



The University of
Nottingham

UNITED KINGDOM • CHINA • MALAYSIA

**LOSSES IN THE REGENERATOR AND THE CRITICAL
SECTIONS OF A TRAVELLING WAVE
THERMOACOUSTIC ENGINE**

DAVID KHOO WEE YANG, BEng. (Hons.)

**Thesis submitted to the University of Nottingham
for the degree of Doctor of Philosophy**

APRIL 2015

Abstract

Thermoacoustic engine (TAE) can be used to convert heat from any source into electrical energy. Despite the theoretical efficiency of the cycle is very close to the Carnot cycle efficiency but due to many practical reasons, the actual efficiency of the engine is still very low. In order to enhance the overall efficiency of the waste-heat driven thermoacoustic engine (WHTAE), it is important to understand and identify the sources of losses in the engine components as well as to suggest design modifications on some critical components in the engine. All the studies reported to date are mainly focusing on the optimisation of the regenerator and the resonator without taking into consideration some of the important issues. One common trait of all the previous optimisation efforts is that the acoustic energy dissipation through the regenerator and the loop (or bends) were not well explained. It should be noted that this study provides a more comprehensive discussion on the acoustic field and the loss mechanisms between the regenerator and the sharp bend (torus-like section) in association with the radiant heat exchanger (RHX) of a WHTAE. In this work, a simplified solution and a numerical investigation are implemented to study the convection and radiation heat transfer between the regenerator and the RHX in two of the SCORE™ engine configurations. Both simplified solution and numerical results reveal that bulge is about three times better in total radiation heat transfer compared to the convolution. Based on the numerical results obtained, the design of the bulge show about five times more in total radiation versus convection to the regenerator top surface. The multi-microphone least square technique is employed in conjunction with impedance tube measurement method to determine the acoustic properties of the tested specimen in order to develop an experimental modelling of a TAE that works in travelling-wave condition by using absorbing materials. Eight materials and combinations are investigated to realise that using an elastic end works best for low frequency attenuation applications. The selection of the attenuation material or combination of materials should be done very carefully and is strongly dependent on the target frequency. No material can work better for all frequencies. Some of the

materials are suitable for high frequency but not suitable for low frequency attenuation applications. The acoustic energy losses through the regenerator and the RHX are determined by utilising the multi-microphone travelling-wave technique. It was found that when more than 30 layers of regenerator, more flow resistance is generated, there is no significant increase in the regeneration effect. Therefore, it is unbeneficial to add more than 30 layers of mesh. Owing to the perfect contact between the working fluid (gas parcels) and the solid material, the dissipation in the regenerator is dominated by viscous losses in both ambient and hot conditions. When imposing a temperature gradient across the regenerator, the system encounters more amplification than attenuation. Straight tube has the least acoustic energy dissipation and the highest loss in acoustic energy is obtained by the convolution RHX configuration. The loss in acoustic energy for the straight tube is mainly due to the viscous losses in the regenerator while the acoustic dissipation for the RHX configuration is mainly caused by the vortices generated at the two 90° sharp bends and the sudden change of cross-sectional area. A thermoacoustic software, DeltaEC is employed to predict the acoustic energy dissipation through the regenerator and the RHX. The numerical model is found to predict the experimental results of the acoustic energy losses accurately. The DeltaEC models can be used to help on the design of future prototypes and for better optimisation of the TAEs.

List of Publications

Journals

1. D. K. W. Yang, Y. A. Abakr, N. M. Ghazali, Experimental investigations on the effects of coiling and bends on the sound energy losses through a resonator tube. *Procedia Engineering*, 2013. **56**: p. 842-848.
2. D. K. W. Yang, Y. A. Abakr, N. M. Ghazali, CFD investigation of the heat transfer between an external heat source and the regenerator of a thermoacoustic engine. *Procedia Engineering*, 2013. **56**: p. 835-841.
3. D. K. W. Yang, Y. A. Abakr, Experimental determination of acoustic losses in an acoustic resonator using impedance tube technique. *Applied Mechanics and Materials*, 2014. **471**: p. 361-366.
4. D. W. Y. Khoo, Y. A. Abakr, N. M. Ghazali, Radiation heat transfer between the externally heated surface and the regenerator of the thermoacoustic engine. *Energy Procedia*, 2015. **61**: p. 2576-2579.
5. D. W. Y. Khoo, Y. A. Abakr, Experimental and numerical investigation of the acoustic absorption coefficient at very low frequency. *Journal of Magnetohydrodynamics*, 2015. **51**(3): p. 249-259.
6. D. W. Y. Khoo, Y. A. Abakr, Effect of different heat exchangers on the waste-heat driven thermoacoustic engine. *Journal of Engineering Science and Technology*, 2016. **11**(1): p. 109-120.

Conferences

1. D. Khoo, Y. A. Abakr, N. M. Ghazali, Numerical investigation on the heat transfer from the cooking stove to the thermoacoustic engine's

- regenerator, in The International Conference, Low-cost, Electricity generating heat engines for rural areas. 2012: Nottingham, UK.
2. D. K. W. Yang, Y. A. Abakr, Experimental determination of acoustic losses in an acoustic resonator using impedance tube technique, in 4th International Conference on Noise, Vibration and Comfort (NVC). 2012: Kuala Lumpur, Malaysia.
 3. D. K. W. Yang, Y. A. Abakr, N. M. Ghazali, Experimental investigations on the effects of coiling and bends on the sound energy losses through a resonator tube, in 5th BSME International Conference on Thermal Engineering. 2012, Bangladesh Society of Mechanical Engineers: Dhaka, Bangladesh.
 4. D. K. W. Yang, Y. A. Abakr, N. M. Ghazali, CFD investigation of the heat transfer between an external heat source and the regenerator of a thermoacoustic engine, in 5th BSME International Conference on Thermal Engineering. 2012, Bangladesh Society of Mechanical Engineers: Dhaka, Bangladesh.
 5. D. W. Y. Khoo, Y. A. Abakr, N. M. Ghazali, Radiation heat transfer between the externally heated surface and the regenerator of the thermoacoustic engine, in The 6th International Conference on Applied Energy (ICAE). 2014, National Taiwan University of Science and Technology: Taipei, Taiwan.
 6. D. W. Y. Khoo, Y. A. Abakr, N. M. Ghazali, The potential of an air-operated thermoacoustic cooler at low pressure, in The 9th Pamir International Conference, Fundamental and Applied MHD. 2014, Institute of Physics of University of Latvia: Riga, Latvia.
 7. D. W. Y. Khoo, Y. A. Abakr, Experimental and numerical investigation of the acoustic absorption coefficient at very low frequency, in The 9th Pamir International Conference, Fundamental and Applied MHD. 2014, Institute of Physics of University of Latvia: Riga, Latvia.

Acknowledgements

First and foremost, I must express my utmost, endless and sincere gratitude to my supervisor, Dr. Yousif Abdalla Abakr, for all his invaluable guidance, patience, enthusiasm and encouragements throughout the entire duration of this study and thesis writing. With his mentorship and direction as well as inspirational advice, my doctoral research has become an enjoyable experience. To me, he is not only my research advisor, he is also a friend, a special person in my life whom I will never forget, akin to a Chinese proverb that says, “one day’s teacher, a whole life’s father”.

I am also grateful to my co-supervisor, Dr. Normah Mohd Ghazali, for her input and guidance during all stages of the research especially her contribution in the process of preparing journal and conference publications.

I would like to thank MOSTI, a ministry of the government of Malaysia, for funding this work, without its support the present study would not have been possible.

I would like to pay my appreciation to my beloved parents and sisters. I would not be where I am today without their love and encouragements.

I would like to take this opportunity to express my deepest appreciation and gratitude to Dr. Yap Eng Hwa, for giving me advices during the 1st and 2nd year of thesis writing as well as his life lessons along the way.

Last but not least, not to be forgotten, my friends for their support and care over the years.

Table of Contents

Abstract.....	i
List of Publications.....	iii
Journals.....	iii
Conferences.....	iii
Acknowledgements.....	v
Table of Contents.....	vi
List of Figures.....	xii
List of Tables.....	xviii
Nomenclature.....	xix
Latin letters.....	xix
Greek letters.....	xx
Subscripts.....	xxi
Superscripts.....	xxii
Abbreviations.....	xxiii
Chapter 1 Introduction of Thermoacoustics and Applications.....	1
1.0 Introduction.....	1
1.1 Background.....	3

1.2	Important Thermoacoustic Parameters	8
1.2.1	Acoustic Wavelength and Frequency	8
1.2.2	Thermal and Viscous Penetration Depths	9
1.2.3	Volume Porosity and Hydraulic Radius.....	10
1.3	Thermoacoustic Heat Engines	11
1.4	Waste-Heat Driven Thermoacoustic Engine	17
1.5	Motivation for the Present Study	19
1.6	Aim and Objectives of this study	21
1.7	Thesis Outline.....	22
Chapter 2 Literature Review.....		25
2.0	Introduction	25
2.1	SCORE™ Project.....	25
2.2	Losses in the Thermoacoustic Engine	28
2.2.1	Energy Dissipation in the Regenerator	29
2.2.2	Energy Losses in the Resonator	31
2.2.3	Energy Dissipation in Tapers and Cones.....	32
2.2.4	Energy Losses in the Radiant Heat Exchanger	33
2.3	Travelling-Wave Thermoacoustic Engine	34
2.4	Numerical Simulation of the Thermoacoustic Engine	36
2.5	Acoustic Measurements	38

2.5.1	One-Microphone and Two-Microphone Methods.....	38
2.5.2	Multi-Microphone Method	40
2.6	Concluding Remarks.....	41
2.7	Research Questions	42
Chapter 3 Methodology.....		44
3.0	Introduction	44
3.1	Simplified Solution and Numerical Study of the Heat Transfer between the Regenerator and the Radiant Heat Exchanger.....	44
3.2	Experimental Modelling of a Travelling-Wave Thermoacoustic Engine 47	
3.3	Losses through the Regenerator and the Radiant Heat Exchanger...47	
3.4	Numerical Modelling of the WHTAE.....	49
3.5	Flow Chart of the Research Activities	50
Chapter 4 Heat Transfer in the Waste-Heat Driven Thermoacoustic Engine ..		51
4.0	Introduction	51
4.1	SCORE™ Thermoacoustic Engine	52
4.2	The Challenge of the Heat Transfer from the Heating Surface to the Hot Heat Exchanger in the SCORE™ Thermoacoustic Engine.....	54
4.2.1	Heat Transfer Processes in an Externally Heated Thermoacoustic Engine 57	
4.2.2	Important Modes of Heat Transfer in the SCORE™ Thermoacoustic Engine	57
4.3	Analysis of Radiation Heat Transfer in the Bulge and Convolution...59	

4.3.1	View Factor calculations for the Convolution and the Regenerator Integrity	59
4.4	Numerical Modelling of Heat Transfer in the SCORE™ Thermoacoustic Engine	65
4.4.1	Modelling of the Regenerator	71
4.5	Results and Discussions	75
4.6	Concluding Remarks	83
Chapter 5 Experimental Modelling of a Travelling-Wave Thermoacoustic Engine		86
5.0	Introduction	86
5.1	Attenuation of Acoustic Waves	87
5.2	Experimental Setup	88
5.3	Different types of Excitation Signals	90
5.4	Multi-Microphone Least Squares Technique	91
5.5	Impedance Tube System	94
5.6	Results and Discussions	95
5.6.1	Absorption and Reflection Coefficients from an Approximate Rigid Surface	95
5.6.2	Performance of Potential Attenuation Alternatives	97
5.7	Concluding Remarks	99
Chapter 6 Losses through the Regenerator and the Radiant Heat Exchanger		100
6.0	Introduction	100

6.1	Losses in the Regenerator	101
6.2	Experimental Setup of the Straight Tube Configuration	102
6.2.1	Regenerator	103
6.2.2	Hot Heat Exchanger	105
6.2.3	Cold Heat Exchanger	105
6.3	Instrumentation and Experimental Procedure for Straight Tube Configuration	106
6.4	Multi-Microphone Travelling-Wave Technique	107
6.5	Acoustic Energy Losses	111
6.6	Womersley Number and the Standing Wave Ratio	111
6.7	Results and Discussions of Losses in the Regenerator	113
6.7.1	Thermal Energy Flow in the Regenerator	113
6.7.2	Acoustic Losses in the Regenerator	117
6.8	Losses through the Radiant Heat Exchanger	124
6.9	Experimental Setup of Radiant Heat Exchanger Configuration	124
6.9.1	Radiant Heat Exchangers	126
6.10	Instrumentation and Experimental Procedure for Radiant Heat Exchanger Configuration	127
6.11	Results and Discussions of Losses through the Radiant Heat Exchanger	127
6.12	Concluding Remarks	132

Chapter 7 Numerical Modelling of the Waste-Heat Driven Thermoacoustic Engine	134
7.0 Introduction	134
7.1 DeltaEC Modelling.....	135
7.2 Model Development	136
7.2.1 Governing Equations	136
7.2.2 Boundary Conditions	137
7.3 Results and Discussions	143
7.3.1 Comparison between the Different Types of Excitation Signals in the Absorption Coefficient Experiment.....	143
7.3.2 Validation against the Experimental Results obtained in the Acoustic Dissipation Experiment	145
7.4 Concluding Remarks.....	152
Chapter 8 Conclusions and Future Work.....	153
8.0 Introduction	153
8.1 Achievements of this Work.....	153
8.2 Limitations.....	156
8.3 Recommendation of Future Work	157
References	159

List of Figures

Figure 1.1: Schematic diagram of (a) Sondhaus tube [10] and (b) Rijke tube [11].	4
Figure 1.2: Schematic diagram of (a) Standing-wave refrigerator by Hofler [18] and (b) Torus section of the thermoacoustic Stirling heat engine by Backhaus and Swift [21]......	6
Figure 1.3: Thermodynamic processes of the standing-wave engine: (a) gas parcel in engine's core, (b) temperature location graph and (c) p - v graph [30].	13
Figure 1.4: Thermodynamic processes of the travelling-wave engine: (a) gas parcel in engine's core, (b) temperature location graph and (c) p - v graph [30].	15
Figure 1.5: SCORE™ engine prototypes: (a) propane-driven thermoacoustic generator (Demo0) and (b) wood-burning thermoacoustic generator (Demo2) [36]......	18
Figure 1.6: Conceptual WHTAE powered by stove.....	19
Figure 1.7: Relationship chart that describes the main research activities in chapter 4 through chapter 7.	24
Figure 2.1: Schematic representation of (a) standing wave ratio technique and (b) the two-microphone method.....	39
Figure 3.1: Two-dimensional representation of (a) convolution and (b) bulge in the view factor analysis.	45
Figure 3.2: Flow chart of the methodology used for the investigation of heat transfer between the regenerator and the RHX.	46
Figure 3.3: Flow chart of the methodology used for the investigation of the passive attenuation and the losses of the engine components.....	49

Figure 4.1: The (a) side view and (b) top view of the SCORE™ engine.....	52
Figure 4.2: Basic concept of a travelling-wave thermoacoustic driver with direct heating at the two sides of the regenerator.	55
Figure 4.3: External heating of the thermoacoustic engine through (a) bulge and (b) convolution.....	56
Figure 4.4: Thermal resistance network between the regenerator and the RHX: (a) bulge and (b) convolution.	58
Figure 4.5: Divisions of one convolution element (convolute) for the view factor calculations (all the dimensions are shown in mm, not to scale).	60
Figure 4.6: Percentage of radiation from each section from the convolution to the regenerator.	60
Figure 4.7: Radiation thermal resistance network for the convolution.	63
Figure 4.8: Radiation heat transfer between the bulge (1) and the regenerator (2).....	64
Figure 4.9: Radiation thermal resistance network between the bulge and the regenerator.....	64
Figure 4.10: Three-dimensional representation of the bulge together with its dimension (in mm).....	65
Figure 4.11: Pressure drop versus velocity along the regenerator.	73
Figure 4.12: Heat flow from different sections of the convolution to the regenerator.....	76
Figure 4.13: Radiation heat transfer from the convolution and from the bulge to the regenerator, with the comparison to the CFD simulation results.	77
Figure 4.14: Convection heat flux and radiation heat flux for different mesh sizes for bulge B at $Z = 0.1$ m on the bulge surface at $t = 15.7$ s when the bulge surface temperature is 1024 K.	78

Figure 4.15: Convection heat flux and radiation heat flux for bulge A, B and C at $Z = 0.1$ m on the bulge surface at $t = 15.7$ s when the bulge surface temperature is 1024 K.....	79
Figure 4.16: Convection heat flux and radiation heat flux for convolution at $Z = 0.1$ m on the convolution surface at $t = 15.7$ s when the convolution surface temperature is 1024 K.	80
Figure 4.17: Cross-section of the convolution model.	80
Figure 4.18: Contour of temperature distribution at XY plane when $Z = 0.1$ m for all the geometries at $t = 7.9$ seconds.....	82
Figure 4.19: Contour of static pressure at XY plane when $Z = 0.1$ m for all the geometries at $t = 15.7$ seconds.....	82
Figure 5.1: Experimental setup of multi-microphone impedance tube system.	89
Figure 5.2: Four different types of materials that are under investigation: (a) Egg tray, (b) Honeycomb, (c) Sponge and (d) Egg tray and sponge combination.	90
Figure 5.3: Impedance tube setup for two-microphone method.	91
Figure 5.4: Reflection coefficient versus frequency when the thick aluminium plate is under examination.....	96
Figure 5.5: Absorption coefficient as a function of frequency when the thick aluminium plate is used as the rigid backing.....	97
Figure 5.6: Absorption coefficient as a function of frequency for all the tested materials when uniform white noise is used as the excitation signal.....	98
Figure 6.1: Layout of the test section for the straight tube configuration in hot condition.....	103
Figure 6.2: Stainless steel wire meshes that are stacked together using sewing.	104

Figure 6.3: Close up (400% magnification) of the regenerator wires.	104
Figure 6.4: Heat exchangers of the system: (a) heating element and (b) cold heat exchanger.	106
Figure 6.5: Normalised time lag for the heat to transfer from hot end to cold end of regenerator.	114
Figure 6.6: Normalised temperature for cold and hot heat exchangers.....	115
Figure 6.7: Real time temperature difference between the cold and the hot heat exchangers in degree Celsius for different number of meshes.	116
Figure 6.8: Downstream normalised energy against frequency for different number of regenerator meshes in ambient condition.....	118
Figure 6.9: Womersley number as a function of frequency for different temperatures at the HHX.	119
Figure 6.10: Womersley number versus temperature for different frequencies.	119
Figure 6.11: Downstream normalised energy against frequency for different number of regenerator meshes when the temperature at the HHX is 373K.	121
Figure 6.12: Downstream normalised energy against frequency for different temperatures at the HHX when 30 layers of regenerator.	121
Figure 6.13: SWR against frequency for different number of regenerator meshes at both upstream (US) and downstream (DS) of the system in ambient condition.	123
Figure 6.14: SWR against frequency for different number of regenerator meshes at both upstream (US) and downstream (DS) of the system when the temperature at the HHX is 373K.....	123
Figure 6.15: Layout of the RHX configuration in (a) ambient condition and (b) hot condition.	125

Figure 6.16: Pattern of the heating element on the two types of RHX: (a) bulge and (b) convolution.....	126
Figure 6.17: Downstream normalised energy against frequency for different temperatures at the RHX when 30 layers of regenerator for bulge.	128
Figure 6.18: Downstream normalised energy against frequency for different temperatures at the RHX when 30 layers of regenerator for convolution.	128
Figure 6.19: Downstream normalised energy as a function of frequency in ambient condition when 30 layers of regenerator for different configurations.	129
Figure 6.20: Downstream normalised energy against frequency when 30 layers of regenerator and the temperature at the HHX is 373K for different configurations.....	130
Figure 6.21: SWR as a function of frequency at both upstream (US) and downstream (DS) of the system in ambient condition when 30 layer of regenerator for different RHXs.....	131
Figure 6.22: SWR against frequency at both upstream (US) and downstream (DS) of the system when 30 layers of regenerator and the temperature at the hot heat exchanger is 373K for different RHXs.....	131
Figure 7.1: Schematic diagram of the impedance tube system produced in DeltaEC.....	138
Figure 7.2: Schematic diagram of the acoustic energy dissipation experiments in hot condition produced in DeltaEC: (a) straight tube configuration and (b) RHX configuration.....	139
Figure 7.3: Reflection coefficient versus frequency when aluminium plate is under examination.	144
Figure 7.4: Absorption coefficient as a function of frequency when aluminium plate is used as the rigid backing.....	144
Figure 7.5: Downstream normalised energy versus frequency in (a) ambient condition and (b) hot condition when the temperature at the HHX is 373K for 30 layers of regenerator in straight tube configuration.....	146

Figure 7.6: SWR versus frequency regenerator meshes at upstream (US) of the system in ambient condition when 30 layers of regenerator for straight tube configuration.147

Figure 7.7: Downstream normalised energy versus frequency in (a) ambient condition and (b) hot condition when the temperature at the RHX is 373K for 30 layers of regenerator in bulge RHX configuration.149

Figure 7.8: Downstream normalised energy versus frequency in (a) ambient condition and (b) hot condition when the temperature at the RHX is 373K for 30 layers of regenerator in convolution RHX configuration.....150

Figure 7.9: SWR versus frequency regenerator meshes at upstream (US) of the system in ambient condition when 30 layers of regenerator for bulge RHX configuration.151

Figure 7.10: SWR versus frequency regenerator meshes at upstream (US) of the system in ambient condition when 30 layers of regenerator for convolution RHX configuration.....151

List of Tables

Table 1.1: The summary of the two types of thermoacoustic engines.....	16
Table 4.1: The calculations of the view factors for all the sections in the convolutions.	61
Table 4.2: Summary of radiation parameters of the convolution sections: (a) view factors, (b) space resistance and (c) surface resistance.	63
Table 4.3: Surface and space resistance between the bulge and the regenerator.	64
Table 4.4: Mesh size, overall RHX surface area and total RHX volume excluding the porous media (regenerator) for all the four geometries.	67
Table 4.5: Fluent settings for all the four geometries.....	69
Table 4.6: SCORE™ experimental data [7].	72
Table 7.1: Summary of the dimensions and other details of the impedance tube system.....	138
Table 7.2: Summary of the dimensions and other details of the RHX configuration.	142
Table 7.3: Summary of the number of GUESSES and TARGETS in both phases of the numerical model.	143

Nomenclature

Latin letters

a	Speed of sound	[m/s]
A	Cross-sectional area	[m ²]
c	Speed of sound	[m/s]
c_p	Isobaric heat capacity	[J/(kg.K)]
c_v	Isochoric heat capacity	[J/(kg.K)]
C	Inertial resistance factor	
	Wave component	
d	Diameter	[m]
dx	Distance between microphone and sample	[m]
D	Depth	[m]
	Viscous resistance factor	
E	Emissive power	[W/m ²]
	Energy	[W]
f	Frequency	[Hz]
	Rott function	
F	View factor	
g	Green function	[kg/(m ⁴ .s)]
H	Transfer function	
J	Radiosity	[W/m ²]
k	Thermal conductivity	[W/(m.K)]
	Wave number	[m ⁻¹]
k'	Real component of ϵ	[m ⁻¹]
k''	Imaginary component of ϵ	[m ⁻¹]
L	Length	[m]
m	Number of wire per unit length	[wires/m]
	Mass	[kg]
N_{mesh}	Number of mesh	
p	Pressure	[Pa]
Pr	Prandtl number	
\dot{q}	Rate of heat transfer per unit surface area	[W/m ²]

\dot{Q}	Rate of heat transfer	[W]
Q	Heat	[J]
r_h	Hydraulic radius	[m]
R	Gas constant	[J/(kg.K)]
	Ratio of curve radius over distance between two cylindrical surfaces	
	Thermal resistance	[K/W]
	Reflection coefficient	
s	Cross-sectional area	[m ²]
S	Momentum source term	[kg/s ²]
t	Time	[s]
T	Temperature	[K or °C]
U	Volume velocity	[m ³ s ⁻¹]
V	Volume	[m ³]
v	Velocity	[m/s]
\dot{W}	Acoustic energy flow	[W]
W_o	Womersley number	
z	Distance between microphone and sample	[m]

Greek letters

α	Absorptivity	
	Absorption coefficient	
	Permeability	
σ	Boltzman's constant	
φ	Volumetric porosity	
δ	Penetration depth	[m]
ε	Emissivity	
	Complex wave number	[m ⁻¹]
κ	Thermal diffusivity	[m ² /s]
λ	Acoustic Wavelength	[m]
γ	Ratio of specific heat	
ρ	Density	[kg/m ³]
	Reflectivity	
τ	Transmissivity	
μ	Dynamic viscosity	[kg/m.s]
ν	Kinematic viscosity	[m ² /s]

ω Angular frequency [rad/s]

Subscripts

b	Blackbody
bulge	Bulge radiant heat exchanger
convolution	Convolution radiant heat exchanger
cond	Conduction
conv	Convection
dot	Overdot (Time derivative)
D	Downstream
gas	Gas
i	Incident
k	Thermal
l	Low limit
lag	Lagging
m	Mean
max	Maximum
min	Minimum
N	Normalisation
opt	Optimisation
rad	Radiation
reg	Regenerator
s	Surface
solid	Solid
u	Upper limit
U	Upstream
v	Viscous
wetted	Gas-solid contact area
wire	Wire of mesh screen
+	Incident
-	Reflected
1	First-order

Superscripts

H	Hermitian matrix of K
+	Moor-Penrose generalized inverse of K
*	Complex conjugate

Abbreviations

AC	Alternating Current
AHX	Ambient Heat Exchanger
CHX	Cold Heat Exchanger
CFD	Computational Fluid Dynamics
COP	Coefficient Of Performance
COPC	Carnot Coefficient Of Performance
DAQ	Data AcQuisition system
DeltaEC	Design Environment for Low Amplitude thermoacoustic Energy Conversion
DS	DownStream
FFT	Fast Fourier Transform
HHX	Hot Heat Exchanger
LANL	Los Alamos National Laboratories
NI	National Instruments
OPTR	Orifice Pulse Tube Refrigerator
PIV	Particle Image Velocity
RAN	Reynolds Averaged Navier-stokes
RHX	Radiant Heat Exchanger
RPN	Reverse Polish Notation
SCORE™	Stove for COoking, Refrigeration and Electricity
SIMPLE	Semi Implicit Method for Pressure Linked Equations
SWR	Standing Wave Ratio
S2S	Surface-to-Surface
TAE	ThermoAcoustic Engine
TAR	ThermoAcoustic Refrigerator
TASHE	ThermoAcoustic Stirling Heat Engine
UDF	User Defined Function
US	UpStream
WHTAE	Waste Heat Driven Thermoacoustic Engine

Chapter 1

Introduction of Thermoacoustics and Applications

1.0 Introduction

Thermoacoustic effect is the thermodynamic interaction of a sound wave with solid material that has a temperature gradient along the direction of the sound wave propagation. Lord Rayleigh [1], a well-known physicist, was the first to explain qualitatively the thermoacoustic effect. A thermoacoustic engine (TAE) converts heat energy to acoustic energy via its core, comprising a porous material (regenerator) that is sandwiched between two heat exchangers (hot and ambient). The two heat exchangers impose a temperature gradient along the porous material, which is required to sustain and amplify the acoustic wave that is generated. Thermoacoustic devices have two major advantages over traditional energy conversion systems: their inherent mechanical simplicity, and the use of environmentally friendly working gases. Thermoacoustic engines (TAEs) are capable to produce acoustic energy from any source of heat energy. One of the potential applications for TAEs is to make use of low-quality heat sources such as industrial waste heat, solar energy or fossil fuels for energy recovery. Thus, the primary energy source to drive a TAE could be conventional or unconventional. In a typical TAE, heat is injected directly to the

system by using a hot heat exchanger (HHX). If the heat source for the TAE is waste heat, the entire system has no harmful effects on the environment thus can be termed as a sustainable TAE system. Several researchers had designed thermoacoustic devices that capture waste heat to perform useful work. Symko et al. [2] designed thermoacoustic prime mover that operates using heat from a microcircuit to remove heat by using the produced acoustic radiation. The proposed TAE achieved an onset temperature difference of 25 °C. Another interesting development was addressed by Hatazawa et al. [3] whom used heat energy from the exhaust gas of a 4-stroke automobile gasoline engine to drive a standing-wave heat engine. Thermal input to the TAE was reported to be in excess of 300 W at over 300 °C, achieved with an engine speed of 2600 rpm and a throttle opening of 35 %. Adeff and Hofler [4] constructed and tested a prototype thermoacoustic refrigeration system that utilises solar energy. A cooling power of 2.5 W and the corresponding cold temperature of 5 °C was accomplished. Babaei et al. [5] proposed a waste-heat driven refrigeration system that operates using waste heat from a gas turbine engine. An overall theoretical efficiency of 36 % with a refrigeration coefficient of performance (COP) of 2.35 was achieved in their work. Zoontjens et al. [6] theoretically studied the feasibility of using thermoacoustic cooling technology for automotive air conditioning that utilises on the waste heat from an automobile engine. The proposed device was capable of producing a cooling power that is equivalent to 10% of the waste heat input. The waste-heat driven thermoacoustic engine (WHTAE) investigated in this study was first designed and studied by the SCORE™ (Stove for COoking, Refrigeration and Electricity) project as illustrated in Figures 1.5 and 1.6 [7]. An achievement of 36 W of electricity was obtained by utilising the waste heat energy from cooking stove [8]. Current research interests include both the in-depth understanding of the fundamental thermoacoustic processes in the SCORE™ engine and the

optimisation of the overall efficiency in order to improve the performance of the engine.

1.1 Background

The thermoacoustic phenomenon was first noticed in the mid of the 19th century when glass blowers noticed that the temperature difference between the hot glass bulb and the cooler tube caused the tube to generate audible tones [9]. Sondhauss [10], a German physicist, experimented with a closed-open tube, heating it by applying a flame to the bulb at the closed end to produce sound. This noise emitter became the earliest TAE known as a Sondhauss tube. The schematic diagram of the Sondhauss tube is illustrated in Figure 1.1 (a). Sondhauss explored the relation between the geometry of the resonating tube and the frequency of the sound produced. He noticed that the oscillation frequency was linked to the length of the tube and the volume of the closed end bulb. The sound produced was found to be more intense when a hotter flame was applied. However, Sondhauss did not give an explanation of the observations.

Rijke [11] managed to find that a glass tube with both ends open could also produce audible tones as displayed in Figure 1.1 (b). He found that the sound could only be produced when the tube was in a vertical orientation and the heating element was in the lower half of the tube, indicating that the convective flow created by heating air in the tube was necessary to its sound production. Rijke then concluded that the sound created was the loudest when the heated wire mesh was placed approximately one-quarter length from the bottom of the tube.

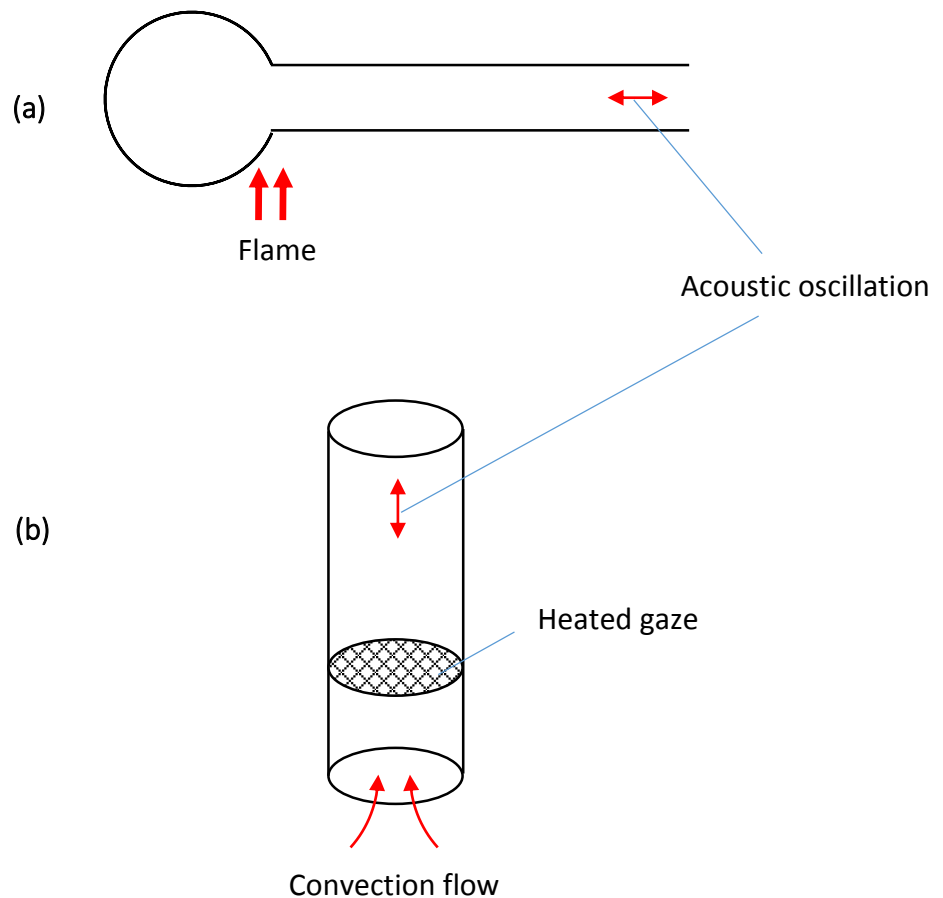


Figure 1.1: Schematic diagram of (a) Sondhauss tube [10] and (b) Rijke tube [11].

Rayleigh [1], a British physicist, understood that the sound was generated by the oscillatory thermal expansion and compression of the air in the tube. Rayleigh then formulated a criterion to explain how acoustic waves could be excited and sustained by heat addition:

“If heat be communicated to, and abstracted from, a mass of air vibrating (for example) in a cylinder bounded by a piston, the effect produced will depend upon the phase of the vibration at which the transfer of heat takes place. If heat be given to the air at the moment of greatest condensation, or be taken from it at the moment of greatest rarefaction the vibration is encouraged. On the other hand, if heat be given at the moment of greatest rarefaction, or

abstracted at the moment of greatest condensation, the vibration is discouraged [1].”

Although Rayleigh gave the correct qualitative description of the oscillating thermodynamics that is the core of standing wave engines, an accurate theory was not developed until Nikolaus Rott derived mathematical equations describing acoustic oscillations in a gas in a channel with an axial temperature gradient and lateral channel dimensions of the order of gas thermal penetration depth. These equations were then verified experimentally by Yazaki et al. in the context of Taconis oscillations, which can occur when a gas-filled tube is cooled from ambient temperature to a cryogenics temperature [12]. Rott’s work forms the theoretical basis of most of modern standing wave thermoacoustic [13-17].

Hofler [18] invented a standing-wave thermoacoustic refrigerator (TAR) as illustrated in Figure 1.2 (a), and demonstrated that Rott’s approach to acoustic in small channels was quantitatively accurate. In this type of refrigerator, the coupled oscillations of gas motion, temperature, and heat transfer in the sound wave are phased in time so that heat is absorbed from load at a low temperature and waste heat is rejected to a sink at a higher temperature. Meanwhile, pulse-tube refrigeration was becoming the most active investigation area of cryogenic refrigeration. Gifford [19] displayed a heat-pumping process along the inner surface of a closed tube, where pressure oscillations at low frequency were sustained. Mikulin [20] published a paper describing their experimental findings stating that the oscillating flow generated in a gas-filled resonance tube can produce not only heating but also cooling of the tube wall. They developed an analytical expression for heat flux in resonant tubes and tested its validity with laminar flow experiment. The oscillations were driven by a piston at one end of the tube and the other end is

closed by a shiftable end and the walls of the resonance tube were kept at uniform temperature. They found both experimentally and theoretically that the wave motion is attended by time-averaged net heat flows. The longitudinal heat flux is transported from the velocity antinode to the adjacent pressure antinodes; and the transverse heat flux is rejected to the environment in a region near the pressure antinode or is absorbed from the environment in a region near the velocity antinode, if the Prandtl number of the ideal gas medium is smaller than unity.

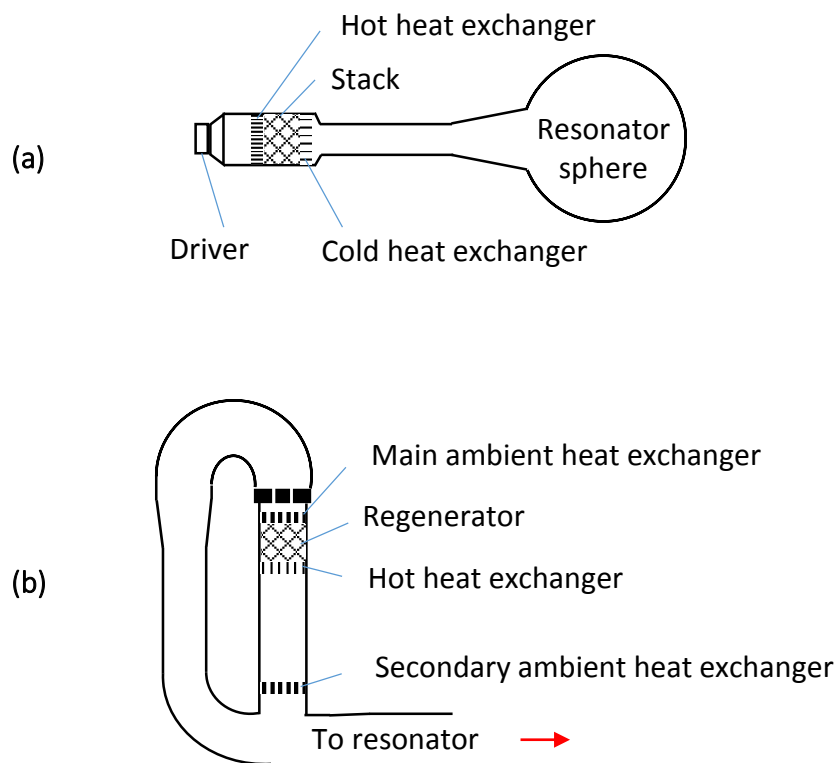


Figure 1.2: Schematic diagram of (a) Standing-wave refrigerator by Hofler [18] and (b) Torus section of the thermoacoustic Stirling heat engine by Backhaus and Swift [21].

Around the mid of 20th century, Bell Telephone Laboratories in the United States received a few patents for electrical generators which converted the acoustic power from Sondhauss tube into useful levels of electrical power. These devices would convert heat (from an open flame) into a pressure wave

(acoustic power) with a TAE (Sondhauss tube), and then the acoustic power was converted into electricity by cycling an acoustical-to-electric transducer. The concept for these devices was attractive because the conversion of heat into acoustic power requires no moving parts, hence they were relatively inexpensive to build, reliable and would require a low amount of maintenance. However, they were not considered applicable because the conversion of heat into acoustic power was not efficient and the pressure oscillations were relatively weak. It seems that to this point in time, no standing wave heat engine has achieved thermal efficiency in excess of 20 %. Feldman et al. [22] explained that the performance of Sondhauss tube could be improved by inclusion of a stack of small tubes. Using stack of small tubes has the effect of increasing the effective contact area between the gas and the solid over the cross section of the small tube, so that the whole gas contributes to the thermoacoustic heat transport process. According to Swift, theoretical modeling of the complex thermoacoustic environment in detail did not begin until the late 1960s.

Swift describes Rott and colleagues as the developers of useful theoretical formulation for thermoacoustic devices, citing their progressive development in articles from 1969 until 1983. Rott's equations have formed a solid basis for the design of low-amplitude thermoacoustic heat engines and pumps, and his work is considered to be the foundation from which modern thermoacoustic has developed. Investigation of thermoacoustic refrigerators (TARs) and thermoacoustic engines (TAEs) began at Los Alamos National Laboratories (LANL) in the early 1980s. Wheatley, Swift and Hofler among others are largely responsible for the new wave of advancements in practical thermoacoustic engines and refrigerators [23-26]. The first TAR was built at LANL, used a loudspeaker at one end of a closed tube, and a stack made of fibre glass plates positioned at the opposite end [18]. The stack of plates was used to improve

the thermoacoustic effect. Since then, many thermoacoustic devices have been constructed.

Tijani et al. [27] designed and built a standing wave TAR much like Hofler's but he devoted more attention to the effects of varying certain parameters, such as working gas properties and stack size. Garret et al. [28] developed a TAR for cooling samples collected on space missions. Swift [29] designed a large TAE to drive an orifice pulse tube refrigerator, another kind of thermoacoustic device, which liquefied natural gas. Ballister and Mckelvey [30] created a thermoacoustic device for cooling shipboard electronics. Backhaus and Swift experimented with a travelling wave TAE that provided almost reversible heat transfer in the regenerator [21]. Figure 1.2 (b) shows the schematic diagram of the thermoacoustic heat engine by Backhaus and Swift. Ceperley's orifice pulse tube refrigerator is an example of a travelling wave TAE [31]. Either a predominantly standing wave or a predominantly travelling wave can be used, although geometries for the two types of waves are substantially different.

1.2 Important Thermoacoustic Parameters

1.2.1 Acoustic Wavelength and Frequency

The acoustic wavelength and frequency are the main parameters determining the total length of a thermoacoustic device. The acoustic wavelength is the distance at which an acoustic wave repeats itself which can be expressed by Equation (1.1):

$$\lambda = \frac{a}{f} \tag{1.1}$$

Where a is the speed of sound and f is the oscillation frequency. In essence, standing-wave thermoacoustic devices have a total length that is equivalent to half or quarter of the acoustic wavelength whereas travelling-wave thermoacoustic devices are designed to operate in one acoustic wavelength. The speed of sound for ideal gases can be defined by Equation (1.2):

$$a = \sqrt{\gamma RT} \quad (1.2)$$

$$\gamma = \frac{c_p}{c_v} \quad (1.3)$$

Where γ , c_p , c_v , R , T are the ratio of specific heat, isobaric heat capacity, isochoric heat capacity, gas constant and temperature respectively.

1.2.2 Thermal and Viscous Penetration Depths

The thermal penetration depth can be expressed in Equation (1.4). It is an important characteristic length in understanding the thermodynamic processes in the thermoacoustic devices. The thermal penetration depth is the lateral distance that describes how far heat can diffuse through the gas during a time interval of the order of the period of the oscillation divided by π .

$$\delta_k = \sqrt{\frac{2k}{\omega \rho c_p}} \quad (1.4)$$

Where k , ω , ρ are the thermal conductivity, the angular frequency and the density of air respectively. Another important length scale of great importance in thermoacoustics, is the viscous penetration depth which is expressed in Equation (1.5). The viscous penetration depth is the distance perpendicular to the direction of motion of the gas that is related to the lateral diffusion of momentum in a period of oscillation divided by π .

$$\delta_v = \sqrt{\frac{2\mu}{\omega\rho}} \quad (1.5)$$

Where μ represents the dynamic viscosity. It is within this layer that viscous shear forces occur which lead to the acoustic energy dissipation. When the gas is at distances to the nearest solid much greater than these penetration depths, the gas will not experience both thermal and viscous effects. The square of the ratio of these two penetration depths is called the Prandtl number which is defined by Equation (1.6):

$$Pr = \left(\frac{\delta_v}{\delta_k}\right)^2 = \frac{\mu c_p}{k} \quad (1.6)$$

The thermoacoustic devices usually suffer from substantial viscous losses because the Prandtl number is close to unity for typical gases. Therefore, working gasses that have lower Prandtl number such as helium or mixture of gases can be beneficial to balance between viscous losses and thermal efficiency.

1.2.3 Volume Porosity and Hydraulic Radius

With regard to the design of the stack or regenerator, there are another two important parameters that require special attention. The first parameter is the volumetric porosity which is defined as the ratio of the volume of gas in the stack or regenerator to the total volume of the stack or regenerator.

$$\phi = \frac{V_{gas}}{V_{gas} + V_{solid}} \quad (1.7)$$

Where V_{gas} is the volume of gas and V_{solid} is the volume taken up by the solid material in Equation (1.7). The second important parameter is the hydraulic

radius which is defined as the ratio of the gas volume to the gas-solid contact area.

$$r_h = \frac{V_{gas}}{A_{wetted}} \quad (1.8)$$

Where A_{wetted} is the interface area between the gas and the solid material in the regenerator in Equation (1.8). These two parameters for designing a stack-screen regenerator can also be written as shown in Equations (1.9) and (1.10) [32].

$$\phi \approx 1 - \frac{\pi m d_{wire}}{4} \quad (1.9)$$

$$r_h \approx d_{wire} \frac{\phi}{4(1-\phi)} \quad (1.10)$$

Where m is the number of wires per unit length and d_{wire} is the wire diameter.

1.3 Thermoacoustic Heat Engines

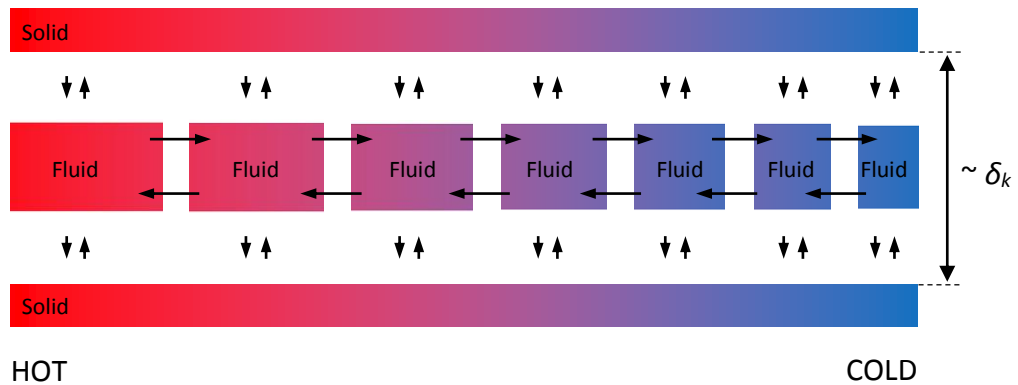
The function of a thermoacoustic heat engine is to produce useful work from the heat supplied to the engine. The fundamental components of a typical thermoacoustic heat engine include a resonator tube, a regenerator or a stack, and heat exchangers. There are mainly two different types of TAEs: standing-wave engine and travelling-wave engine. Advantages of thermoacoustic devices include environmental friendliness, potentially high reliability due to simple structure, no moving parts and reasonable efficiency. In order to understand more in depth of the thermoacoustic processes, the diagrams produced by Los Alamos National Laboratory (LANL) are used in this work to describe the difference between standing-wave and travelling-wave engines [32]. The diagrams present a comprehensive illustration of the thermoacoustic

processes occur in the two types of the thermoacoustic devices as displayed in Figures 1.3 and 1.4.

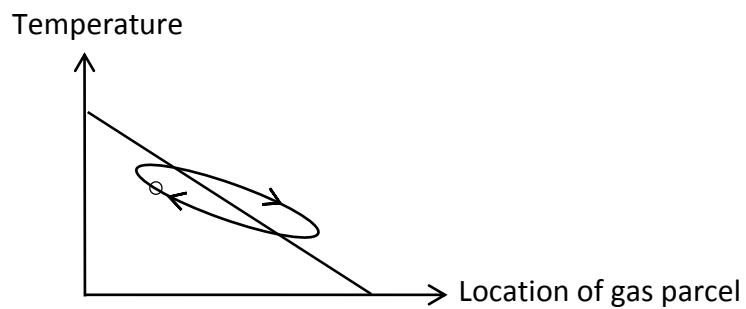
The movement of a gas parcel in the stack of a standing-wave engine is magnified as presented in Figure 1.3 (a). When the gas parcel displaces to the left hot end (thermal expansion and the pressure is high), it is cooler than the surrounding plates, so it absorbs heat from the plates; when the gas parcel displaces to the right cold end (thermal contraction and the pressure is low), it is warmer than the surrounding plates, so it rejects heat to the plates. According to Figure 1.3 (b), the diagonal line indicates the temperature of the plates as a function of position, and the moving dot traces the temperature of the gas parcel as a function of both time and position. The time phasing between pressure and motion (compression and expansion) is crucially important. It can be illustrated by the graph of pressure, p against volume of gas parcel, v as a function of time. Based on Figure 1.3 (c), if the thermal expansion and contraction are absent (no heat transfer), the graph would appear simply as an oscillation along a diagonal line (a diagonal line only). The thermal expansion and contraction have expanded the line into a narrow ellipse. The area of the enclosed ellipse is the cycle integral of pressure with respect to the volume which is also the net work done per cycle by the gas parcel on its surroundings. The sum of such works by all the gas parcels in the stack is the work produced by the engine. This work is produced at acoustic frequency of standing wave so it is an acoustic power.

The thermal contact between the gas parcel and plates must be neither too strong nor too weak. If it is too weak, no heat transfer between gas parcel and plates, so no thermal contraction and expansion thus no work occur. If it is too strong, the gas parcel temperature would trace an oscillating line exactly on top of the solid local temperature in the temperature-location graph, which

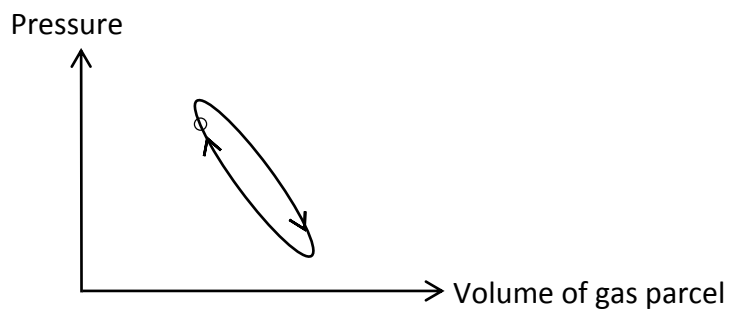
would shift the time phasing of thermal contraction and expansion by almost 90° (thermal contraction when the pressure is high and expansion when the pressure is low). With such phasing, the p - v graph would become a reciprocating line and again no work occurs.



(a)



(b)



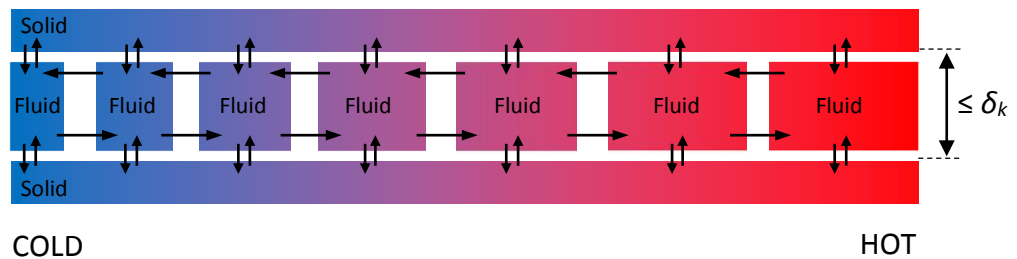
(c)

Figure 1.3: Thermodynamic processes of the standing-wave engine: (a) gas parcel in engine's core, (b) temperature location graph and (c) p - v graph [30].

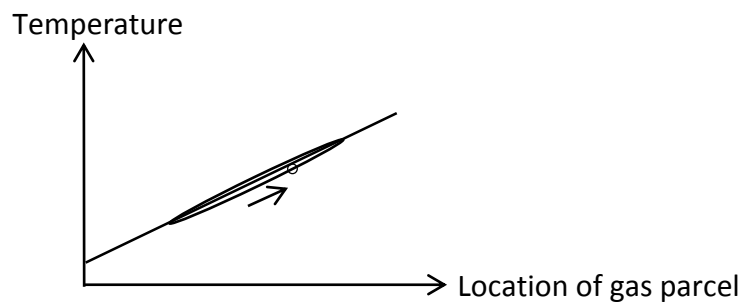
A successful standing wave engine requires imperfect thermal contact between the gas parcel and the stack. Therefore the stacks are made to have gaps similar

in magnitude to the thermal penetration depth of the gas. If the heat exchanger maintains a large temperature gradient along the plate, the gas parcel in stack produces work, simply because the gas parcel in stack experiences thermal expansion when the pressure is high and contraction when the pressure is low (in phase). Thus the gas parcel in the stack pumps acoustic power into the standing wave. The standing wave therefore provides oscillating pressure and oscillating motion that causes the gas parcel to experience oscillating temperature responsible for thermal expansion and contraction. The velocity of gas parcel along the stack temperature gradient is 90° out of phase with oscillating pressure, so imperfect thermal contact is required to enable thermal expansion and contraction steps to be in phase with the oscillating pressure. These complex coupled oscillations appear spontaneously whenever the temperature gradient is high enough.

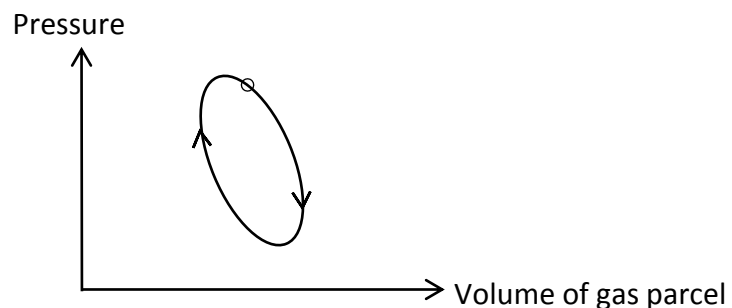
On the other hand, the travelling-wave Thermoacoustic Stirling Heat Engine (TASHE) has a HHX at the right end and a cold heat exchanger (CHX) at the other end of a regenerator instead of a stack as shown in Figure 1.4 (a). When the gas parcel travels to the left, the heat is transferred from the gas parcel to the plates (rejecting heat to the solid and compress slowly), until the gas parcel starts to move to the right, the heat transfer direction changes slowly and the gas parcel moves to the other end (from the plate to the gas parcel). The right end (hot end) has a high pressure and vice versa for the left end (cold end). Hence the gas parcel in the regenerator experiences thermal expansion (starting to) when the pressure is high and thermal contraction (compression process) when the pressure is low.



(a)



(b)



(c)

Figure 1.4: Thermodynamic processes of the travelling-wave engine: (a) gas parcel in engine's core, (b) temperature location graph and (c) p - v graph [30].

In contrast with standing wave TASHE, the velocity of the gas along the regenerator temperature gradient is substantially in phase with the oscillating pressure. Therefore, almost perfect thermal contact between the gas parcel and adjacent plate must be achieved in order to cause the thermal expansion and contraction steps to be in phase with the oscillating temperature. This level of thermal contact can be accomplished by building the gaps between the regenerator to be of a hydraulic radius much less than the thermal penetration depth of the gas. The temperature-location graph shows the gas parcel

temperature as a function of time always lies at top of the local solid temperature (every point within the regenerator, the gas parcel and the adjacent plates are at the same temperature at any axial location) as illustrated in Figure 1.4 (b). Heat is transported from high to low temperature, thus producing an amount of work. Figure 1.4 (c) demonstrates the p-v graph of the travelling-wave engine. The characteristics of the two types of TAEs can be summarised as displayed in table 1.1.

Table 1.1: The summary of the two types of thermoacoustic engines.

Engine Type	Standing Wave	Traveling Wave
Porous medium	Stack	Regenerator
Phase	Pressure and displacement in phase. Velocity is (almost) 90° out of phase with pressure.	Pressure and velocity in phase (to allow transmission of acoustic energy in the direction of the acoustic travelling wave). Acoustic gas displacement & temperature lags the acoustic pressure by 90°.
Function	Absorbs heat at a high temperature and exhausts heat at a lower temperature while producing work as an output.	
Gas parcel movement	Thermal expansion of the parcel occurs when the surrounding pressure is high and thermally contract when it displaces to the cold side where the surrounding pressure is low.	
Pore size, r_h	$= \delta_k$ (Thermal penetration depth) Imperfect thermal contact/heat exchange between the fluid and the solid. As a result, a phase shift or time delay introduced between the pressure and the temperature of the gas parcels that are at a distance (lateral dimension) of about a penetration depth from stack plate. Parcels that are father away have no thermal contact ($\geq \delta_k$) with the plate and are simply	$\leq \delta_k$ Almost perfect thermal contact between the fluid and the solid. As a result, every point within the regenerator, the gas parcels and the regenerator solid plates are at same temperature at any axial location.

	compressed and expanded adiabatically.	
Thermodynamics cycle	2 reversible adiabatic compression and expansion steps & 2 irreversible isobaric heat transfer steps. (Brayton cycle)	2 reversible isothermal compression and expansion steps & 2 reversible polytropic isochoric displacement heat transfer steps. (Stirling cycle)
Advantages (A) and disadvantages (D)	A - Low viscous dissipation because wider pores.	A - No irreversible processes A - Ideal efficiency = Carnot efficiency
	D - Irreversible heat transfer and friction which has negative effect on the efficiency.	D - Significant viscous dissipation due to narrow pores. (lower the efficiency)

1.4 Waste-Heat Driven Thermoacoustic Engine

The waste-heat driven thermoacoustic engine (WHTAE) investigated in this study was first designed by an international collaboration research consortium which aims to develop a wood-powered generator capable of both cooking and cooling food to be used in rural area, the project is named SCORE™ (Stove for Cooking, Refrigeration and Electricity). SCORE™ team has successfully demonstrated the potential development of low cost TAEs for rural communities in the past few years [7, 33-35]. The recent focus of SCORE™ project is to make use of wood instead of propane gas as a heat source to generate electricity. In a recent SCORE™ engine design, the bulge is substituted by a convolution which is believed to have a better heat transfer to the regenerator of the engine [8, 36]. Figure 1.5 shows the two actual prototypes of the SCORE™ engine: propane-driven thermoacoustic generator (Demo0) and wood-burning thermoacoustic generator (Demo2) [36].

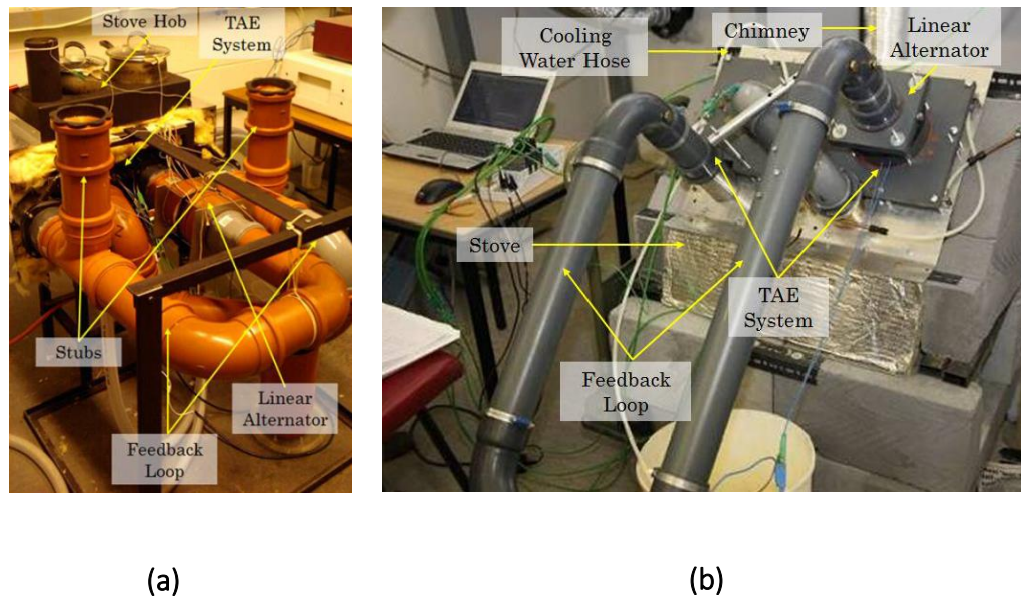


Figure 1.5: SCORE™ engine prototypes: (a) propane-driven thermoacoustic generator (Demo0) and (b) wood-burning thermoacoustic generator (Demo2) [36].

The waste heat from an integrated stove is harvested and transported into the WHTAE with the aid of a radiant heat exchanger (RHX). A schematic diagram of the conceptual WHTAE is illustrated in Figure 1.6. The bulge or convolution acts as a RHX that transfers heat from the external heat source into the engine. The thermally induced acoustic energy is converted into electrical energy by using a linear alternator which is installed near the CHX. In order to enhance the efficiency of the engine, which is crucial for maximising the overall engine performance, it is important to supply most of the heat to the engine directly at the regenerator top surface.

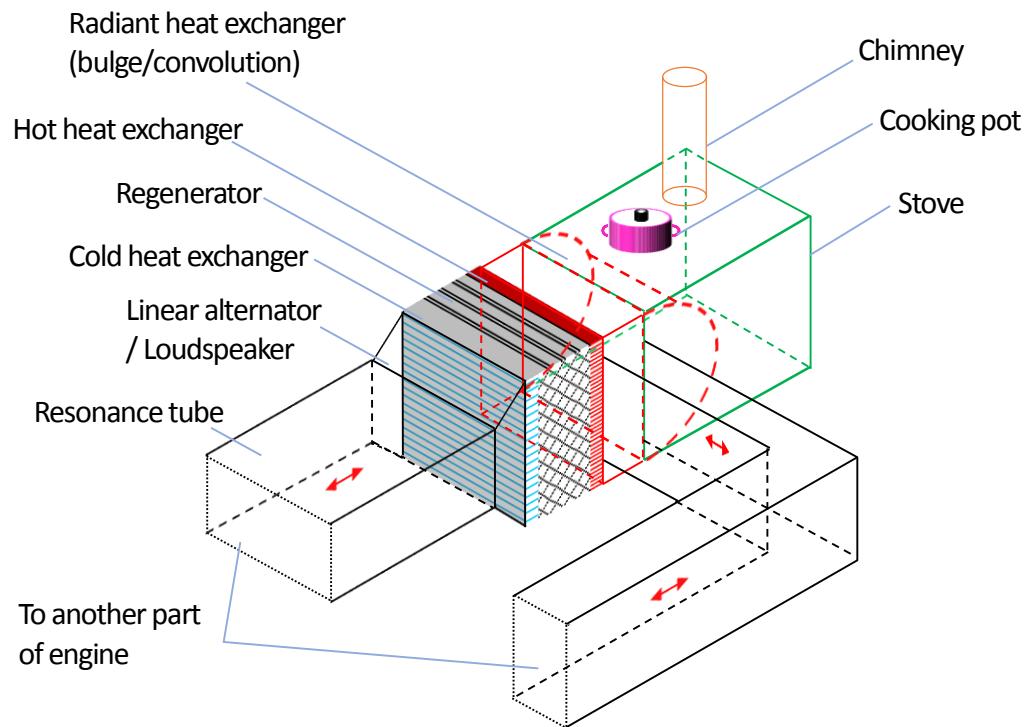


Figure 1.6: Conceptual WHTAE powered by stove.

1.5 Motivation for the Present Study

It is intuitive that the energy dissipation in the engine is mainly contributed by the thermosviscous losses in the regenerator. Although the amount of useful work could be increased by using more regenerator layers but attenuation would also be introduced at the same time. Regenerators for thermoacoustic applications have been studied for many years but most of the reported literatures seek to optimise the regenerator and there is inadequate knowledge related to the loss mechanism and the acoustic field in the regenerator. While there has been some research carried out to study the energy dissipation in the regenerator but it seems that most of these efforts are concentrating on the cryogenic systems where regenerators are used in Stirling Cryocoolers [37, 38] because of the higher potential applications in the

refrigeration systems. One of the obstacles that prohibit researchers to implement the investigation on the losses through the regenerator in the engine is the temperature limitation of the sensors used. When measuring the losses in the hot condition, the sensors would need to be placed close to the hot heat exchanger [39, 40]. Moreover, based on the author's knowledge, there were no studies conducted on using perspex resonator to study the energy dissipation in the regenerator which makes this work to be unique and novel. Hence, special attention should be given to the core of engine which is the regenerator where the energy conversion takes place.

The WHTAE used by the SCORE™ project is externally heated via a RHX which makes it very special from other existing thermoacoustic devices. It has been determined that for best performance of the engine, most of the heat should be supplied at the top layer of the regenerator. Therefore the RHX component plays an important role in determining the overall efficiency of the engine. However, this influencing factor remains as one of the priority areas of concern that has yet to be explored. To date, there is only one study related to the investigation of the RHX in the SCORE™ engine [8]. The importance of the investigation on the heat transfer between the regenerator and the RHX was also been addressed [36]. Owing to the resonator design of the complete SCORE™ engine where acoustic loops are constructed by bends which contribute to unexpected losses in the engine, the implementation of losses and heat transfer experiments on the actual engine would not be feasible. Another problem associated with the implementation of energy dissipation and heat transfer experiments on the SCORE™ engine would be the dual engine configuration. The performance of each TAE is not exactly identical and this can cause the measurements taken to be inaccurate. Besides that, changing the RHX components and install them on the similar engine can be a difficult mission as it requires a lot of fabrications and modifications of the

entire engine design. As a result, the research on the energy dissipation through the regenerator and the heat transfer process between the RHX and the regenerator of the SCORE™ TAE has become a growing concern and a hot topic that needs to be explored. The findings of this work can then be used to optimise the design of the future SCORE engine.

1.6 Aim and Objectives of this study

The aim of this work is to improve the WHTAE by means of understanding and identifying the sources of losses in the engine components as well as suggesting design modifications on some critical components in order to enhance the overall performance of the engine. This study consists of mainly five objectives:

- 1) To analyse the heat transfer process in the regenerator and the RHX.
- 2) To develop an experimental model of a travelling wave TAE with an optimised attenuation of the wave at the end of an open loop so that a travelling-wave engine is resembled.
- 3) To evaluate the acoustic field in the WHTAE.
- 4) To assess the acoustic energy loss through the regenerator and the RHX.
- 5) To create a numerical model of the WHTAE to be used for detailed parametric analysis and optimisation studies.

1.7 Thesis Outline

This thesis is organised in 8 chapters. In the current chapter, after an overview of thermoacoustic history, important characteristic length, a description to the ideas, working principle of both TAEs and WHTAE, the aim and objectives of the current study are proposed and scope of work is presented.

Chapter 2 reviews and discusses some of the relevant previous research work. Firstly, reviewed literatures about the SCORE™ project are presented including the most recent effort made on the investigated WHTAE in this study [41]. The previous work related to the energy dissipation in the engine's components including the regenerator, resonator, RHX, tapers and cones are also reported. In order to have a better understanding of the TAE that is working in a travelling condition, literatures regarding engines that operates in travelling-wave phasing are also included in this chapter. The previous work about the numerical modelling of travelling-wave TAEs using DeltaEC (Design Environment for Low-amplitude ThermoAcoustic Energy Conversion) [42] are also covered in this chapter. The studies related to different microphone techniques used to determine acoustic properties are also presented.

Chapter 3 summarises the research methodology used in this study. A flow chart of the overall methodology is presented to describe the flow of the research activities of this work.

Chapter 4 is devoted to the simplified solution and the numerical investigation of the two modes of heat transfer: convection and radiation. The investigation of the heat transfer between the regenerator and the RHX (bulge or convolution) are conducted in two consecutive stages. In the first stage, a simplified solution of the radiative heat flux distribution generated in the

engine is under examination. Second stage of the heat transfer investigation would be to simulate numerically the coupled heat transfer effect and the temperature gradient from the RHX to the regenerator top surface. The comparison of results between the simplified solution and the numerical simulation are also included in this chapter.

The experimental modelling of a TAE that works in travelling-wave condition by using absorbing materials is introduced in chapter 5. The acoustic properties of different absorbing materials are determined by using the least squares technique with the aid of multi-microphone impedance tube system [43-45] as presented in this chapter. The comparison of the experimental results against the results produced by the numerical simulation using DeltaEC [46, 47] are discussed in chapter 7.

Chapter 6 details the energy fluxes in both the regenerator and the resonator in association with radiant heat exchangers (RHXs) of different forms. The energy transportation in the straight tube configuration and the complete experimental setup (bulge and convolution configuration) are discussed in this chapter. The acoustic energy dissipation through the regenerator and the bends in integration with RHXs are determined by using the multi-microphone method based on travelling-wave technique. The experimental results are compared with the numerical results obtained using DeltaEC in chapter 7.

Chapter 7 presents a numerical analysis using DeltaEC. The predictions of the reflection and absorption coefficients as well as the energy losses produced by DeltaEC are validated against the experimental results in chapters 5 and 6. Chapters 4 through 7 contain the main research activities of this thesis and are summarized in the relationship chart shown in Figure 1.7. Lastly, chapter 8 draws conclusions based on the outcomes and the findings of the numerical and experimental work, answers the research questions and provides

recommendations such as design modifications on some critical engine components for future research.

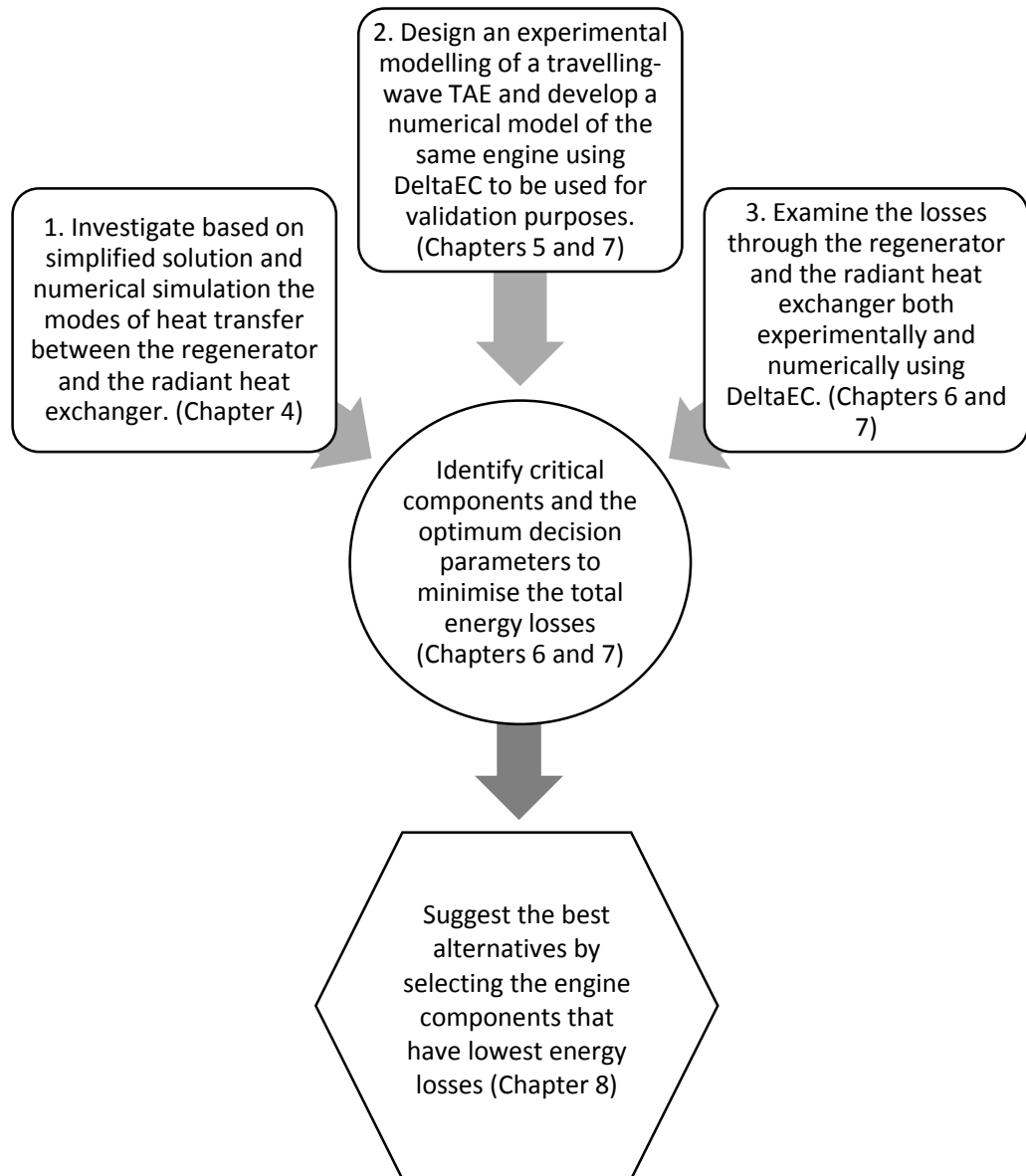


Figure 1.7: Relationship chart that describes the main research activities in chapter 4 through chapter 7.

Chapter 2

Literature Review

2.0 Introduction

Before presenting the details of this research, this chapter reviews and discusses some of the relevant previous research work. This chapter is divided into five main sections. The first section reviews the previous work done by SCORE™ project including the most recent effort made on the investigated WHTAE in this study [8]. The literatures related to the energy dissipation in the engine's components including the regenerator, resonator, radiant heat exchanger, taper and cones are then presented. In order to have a better understanding of the TAE working in travelling-wave conditions, previous work regarding engines that operate in travelling-wave phasing are also included. In addition, the reviewed literatures about the numerical modelling of travelling-wave TAEs using DeltaEC (Design Environment for Low-amplitude ThermoAcoustic Energy Conversion) [47] are also included in this chapter. The final section presents the studies related to different microphone techniques used to determine the acoustic properties.

2.1 SCORE™ Project

The WHTAE investigated in this study was first designed by a European research consortium led by the University of Nottingham, UK named SCORE™ which is

one of the leading thermoacoustic research projects that aim at designing a low-cost thermoacoustic electricity generator for the use in remote areas of developing countries, where waste heat is obtained from biomass burning (wood, charcoal, sawdust, etc) for cooking applications can be used for generating electricity to improve the quality life of rural communities [7, 48]. SCORE™ has successfully demonstrated the potential development of low cost TAEs for rural areas in the past few years.

Yu et al. [33] carried out an experimental investigation on pre-prototype SCORE™ engine which uses the looped-tube travelling wave configuration to convert thermally induced acoustic power to electricity using loudspeaker as an alternator. Pressure measurements were performed on the two sides of the alternator diaphragm. Simple temperature measurements were also carried out in the regenerator. For a heat input of 800 W, the measured oscillating pressure and temperature difference across the regenerator were 5667 Pa and 231 °C respectively. An electrical output of 5.17 W was achieved with a corresponding system efficiency of 0.65%. Their work was extended by removing the secondary CHX and placed an insulation blanket to reduce heat losses at the regenerator region [49]. At the input heating power of 703 W, the pressure amplitude was 7016 Pa and the temperature difference across the regenerator was 570 °C. The tested engine was able to produce 11.58 W of electric power. A record of thermal-to-electric efficiency of 1.65% was accomplished. Chen et al. [8] conducted experimental work on the latest SCORE™ TAE which utilises the waste heat from biomass to generate electricity. Pressure amplitude was measured near the regenerator in the engine and few temperature measurements were taken near the HHX. The flame temperature was between 750 to 1000 °C when the engine generated 22.7 W of electricity under the pressurisation of 50 kPa gauge by consuming 7 kW thermal heat from 1.5 kg of wood which corresponds to an overall system efficiency of 0.3%.

These studies worked merely on the overall design and testing of the TAE. There is still insufficient information regarding the individual component of the engine.

Few researchers were focused on the improvement of the SCORE™ engine performance by optimising the linear alternator which converts the thermally induced acoustic energy to electricity. Yu et al. [50] investigated the characterisation of the performance of audio loudspeaker as a linear alternator on the acoustic-to-electric efficiency. The aim was to consider cheap linear alternator such as a commercial available audio loudspeaker to be installed in the SCORE™ engine. Their work only took into consideration the important parameters related to the tested alternator such as the stiffness, electric inductance and mechanical resistance of the alternator. Saha et al. [51] also worked on the linear alternator for the SCORE™ engine. Some of the design issues of the linear alternator for SCORE™ project were addressed and based on cost and efficiency perspective, several advantages of the double Halbach array alternator structure over the commercial loudspeaker were discussed. It was found that double coil structure with a smaller number of coil turns would be suitable for the SCORE™ engine. However, no particular attention was paid to the rest of the components in the engine.

Moreover, Wee et al. [52] investigated the wave propagation through the bends in a looped tube system representing sections of the SCORE™ engine by using Particle Image Velocimetry (PIV) measurement technique. They managed to correlate the acoustic transmission power loss with the acoustic dean number and found that below a critical dean number of 1.3, the losses through the bend increase in a reasonably linear fashion. Wee et al. [53] made another contribution to SCORE™ project by proposing a PIV based wave decomposition technique to analyse the acoustic waves propagating through ducts. However,

the tested system was made without the presence of a regenerator and heat exchangers. Their research works were mainly concentrated on the analysis of pure acoustic, the thermodynamic process was not taken into account. All the research work done by SCORE™ did not include a comprehensive analysis of the regenerator and the heat exchangers especially the heat transfer process from the external heat source to the regenerator which will greatly influence the overall performance of the engine.

2.2 Losses in the Thermoacoustic Engine

TAEs have many promising applications and advantages over traditional energy recovery systems. Although the investigated WHTAE has the potential for long-life with high stability and reliability but there are few existing engineering issues that need to be solved in order to enhance the overall efficiency of the engine. The studies related to the losses in the engine remain as one of the areas of intense research interest that has not been done so far. Hence it is necessary to find solutions to improve the performance of the engine by reducing the acoustic energy dissipation. There are several mechanisms of acoustic losses that take place in the TAE. Different open area of components (heat exchangers and regenerator), change of cross-sectional area of tubes, inner surface of resonator wall that is opened for acoustic flow and acoustic streaming losses at the bends can have significant impact on acoustic wave propagation. In essence, the losses in the regenerator are generally due to the interaction between the solid plate of the regenerator and the adjacent fluid. The energy dissipation in the resonator is because of the friction loss between the oscillating acoustic waves and the resonator walls. The losses in the RHX are mostly due to the reflected component of the acoustic wave when it passes through the narrow channels of the RHX.

2.2.1 Energy Dissipation in the Regenerator

It is intuitive that the losses dissipated in the engine are mainly contributed by the thermoviscous losses in the regenerator. Despite the amount of useful work could be increased by using more regenerator layers but attenuation would be increased at the same time. Therefore the regenerator length must be chosen wisely by compromising between amplification and attenuation effects. Regenerators for thermoacoustic applications have been studied for many years but most of reported literatures fall into the cryogenic systems, where the regenerators are used in Stirling Cryocoolers. Bassem et al. [37] numerically optimised the regenerator in a travelling-wave thermoacoustic cooler. About 20% of Carnot coefficient of performance (COPC) was accomplished at the optimised values of regenerator radius and position when the temperature was 265 K at the CHX. Ueda et al. [54] also performed numerical investigations on the optimisation of the regenerator in a travelling-wave TAR. The results revealed the value of COP with the optimised parameters (regenerator installation position, length and hydraulic radius) exceeded 60% of the COPC. Tao et al. [55] numerically investigated the fluid flow and the heat transfer of the regenerator in an orifice pulse tube refrigerator (OPTR). It was reported that the regenerator geometric parameters and the regenerator material properties have significant effects on the cooling power of the OPTR. Nevertheless, these studies only discussed the optimisation of the regenerator by means of changing the geometry, the material and the dimensions of the regenerator. Mitchell et al. [38] developed a numerical expression which measures the heat-transfer effectiveness per unit flow resistance of the regenerator. The published results revealed the importance of the regenerator thermal mass and concluded the etched stainless steel foil regenerator which has a structure similar to parallel-plates works best for Cryocooler applications. Despite the effect of temperature was

considered but there is still lack of understanding and discussion concerning the acoustic field and the mechanisms of acoustic losses in the thermoacoustic device.

There are also studies and investigations conducted on regenerators used for travelling-wave TAEs. Some of the outstanding studies are highlighted in this review. Yu et al. [56] conducted experiments on a small-scale thermoacoustic travelling-wave engine to investigate the impact of hydraulic radius of a stacked-screen regenerator using helium and nitrogen as working gases. The experimental results showed that the ratio of the penetration depth over the hydraulic radius and the resonator length play important roles in controlling the onset temperature of the engine. It is worth noting that the explanation presented on the regenerator was not detailed enough as how the change in temperature will affect the boundary layer thickness of the regenerator. Backhaus and Swift [57] carried out experimental investigation on a parallel-plate regenerator which has similar dimensions to the tested screen-based regenerator in a TASHE [58]. A nearly double of acoustic power output was achieved when a parallel-plate regenerator was chosen. Their work highlighted the importance of understanding the thermally induced acoustic field mechanism in the regenerator and suggested this as future work. Furthermore, Wang et al. [39] studied the temperature evolution of the regenerator in the onset and damping processes in a travelling-wave TAE by applying infrared imaging technique. The experimental results indicated that the temperature distribution in the regenerator will be affected by the Geodeon streaming which appears in the oscillating flow when there is a loop. Ding et al. [40] established an experimental system to quantify the proposed theoretical model of regenerator based on linear thermoacoustic theory. Both published experimental and theoretical results demonstrated that the output acoustic work of the engine can be greatly affected by the geometric properties of the

regenerator. Several researchers experimented on the low-cost regenerator materials selection from the point of view of their sustainability and suitability in the design of thermoacoustic travelling-wave engine. Abduljalil et al. [59] tested the performance of the regenerator experimentally based on the onset temperature difference and the acoustic power output as a function of mean pressure. It was found that mesh-screen regenerator outperformed other tested materials and cellular ceramics may be an alternative to traditional regenerator materials to reduce the overall system costs. Gheith et al. [60] also added knowledge to the field by conducting an experimental study on the different of regenerator materials. It was reported that the regenerator materials have significant effect on the TAE performance. The research on the regenerator is dominated by quantitative studies about optimisation, and there is a lack of qualitative knowledge related to the loss mechanisms and the acoustic field in the regenerator.

2.2.2 Energy Losses in the Resonator

Another interesting component in the thermoacoustic devices that generates acoustic energy which is dissipating along the whole waveguide would be the resonator. The resonator in a thermoacoustic device is used to confine the pressurised working fluid and to determine the operational frequency of the system. Designers usually have the objective to design lower losses in the resonator at the resonance frequency. Efforts were also made on studying the resonator but these are relatively limited compared to the studies done on the regenerator. It was reported that resonators of alternative form can improve the overall performance of the TAE in terms of pressure amplitude. Zink et al. [61] discussed the influence of a curved resonator on the TAE using CFD analysis. The numerical results showed that a severely curved resonator will exhibit a variation in operating frequency and the pressure amplitude of the

acoustic waves. However, the investigation was carried out on a stack-based thermoacoustic device where the acoustic flow behavior was examined in a standing-wave condition. Yu et al. [62] demonstrated that the resonator accounts for one of the main factors that strongly affect the pressure ratio and onset temperature of the TASHE. By optimising the resonator diameter and length, the tested engine was able to achieve a pressure ratio of 1.40 and onset temperature of 73 °C using nitrogen as the working fluid. Zhou et al. [63] suggested that the diameter of the resonator plays a more important role than that of the length in determining the performance of a miniature TASHE based on their simulation and experimental results. Their work managed to accomplish a pressure ratio of 1.116 by optimising the radial dimension of the resonator which is sufficient to drive a refrigerator or a linear electrical generator using helium as the working gas. Several researchers carried out investigation on the performance of TAEs using two types of resonator designs: tapered and iso-diameter resonators [64-66]. It was found that the losses in tapered resonator were lower than that in the constant-diameter resonator. However, the physics behind the losses generated by different resonator geometry is not well discussed and understood yet. The authors of the current study presented an experimental investigation on the energy losses through different resonator geometries in order to enhance the TAE footprint [67, 68]. It was reported that Coiled resonator had the highest losses and the least losses was found to be the straight resonator. The authors of this study suggested to use multi-microphone method to improve the accuracy of the results obtained.

2.2.3 Energy Dissipation in Tapers and Cones

Most of the thermoacoustic devices use tapers or cones to connect the tubes together as well as to reduce acoustic streaming. Despite, the losses dissipated in these components are minor but they are also important as a whole in order

to improve the overall performance of the engine. However, the minor losses in oscillating flows due to the sudden change of tube area (tapers or cones) are much less understood because the research works in this particular area are extremely limited. Zhang et al. [69] conducted both theoretical and numerical analysis of minor losses through a duct with sudden change of area. It was found that the losses through the sudden area change are affected by the phase difference between the pressure and velocity. It is worth noting that this study can be deemed as the only relevant literature focusing entirely on the losses due to sudden change of tube area.

2.2.4 Energy Losses in the Radiant Heat Exchanger

The WHTAE used by the SCORE™ project is externally heated via a radiant heat exchanger which makes it very unique and different from the other existing thermoacoustic devices. It is paramount important to deliver most of the heat at the top layer of the regenerator for best performance of the engine. However, this influencing factor remains as one of the priority areas of concern that has yet to be explored. To date, there is only one study related to the investigation of the RHX in the TAE. Two different SCORE™ engine prototypes were tested using different types of radiant heat exchanger by Chen et al. [8]. Their work concluded that the latest wood-burning thermoacoustic generator which was equipped with convolution radiant heat exchanger produced more electric power than the propane-driven thermoacoustic generator which used bulge radiant heat exchanger for heat transfer. However, both TAEs were tested under different operating conditions especially the total heat input for both engines which were not the same. Chen et al. [36] also addressed in their work the importance of the topic of radiant heat exchanger and suggested it to be the focus of future research.

All the previous investigations are undoubtedly valuable addition to better understanding of the thermoacoustic devices, but the studies reported to date are mainly focusing on the optimisation of the regenerator and the resonator without taking into considerations some of the important issues. One common trait of all the previous optimisation efforts is that the acoustic fields pass through the regenerator and the loop (or bends) were not well explained. It should be noted that this study provides a more compressive discussion on the acoustic field and the loss mechanisms between the regenerator and the sharp bend (torus-like section) than previous studies.

2.3 Travelling-Wave Thermoacoustic Engine

The investigated TAE is a waste-heat driven travelling-wave engine which utilises the waste heat from a cooking stove to create travelling acoustic oscillations through a closed loop [41]. Yazaki et al. [70] demonstrated a toroidal-shape travelling-wave TAE. Backhaus and Swift [21] published a detailed experimental study of a travelling-wave TASHE comprising a looped tube connected to a long standing-wave resonator. Tijani and Spoelstra [71] designed and built the same type of TASHE and achieved a new record performance of 49% of the Carnot efficiency. Blok [72] designed a looped tube TAE but with two bypass feedback loops. The thermally induced acoustic waves were circulating in loops. Blok [73] also constructed and tested a hybrid configuration of a travelling-wave TAE with only one bypass feedback mechanism connected at the centre of the torus.

All the literatures mentioned beforehand were intentionally designing the engine to be travelling in a looped manner. The travelling-wave condition could also be created by means of stub-tuning technique. Chen et al. [8] designed and constructed a propane-driven travelling wave thermoacoustic generator.

They added the so called “tuning stub” to the engine which is essentially an additional tube installed perpendicular to the feedback loop in a position close to the thermal buffer tube of the system. The stubs were used to adjust the impedance matching between the acoustic load and the linear alternator thereby to obtain a better travelling-wave condition. Yu et al. [74, 75] proposed a travelling-wave thermoacoustic electricity generator with a linear alternator connected in the engine. The alternator introduces an acoustic load in the engine that alters the acoustic field which leads to acoustic reflections. An acoustic stub was also introduced and attached to the wave guide at a location close to the load. By applying this stub-matching technique, the preferred travelling-wave phasing was obtained and the acoustic impedance caused by the alternator was cancelled out effectively.

Besides stub-tuning method, the desired travelling-wave condition could also be obtained by using load components. Gardner and Swift [76] integrated a standing-wave and two travelling-wave engine in series. They utilised six load components (LC and RC components) which are essentially ball valves used to adjust the inertial and compliant impedances in order to create a travelling-wave phasing. Blok [77] designed a multi-stage TAE by placing four regenerator units in series in a travelling-wave feedback system. The regenerator units were placed on a mutual distance of quarter acoustic wavelength so that reflections due to impedance anomalies will compensate each other [78]. Meanwhile, an acoustic load was added at each stage of the engine to act as an energy converter as well as to obtain a preferred travelling-wave condition. Wee et al. [52] experimented a travelling-wave engine using two loudspeakers. One speaker was used as an acoustic excitation source and the other speaker acted as a linear alternator. The travelling-wave phasing was achieved by tuning the resistive load on the coils of the linear alternator so that the termination impedance could match with the waveguide impedance in the engine.

In addition, the desired travelling-wave mode could also be created by employing an anechoic termination in a system which was rarely reported in the literatures. This passive attenuation of acoustic waves were developed by using absorbing materials. Nevertheless, many studies related to anechoic termination were working in the frequency range of the order of tens of kHz of frequency, the lower frequency range investigated by some researchers were typically a few hundreds to few thousands of Hz of frequency [79-81], still falls far away from the interesting zone for the low frequency TAE which is operating in a frequency range of only 40-150 Hz [8, 36].

2.4 Numerical Simulation of the Thermoacoustic Engine

DeltaEC is a differential equation solver that integrates one-dimensional acoustic wave equation over any user-defined geometry with a user-selected working fluid. The DeltaEC software utilises an iterative shooting method to find a solution for the unknown variables (guesses) based on the known variables (targets) specified by the user. Since the release of the Los Alamos thermoacoustic code, DeltaEC software [82], which is distinctly different from the text-based program that was first made available in 1993 [46], there has been studies demonstrating the usefulness of this software as a tool to design and model the thermoacoustic devices. The DeltaEC simulation efforts reported to date were mainly focusing on standing wave thermoacoustic devices where a HARDEND segment was used as the termination end. By comparison, the DeltaEC work on travelling-wave devices is still lacking especially on TAE category. Tijani and Spoelstra [83] employed DeltaEC to design and optimise a travelling-wave TASHE. The engine produced about 300 W of acoustic power with a performance of 41% of the Carnot performance based on the deduced acoustic power by extrapolation using the DeltaEC model of the system. However, high pressure helium was used as the working

fluid in their work which is very different from the current study. Sun et al. [84] studied numerically and experimentally the effect of different acoustic amplifiers on the performance of a travelling-wave TAE. An acoustic amplifier is basically a segment of tube with a designed length and diameter. Their conclusion was that the proposed cascade acoustic amplifier had a much higher pressure amplitude amplification and a lower acoustic power dissipation compared to the single-stage acoustic amplifier. Nevertheless, these numerical studies did not give clear information about the targets and guesses chosen for the tested model which are important to simulate the engine successfully.

In the past few years, DeltaEC had been fully utilised by Jaworski and colleagues to predict the system performance of the travelling-wave TAE. Abduljalil et al. [85] used DeltaEC software to investigate the output acoustic power of a travelling-wave TAE with ceramic regenerator. The experimental results were verified against the results obtained by DeltaEC and a good agreement was found. However, the results were obtained by assuming a pure travelling-wave condition which is not the normal case in TAEs. Yu and Jaworski [86] examined numerically the distribution of pressure amplitude and volume velocity as well as the phase angle along the regenerator by using DeltaEC. They simulated a travelling-wave TAE based on the published experimental results [21, 57] and used it to compare the performance of two types of regenerator: parallel-plate and stacked-screen. It was found that the viscous dissipation in the tested stack-screen regenerator was about 40 W more than that in the parallel-plate regenerator. However, the acoustic waves in the designed numerical models were branched out and then united back into the engine again in order to create a perfect travelling-wave condition. Few years later, in collaboration with Backhaus [74], again employed DeltaEC software and proposed a travelling-wave thermoacoustic electricity generator. Based on the numerical results obtained, the engine was able to produce 10.3 W of electricity with an

input heat power of 434 W by making use of a linear alternator. Nevertheless, most of the reported numerical studies relied on the assumption of operating the TAE in a pure travelling-wave condition. In reality, owing to the presence of regenerator, the engine works in a neither a pure standing-wave nor a pure travelling-wave conditions. DeltaEC has been widely used by researchers in the thermoacoustic community and is proven to predict accurately the performance of thermoacoustic systems.

2.5 Acoustic Measurements

2.5.1 One-Microphone and Two-Microphone Methods

The well-known standing wave impedance tube method makes use of the measured standing wave ratio (SWR) for a specific frequency in the tube to determine the acoustic properties by means of only a movable microphone. An advantage of this method is that it is not necessary to calibrate the microphone. The disadvantages to this method are the complex setup with a movable probe and time needed to find the location of the maximum and minimum pressures for each frequency of interest [87]. An alternative way to measure the acoustic properties by using two microphone systems which require two similar microphones, fixed and phase-calibrated at different positions in the tube with a known distance between them [88-90]. Seybert and Ross [88] proposed a different method for impedance tube measurements of sound absorption using the pressure measurement at two positions, called the two-microphone method, which was much faster than the conventional standing-wave-ratio method. The acoustic wave response is mathematically separated into its reflection and incident components using a transfer function between the microphones. This decomposition of wave propagation allows the computation of the acoustic properties such as reflection coefficient, absorption coefficient

and acoustic impedance. Figure 2.1 illustrates the SWR technique and two-microphone method.

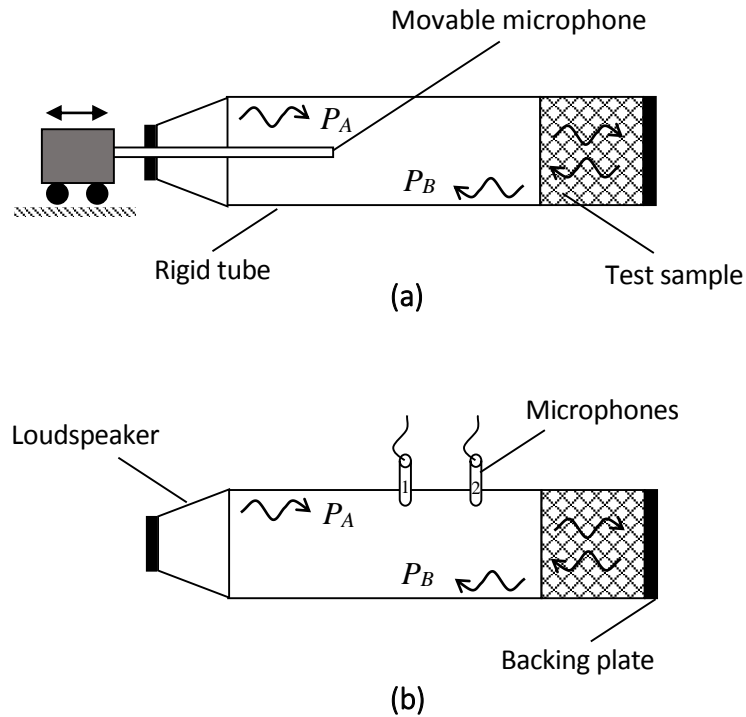


Figure 2.1: Schematic representation of (a) standing wave ratio technique and (b) the two-microphone method.

Chung and Blaser [88-91] further developed this method experimentally and later Chu [92, 93] also improved the method by including the tube-attenuation effect, allowing the microphones to be placed far away from the sample. Boden and Abom [94] studied the two-microphone method by using numerical simulations and found that this method has its lowest sensitivity when the two microphones are separated by a quarter acoustic wavelength. The influence of errors in the two-microphone method has been investigated [95-97]. Chu [98] has proven in order to yield accurate results, one of the microphones has to be placed closer to a the minimum pressure location while the location for the other microphone is not as critical as long as the separation is not close to a

half acoustic wavelength. The primary advantages of the two-microphone method are the significant time saving, no moving parts required, and its excellent suitability to quick response with a random noise source. The drawbacks are that its accuracy significantly degrades at large acoustic wavelengths (low frequencies) and at microphone separations near one-half acoustic wavelength (high frequencies). The two-microphone method has the added problems of requiring highly accurate microphone calibration [99].

2.5.2 Multi-Microphone Method

There is a more recent acoustic properties measurement method utilising more than two microphones to carry out the measurements. This multi-microphone method, on the other hand, yields better results in the low frequency region. Chu [100] and Jones [101] described an alternative multiple-microphone method, a least square method on the pressure measurements at more than three positions. The multi-microphone method has also no restriction on microphones separation relative to acoustic wavelength and allows results to be plotted with a single line based on the transfer function of a few microphone combinations. Jang and Ih [102] theoretically and experimentally studied the influence of the microphone positions on the accuracy of the multiple-microphone method. They found that using equidistant positioning of microphones reduces errors within the effective frequency range. Moreover, they showed that the measurement accuracy can be increased and the frequency range can be widened by increasing the number of equidistant microphones. Another recent improved method uses least squares curve fitting to optimize the response of all the microphone positions to produce a result with minimum error [43-45].

2.6 Concluding Remarks

The general review of the published literatures related to this research revealed that there are many interesting questions yet to be answered by the researchers in these areas. Some of the important issues and questions that need to be understood will be addressed in this work. In order to fill the gaps in the existing knowledge of literatures, this study will investigate an air-operated TAE under low frequency and low pressure condition (atmospheric pressure). Below are the important points to be highlighted in the current study:

- All the research work done by SCORE™ project did not include a comprehensive analysis of the regenerator and the heat exchangers especially the heat transfer process from the RHX to the regenerator which will greatly influence the overall performance of the engine.
- The research on the regenerator and the resonator is dominated by quantitative studies about optimisation, and there is a lack of qualitative knowledge related to the loss mechanisms and the acoustic field in the regenerator and the resonator.
- It is worth noting that the study about the energy dissipation through tapers and cones reported can be deemed as the only relevant literature focusing entirely on the losses due to sudden change of tube area.
- The travelling-wave mode could be created by employing an anechoic termination in a system which was rarely reported in the literatures especially in the interesting zone of the low frequency range of only 40-150 Hz.

- DeltaEC has been widely used by researchers in the thermoacoustic community and is proven to predict accurately the performance of thermoacoustic systems.
- After an overview of different microphone techniques, the multi-microphone travelling-wave technique is found to yield accurate results especially in the low frequency range. The multi-microphone least squares technique with the aid of impedance tube measurement method can produce a result with minimum error.

2.7 Research Questions

After reviewing the literatures, there are some underlying issues or questions that need to be addressed and answered in order to accomplish the objectives of this study. A total number of ten research questions are identified:

- Q1) What is the most important heat exchanging mechanism and how do the different modes of heat transfer affect the performance of the engine?
- Q2) What would be the best option for the design of the RHX in the TAE, bulge or convolution?
- Q3) Which method is better to attenuate the acoustic wave to produce a desired travelling-wave condition in an open loop at low frequency?
- Q4) How the amount of incident and reflected components in the acoustic field influence the efficiency of the engine?

- Q5) What is the effect of the regenerator configuration on the acoustic losses?
- Q6) How the current loop design at the driver side influence the energy losses in the engine?
- Q7) How much energy dissipation in the complete setup of the engine compared to an equivalent straight tube ideal condition?
- Q8) Is the loss in the engine affected by the change of temperature of the HHX?

Chapter 3

Methodology

3.0 Introduction

This chapter summarises the research methodology used in this study. Firstly, the steps of the simplified solution and the numerical simulation of the heat transfer between the regenerator and the RHX are discussed. The second section deals with the methodology of the experimental modelling of the travelling-wave TAE. The steps of the experimental study of the acoustic energy losses through the regenerator and the RHX are then presented. It then goes on to describe the numerical modelling of the WHTAE. In the final section of this chapter, a flow chart of the overall methodology is displayed to describe the flow of the activities of this research work.

3.1 Simplified Solution and Numerical Study of the Heat Transfer between the Regenerator and the Radiant Heat Exchanger

In order to enhance the efficiency of the WHTAE, which is crucial for maximising the overall engine performance, it is important to supply most of the heat to the engine directly at the regenerator top surface. In this study, two modes of heat transfer, convection and radiation are under examination. The

investigation of the heat transfer process between the regenerator and the RHX (bulge or convolution) is conducted in two consecutive stages.

Radiative heat transfer has been deemed to be of particular importance in the engine which is expected to have direct effect on the performance of the engine. In the first stage, the view factor analysis is used to study the radiative heat transfer in the engine. The radiation study is done by dividing the convolution channel into smaller sections A, B, and C. Two virtual planes which have flat surfaces are created in these sections. The radiation analysis for the bulge is less complicated because it consists of only two surfaces. Figure 3.1 shows the two-dimensional representation of the two RHXs. The contribution of radiation percentage from each surface from the RHX to the regenerator is then obtained.

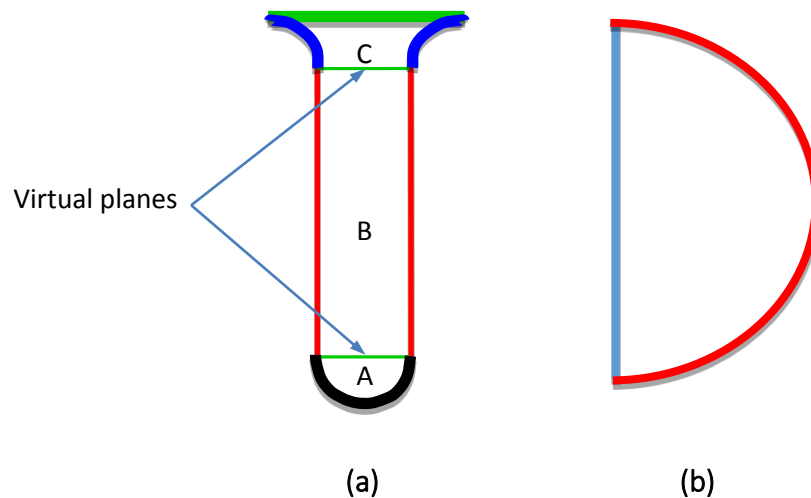


Figure 3.1: Two-dimensional representation of (a) convolution and (b) bulge in the view factor analysis.

The coupled heat transfer effect and the temperature gradient from the RHX to the regenerator top surface are studied numerically in the second stage. There are four different cases, each one of them represents a different geometry in terms of variation of mesh and size. A three-dimensional model of

the bulge is proposed and created in GAMBIT software. The bulge model is further developed into three additional geometries which have different RHX designs including the convolution model. The geometries of the first bulge model and the convolution model are the same as the aforementioned bulge and convolution design used in the SCORE™ project. The simulated space consists mainly of two regions; one is the porous zone (regenerator) and the other is the RHX region. The simulations are conducted using the commercially available Fluent Software 6.3 [103]. User defined functions (UDFs) are developed in C programming language to define periodic boundary conditions. A suitable turbulence model is selected to account for the fluid flow in both the porous media and the RHX regions. The CFD numerical results are compared with the simplified solution results of the radiation heat transfer for the bulge and the convolution for validation and better understanding. The methodology flow chart for the investigation of heat transfer between the regenerator and the RHX is displayed in Figure 3.2. The simplified solution and numerical modelling of the heat transfer processes will be detailed in chapter 4.

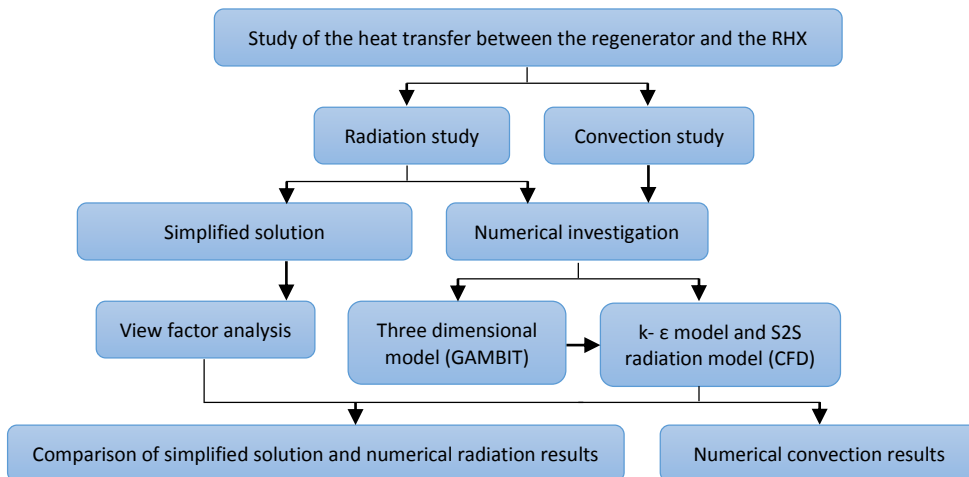


Figure 3.2: Flow chart of the methodology used for the investigation of heat transfer between the regenerator and the RHX.

3.2 Experimental Modelling of a Travelling-Wave Thermoacoustic Engine

This study develops an experimental modelling of a TAE that works in travelling-wave mode by using a passive attenuation technique. A speaker is used to emit the sound waves at one end of a straight tube, different materials or combinations are placed at the other extremity of the tube in order to experimentally obtain a travelling wave in an open loop, simulating the conditions of the engine while being able to control the frequency and amplitude of the wave. The sound absorption coefficient is an important indicator which can effectively determine how much sound energy is dissipated and reflected back.

The multi-microphone least square technique is employed in conjunction with the impedance tube measurement method [43-45] to determine the acoustic properties of the tested absorbing materials. Eight different types of absorbing materials and combinations are tested. Experiments are conducted using a source of uniform white noise and repeated with a Gaussian white noise having a wide frequency band. The research activities carried out here are connected to the methodology used in the following sections as shown in Figure 3.3. The experimental modelling of a travelling-wave thermoacoustic engine will be detailed in chapter 5.

3.3 Losses through the Regenerator and the Radiant Heat Exchanger

The experiments of the acoustic energy dissipation in the regenerator and the resonator in association with the RHX are conducted by setting up two different

configurations. A straight tube configuration was first considered to investigate the losses in the regenerator. The experiments are taken under two different conditions: ambient and hot conditions. In the second set of the experiments, a more complicated setup, RHX configuration was used and the experiments are repeated using the same settings and conditions but the heating element is mounted on the RHX externally. In order to investigate the acoustic energy losses through the RHX, the experimental examination is carried out by changing the types of RHX (bulge or convolution) while fixing the thickness of the regenerator.

Acoustic energy loss is an important indicator that can effectively determine how much sound energy is dissipated through the regenerator and the RHX. The dissipation of acoustic energy through the regenerator and the RHX is obtained by employing the multi-microphone travelling-wave technique [100-102]. Analysis of the acoustic field is implemented by using Womersley number and standing wave ratio (SWR) to further understand the energy losses in the thermoacoustic system. The previous methodology is linked to the current research activities as depicted in Figure 3.3. The study of the acoustic energy dissipation through the regenerator and the RHX will be detailed in chapter 6.

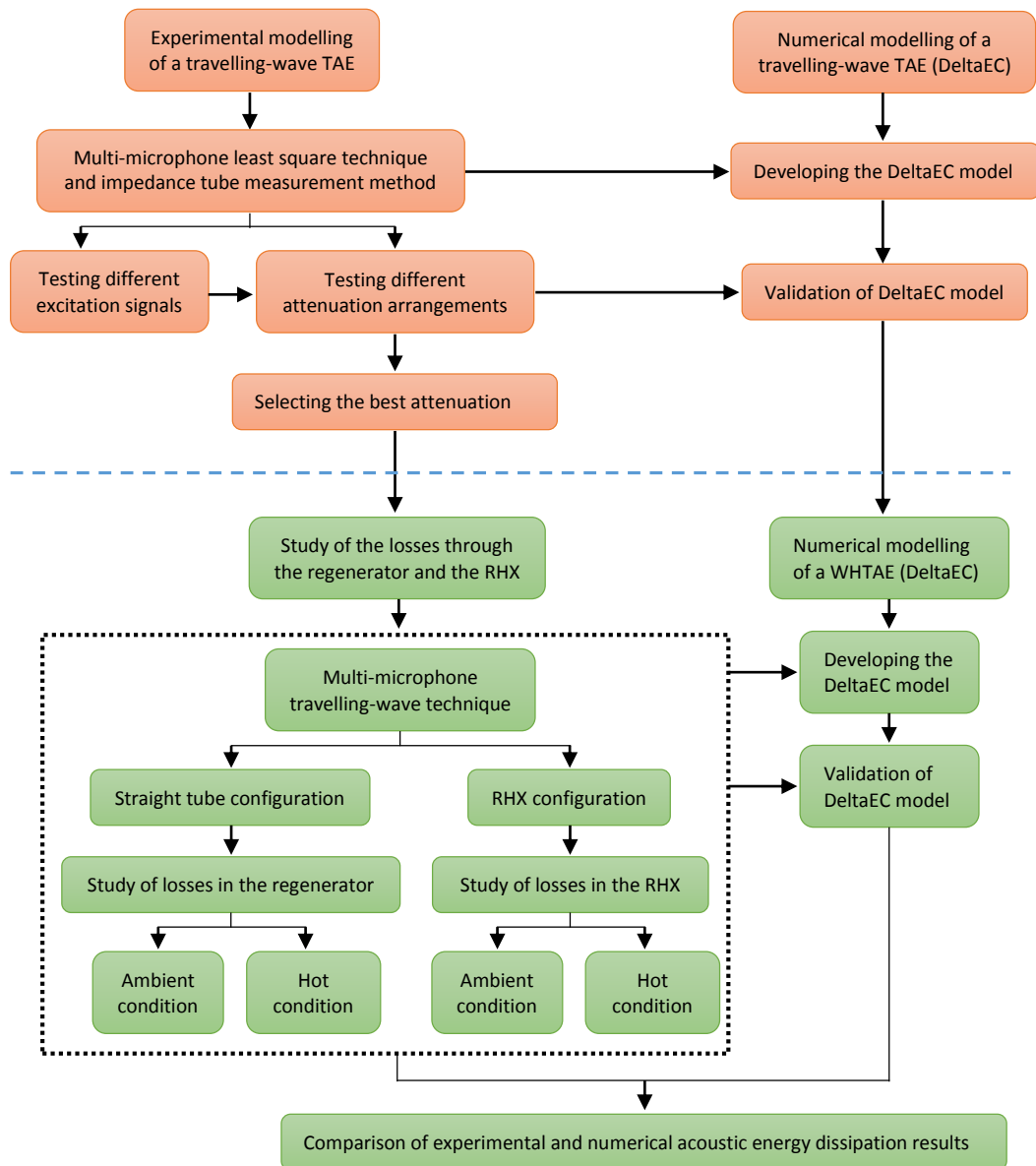


Figure 3.3: Flow chart of the methodology used for the investigation of the passive attenuation and the losses of the engine components.

3.4 Numerical Modelling of the WHTAE

DeltaEC is fully utilised to model similar setups as the ones used in the experimental investigations. The design of the DeltaEC models is divided into two stages. The first stage is the DeltaEC modelling and simulation of the attenuation effectiveness. The second stage consists of the numerical

modelling of the acoustic energy dissipation in the WHTAE. The DeltaEC models for the acoustic energy dissipation experiment have two different configurations: straight tube and RHX configurations. The former model is basically the same as the designed model in the absorption coefficient experiment except now a regenerator which is sandwiched by two heat exchangers is included for investigation. On the other hand, the latter model comprises a compliance volume near the regenerator which is used to indicate the volume of the RHX. The methodology used in this section is connected with the steps undertaken in the previous sections as shown in Figure 3.3. The DeltaEC results are compared against the experimental results and the validated DeltaEC model will be used to help on the design of future prototypes and for better optimisation of the TAEs.

3.5 Flow Chart of the Research Activities

The overall methodology is shown graphically in Figures 3.2 and 3.3. The methodology flow chart for the investigation of the heat transfer between the regenerator and the RHX is displayed in Figure 3.2. Figure 3.3 shows the methodology used in the experimental modelling of a travelling-wave thermoacoustic engine and how it is connected to the methodology used in the experimental investigation of the losses through the regenerator and the RHX as well as the research activities carried out in the numerical modelling of the WHTAE.

Chapter 4

Heat Transfer in the Waste-Heat Driven Thermoacoustic Engine

4.0 Introduction

This chapter presents a detailed study of heat transfer in the SCORE™ TAE. The SCORE™ TAE is introduced at the beginning of this chapter. The second section deals with the heat transfer processes in the engine and identifies the important modes of heat transfer in the SCORE™ TAE which are mainly convection and radiation. The investigation of the heat transfer between the regenerator and the RHX (bulge or convolution) are conducted in two consecutive stages. In the first stage, a simplified solution study of the radiative heat flux distribution in the engine is under examination. The coupled heat transfer effect and the temperature gradient from the RHX to the regenerator top surface are simulated numerically and presented in the second stage. A comparison of results between the simplified solution and the numerical simulation are then discussed. These are followed by concluding remarks from this study as provided in final section.

4.1 SCORE™ Thermoacoustic Engine

SCORE™, one of the leading thermoacoustic research projects, has designed a number of TAEs powered by waste heat from cooking stoves [7, 48]. The main aim of SCORE™ is to design engines which have low manufacturing and maintenance costs in order to be used in rural area. One of important concerns about the SCORE™ engine is the thermal interaction between the RHX (bulge or convolution) and the regenerator; the description of the temperature field and the heat flux distributions inside the engine are the focus of investigation in this chapter. Figure 4.1 shows the schematic diagram of SCORE™ engine.

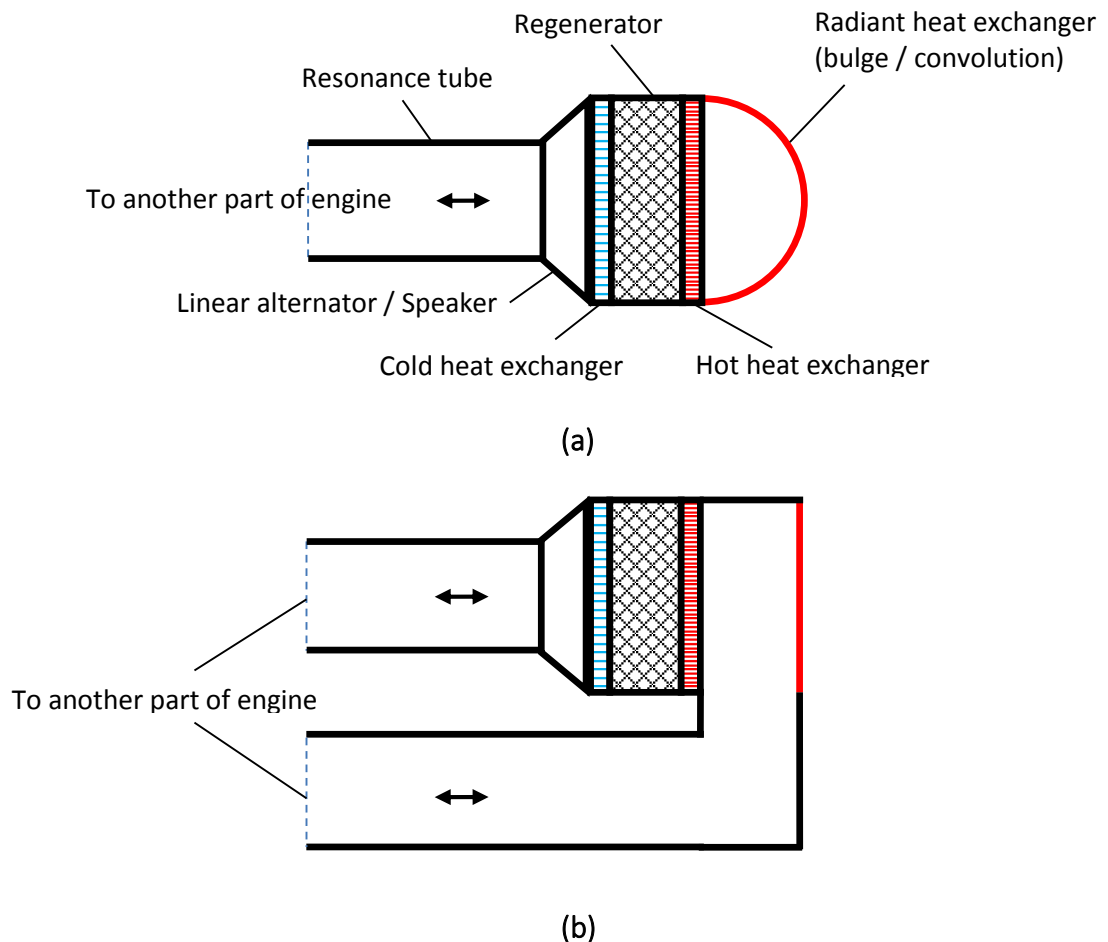


Figure 4.1: The (a) side view and (b) top view of the SCORE™ engine.

The overall performance of the TAE depends a lot on the efficiency of the heat transfer process from the cooking stove to the regenerator. It is important to supply most of the heat to the engine directly at the regenerator top surface. The combined and complex mode of heat transfer from the cooking stove to the engine makes this task extremely difficult to be achieved. Understanding this complex situation of heat transfer is necessary and essential for the optimization of the performances of the engine.

Radiative heat transfer has been deemed to be of particular importance in the engine which is expected to have direct effect on the performance of the engine. There are mainly two RHX designs considered for investigation under this study. The first one is the bulge design, which has a semi-circular surface, facing the flames by its convex side and facing the regenerator of the engine by its concave side. The second design is the convolution, which is a corrugated steel plate in fins like shape. It is believed that the higher the fraction of heat radiated directly to the regenerator and the lower the portion of heat transferred by convection through the adjacent air to the regenerator, the better the energy concentration at the regenerator surface. Therefore the more likely that Rayleigh criterion can be achieved effectively. Hence, heat transfer due to convection has great influence on the total heat transfer of the engine as well. Ignoring such mode of heat transfer may yield inaccuracies in estimating the overall heat transfer. This chapter discusses some important issues to be taken into consideration in order to maximize the amount of heat transfer to the top layer of the regenerator while minimizing the intrinsic losses. This investigation is one step towards optimization the heat exchanger design and selection for better convolution or bulge design.

4.2 The Challenge of the Heat Transfer from the Heating Surface to the Hot Heat Exchanger in the SCORE™ Thermoacoustic Engine

In an idealised TAE, the regenerator is sandwiched by two heat exchangers. Heat is supplied to the engine directly at the top layer of the regenerator by the hot heat exchanger (HHX) at one side and removed at the other side of the regenerator with the aid of the cold or ambient heat exchanger (AHX). This can be achieved easily when using electrical heating. Figure 4.2 shows the basic concept of a thermoacoustic driver with direct heating. An important feature to notice is that heat is supplied to the oscillating air inside the engine at a very short length as it is crossing through the HHX. In this configuration heat is transferred from the HHX to the air mainly by conduction through the tiny channels of the regenerator which are smaller than the thermal penetration depth. However, it becomes very challenging if the heat is transported from an external heat source as in the SCORE™ engine. For an externally heated TAE, it is not easy to design for the oscillating air to cross through the HHX. The external heat source in the SCORE™ project is burning wood or propane gas which can be difficult to accommodate inside the engine. As a result, a RHX (bulge or convolution) is introduced and installed to the engine. The arrangement of the components in the engine is different from the original concept illustrated in Figure 4.2. Instead of providing direct heat input to the regenerator, the heat energy is transported into the engine with the aid of the RHX to the top layer of the regenerator. Figure 4.3 demonstrates the two different configurations used by the SCORE™ engine.

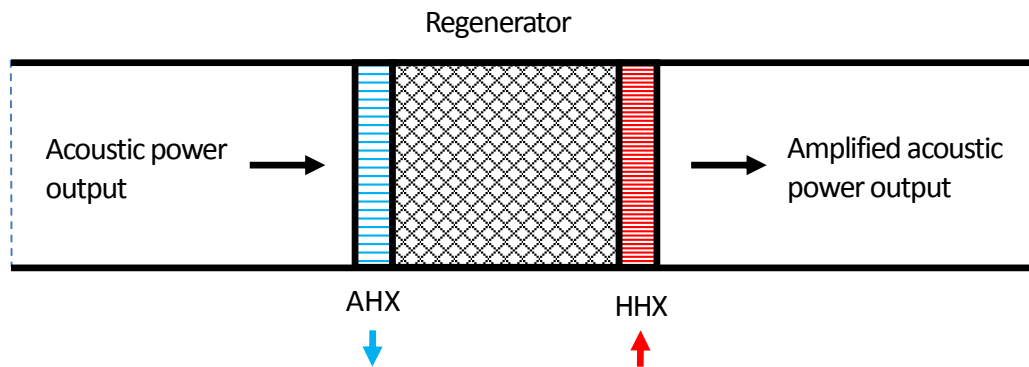
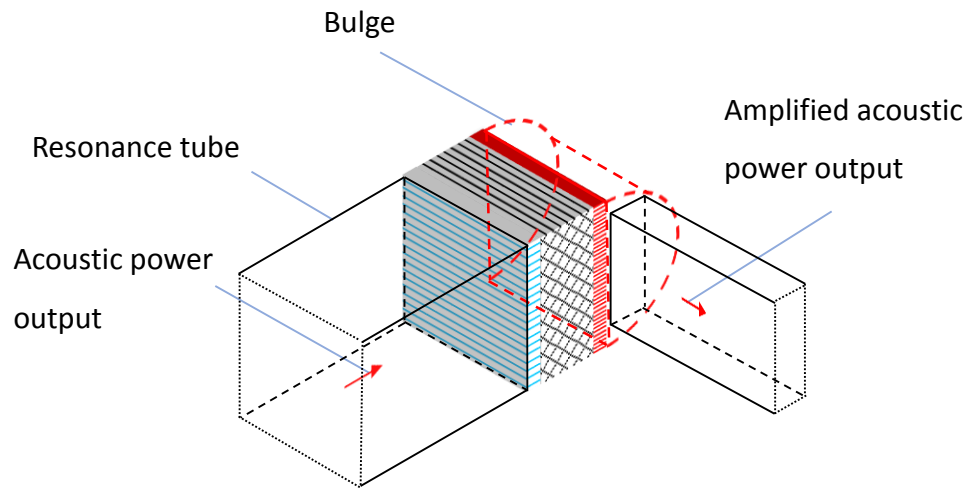
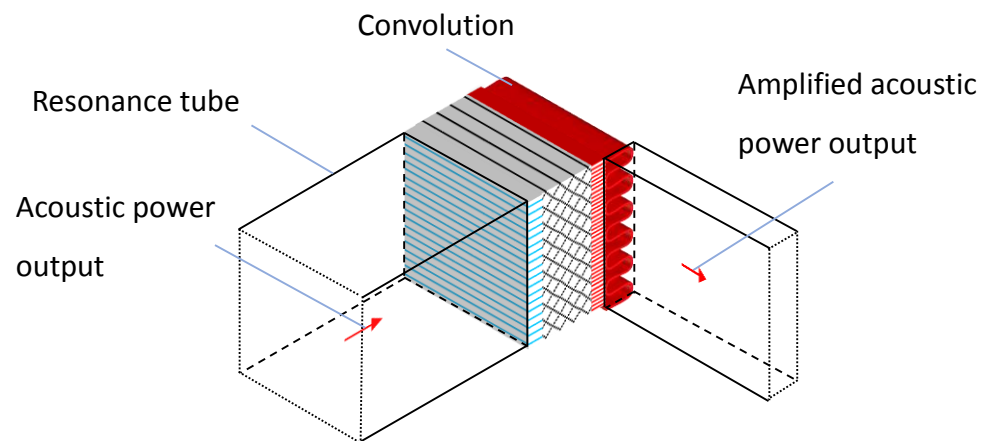


Figure 4.2: Basic concept of a travelling-wave thermoacoustic driver with direct heating at the two sides of the regenerator.

The bulge and convolution dimensions are constructed in such a way that both possess the same volume which is 0.00123 m^3 (based on real measurement of Demo 2.1 SCORE™ TAE) [8] but their overall surface area is different. The bulge has 0.0424 m^2 overall surface area whereas the convolution has an overall surface area of 0.231 m^2 . The regenerator dimensions for both the bulge and the convolution are the same; each of 200 mm length, 200 mm width and 10 mm thickness. The heat transfer from the bulge or the convolution to the regenerator is very complicated and believed to involve radiation and convection as well as conduction. This can be explained because when heat is transported from the RHX to the regenerator, the heat waves in the RHX region will transfer heat energy to regenerator by convection due to temperature difference and there is also heat transfer by electromagnetic radiation between the two surfaces. Because the regenerator is in contact with the convolution so heat is also transferred by conduction. The passage of the oscillating air through the HHX from the bulge or the convolution is also different in length. The cross-sectional area of the oscillating flow between the bulge or the convolution and the regenerator varies significantly between the two designs, it is important to study more in depth the heat transfer in these two configurations in order to improve the overall efficiency of the engine



(a)



(b)

Figure 4.3: External heating of the thermoacoustic engine through (a) bulge and (b) convolution.

4.2.1 Heat Transfer Processes in an Externally Heated Thermoacoustic Engine

There are mainly two types of heat transfer processes in the SCORE™ TAE. Firstly is the heat transfer between the external heat source (radiant heat exchanger) and the regenerator. The second process is the heat transfer between the heat exchanger (HHX or AHX) and the oscillating air through them. It is understood that the latter is mainly by conduction because the regenerator pores are smaller than the thermal penetration depth (acoustic thermal boundary layer), resulting in direct conduction of heat within the boundary layer of the air, making conduction to be generally more important in this region. The positioning and the definition of the HHX in the SCORE™ TAE are not exactly the same for the two different configurations as displayed in Figure 4.3. In the bulge type of the engine as shown in Figure 4.3 (a), the HHX is considered to be the first few layers of the regenerator. Although the inner side of the bulge itself is hotter than the few top layers of the regenerator, but it is relatively far away from the passage of the oscillating air. In the convolution type of the engine as depicted in Figure 4.3 (b), the HHX is bigger in volume. It consists of the top few layers of the regenerator plus the convolution itself. The air is taking longer passage through the hot zone of the convolution along the narrow hot channels of the convolution (convolutes).

4.2.2 Important Modes of Heat Transfer in the SCORE™ Thermoacoustic Engine

In the SCORE™ TAE heat is supplied to the engine at a surface far away from the top layers of the regenerator, resulting in big divergence from the idealised concept of the TAE. The presence of the space between the regenerator and the external heating surface is essential and crucially important for the

oscillating air in the engine so this space could not be eliminated. The thermal resistance network of this space for both types of RHXs are presented in Figure 4.4. It can be seen that the both types of engines (one uses bulge and the other equips with convection) are subjected by radiation and convection. In the convection type of engine, all three modes of heat transfer are involved including conduction because the convection is in contact with the regenerator. The convection possesses bigger surface area than bulge which leads to smaller thermal resistances therefore a higher contribution amount of heat transfer. However, the convolutes are relatively bigger compared to the thermal penetration depth and the mode of heat transfer is believed to be mainly by convection rather than conduction, with smaller amount of radiation to the regenerator.

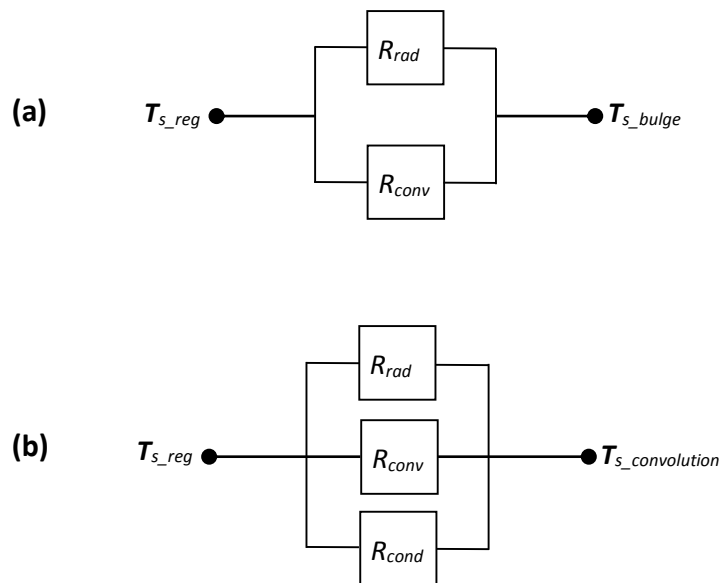


Figure 4.4: Thermal resistance network between the regenerator and the RHX: (a) bulge and (b) convection.

4.3 Analysis of Radiation Heat Transfer in the Bulge and Convolution

The flow of the oscillating air between the external hot surface and the regenerator results in significant heat convection which will harm the engine's performance. Radiation from the surface of the convolution or the bulge to the surface of the regenerator is the best way (in absence of direct conduction) to heat the top layers of the regenerator to a temperature higher than the adjacent oscillating air in order to have an amplification effect of the travelling wave. In the following sections radiation in the two configurations of the engine are evaluated and compared based on simplified solution.

4.3.1 View Factor calculations for the Convolution and the Regenerator Integrity

The view factor or the configuration factor for diffuse surfaces is a pure geometrical property and has nothing to do with the surface emissivity. The view factor F_{12} is defined as the fraction of the radiation leaving surface 1 that arrives at surface 2. An analysis can be done by dividing the convolution channel into smaller sections A, B, and C. Two virtual planes 2 and 4 which have flat surfaces are created in these sections as displayed in Figure 4.5. The contribution of radiation percentage from each section from the convolution to the regenerator is summarised in Figure 4.6 and the detailed calculations of the view factors for all the sections in the convolution by using the established correlations [104, 105] is shown in Table 4.1.

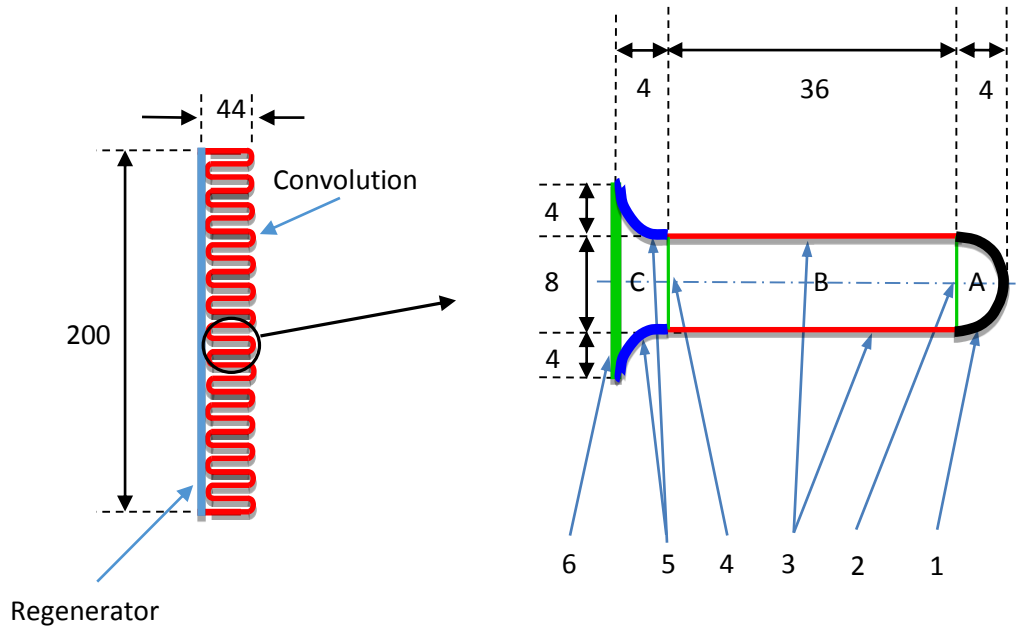


Figure 4.5: Divisions of one convolution element (convolute) for the view factor calculations (all the dimensions are shown in mm, not to scale).

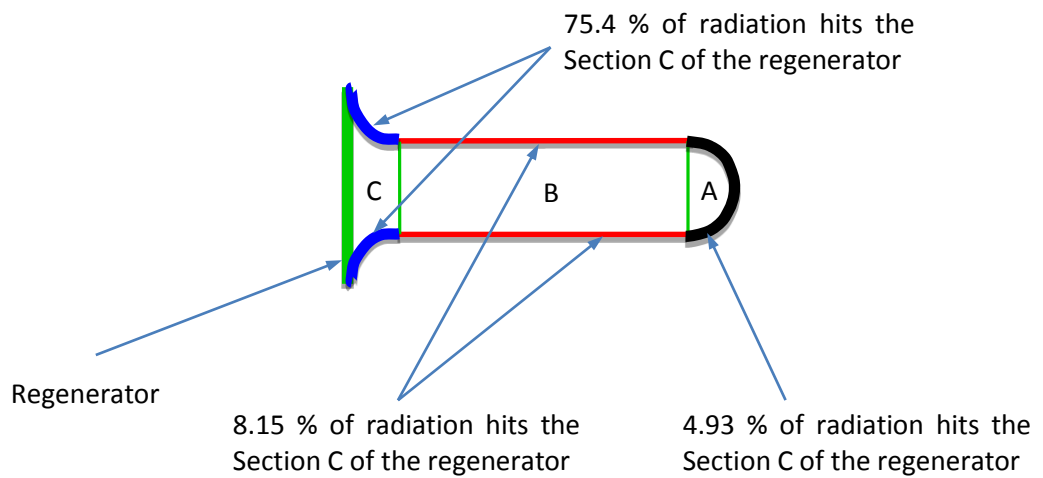


Figure 4.6: Percentage of radiation from each section from the convolution to the regenerator.

Table 4.1: The calculations of the view factors for all the sections in the convolutions.

Section	View factor
A (enclosed by surfaces 1 and 2)	<p>→ $F_{22} = 0$ and $F_{21} = 1$</p> <p>By using reciprocity relation:</p> <p>→ $A_1 F_{12} = A_2 F_{21}$ $4 \pi \times F_{12} = 8 \times 1$</p> <p>∴ $F_{12} = 0.637$</p> <p>Which means 63.7% of the radiation from surface 1 is crossing the virtual surface 2.</p>
B (enclosed by 2, 3 and 4)	<p>→ $F_{22} = 0$ and $F_{44} = 0$</p> <p>The view factors for the two aligned parallel rectangles 2 and 4 are found from [104] using the factors:</p> <p>→ $L_1/D = 200/36 = 5.55$ and $L_2/D = 8/36 = 0.222$</p> <p>Where L_1 and L_2 are the dimensions of the channel of the convolution, 200 mm and 8 mm respectively, and D is the depth of the channel, 44 mm.</p> <p>∴ $F_{24} = 0.095$</p> <p>→ $F_{22} + F_{23} + F_{24} = 1$ $0 + F_{23} + 0.095 = 1$</p> <p>∴ $F_{23} = 0.905$</p> <p>Due to symmetry,</p> <p>∴ $F_{43} = 0.905$</p> <p>By using reciprocity relation:</p> <p>→ $A_4 F_{43} = A_3 F_{34}$ $8 \times 0.905 = 72 \times F_{34}$</p> <p>∴ $F_{34} = 0.100$</p> <p>Which can be deduced that 10 % of the radiation from the vertical straight walls is crossing the virtual surface 4 towards the regenerator. Note that 63.7% of the radiation coming from the curved bottom surface is crossing the virtual surface 2, out of this only 9.5% passes to</p>

	the regenerator ($F_{24} = 0.095$), thus 6.05% of the radiation generated from the bottom curved surface can reach to the regenerator.
C (enclosed by 4, 5 and 6)	<p>The view factor between the two curved parts of this enclosure can be mathematically derived as [105]:</p> $\rightarrow F_{55} = 2 \times \left\{ 1 - \frac{2}{\pi} - \frac{4}{\pi R} \left[1 - (R + 1)^{\frac{1}{2}} + \frac{R}{2} \cos^{-1} \left(\frac{R}{R+2} \right) \right] \right\}$ $\rightarrow R = 4/8 = 0.5$ <p>Where R is the ratio of the radius of the curve divided by the distance between the two cylindrical surfaces.</p> <p>$\therefore F_{55} = 0.128$ and $F_{44} = F_{66} = 0$</p> <p>Using reciprocity and summation relations, six equations are generated to be solved for the other six unknowns:</p> $\therefore F_{45} = 0.185, F_{46} = 0.815, F_{54} = 0.118, F_{56} = 0.754, F_{64} = 0.408, F_{65} = 0.592$ <p>Which can be inferred that 81.5% of the radiation crossing the virtual surface 4 will hit the regenerator surface and 75.4% of the radiation leaving the top semicircular surfaces will hit the generator surface.</p>

4.3.1.1 The Radiation Resistance Network

By neglecting the radiation between surface 1 and 5, the radiation resistance network can be drawn as shown in Figure 4.7. The surface resistance of any surface is given by $R_i = (1 - \epsilon_i) / (A_i \epsilon_i)$ and the space resistance between any two surfaces is given by $R_{ij} = 1 / (A_i F_{ij})$, for weathered stainless steel emissivity ϵ can be taken as 0.78. The list of the view factors, the surfaces resistances and the space resistances are shown in Table 4.2.

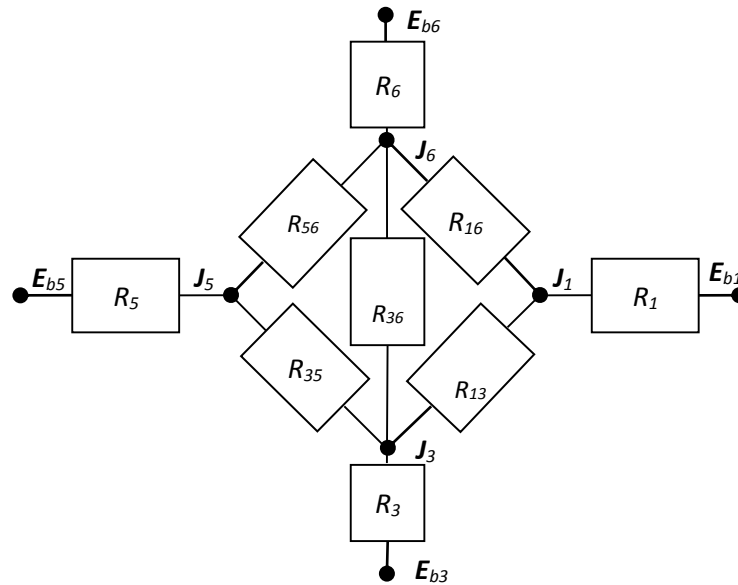


Figure 4.7: Radiation thermal resistance network for the convolution.

Table 4.2: Summary of radiation parameters of the convolution sections: (a) view factors, (b) space resistance and (c) surface resistance.

View factors	-	Space Resistance	K/W	Surface Resistance	K/W
F_{13}	0.576	R_{13}	691	R_1	70.3
F_{16}	0.0493	R_{16}	8075	R_3	13.8
F_{36}	0.0815	R_{36}	959	R_5	70.3
F_{53}	0.107	R_{53}	3720	R_6	34.7
F_{56}	0.754	R_{56}	528		

(a)

(b)

(c)

4.3.1.2 The Radiation Analysis for the Bulge

The bulge analysis is less complicated because it consists of only two surfaces. Figure 4.8 shows the schematic diagram of the bulge RHX. Similar to the previous case used between the bottom cylindrical surface of the convolution and the virtual surface, $F_{12} = 0.637$ or 63.7% of the generated radiation from the bulge is hitting the regenerator. The corresponding radiation resistance

network is shown in Figure 4.9. The results of the surface and the space resistance of the bulge and the regenerator are depicted in Table 4.3.

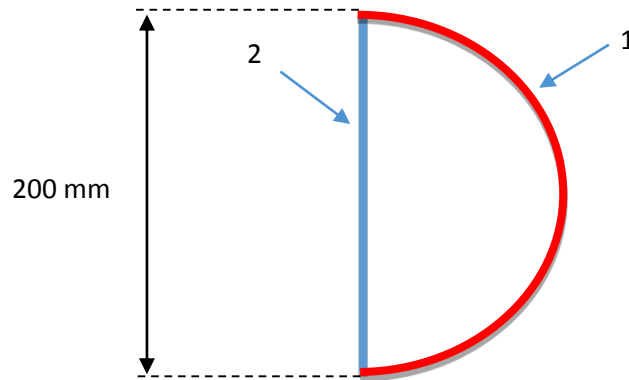


Figure 4.8: Radiation heat transfer between the bulge (1) and the regenerator (2).

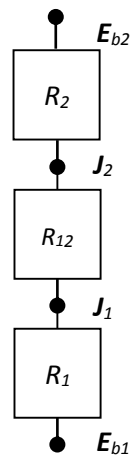


Figure 4.9: Radiation thermal resistance network between the bulge and the regenerator.

Table 4.3: Surface and space resistance between the bulge and the regenerator.

Thermal resistance	K/W
R_1	4
R_2	7
R_{12}	25
R_{total}	37

4.4 Numerical Modelling of Heat Transfer in the SCORE™ Thermoacoustic Engine

There are four different cases, each represents a different geometry in terms of variation of mesh and size. First and foremost, a three-dimensional bulge simulation model is proposed and created in GAMBIT software as shown in Figure 4.10. The bulge model is further examined by developing three additional geometries which have different RHX designs including the convolution model. The geometries of the first bulge model and the convolution model are the same as the aforementioned bulge and convolution design. The rest of the models of the bulge are designed based on the first bulge design but segmented into a smaller semi circles. The simulated space consists of mainly two regions; one is the porous zone (regenerator) and the other is the RHX region.

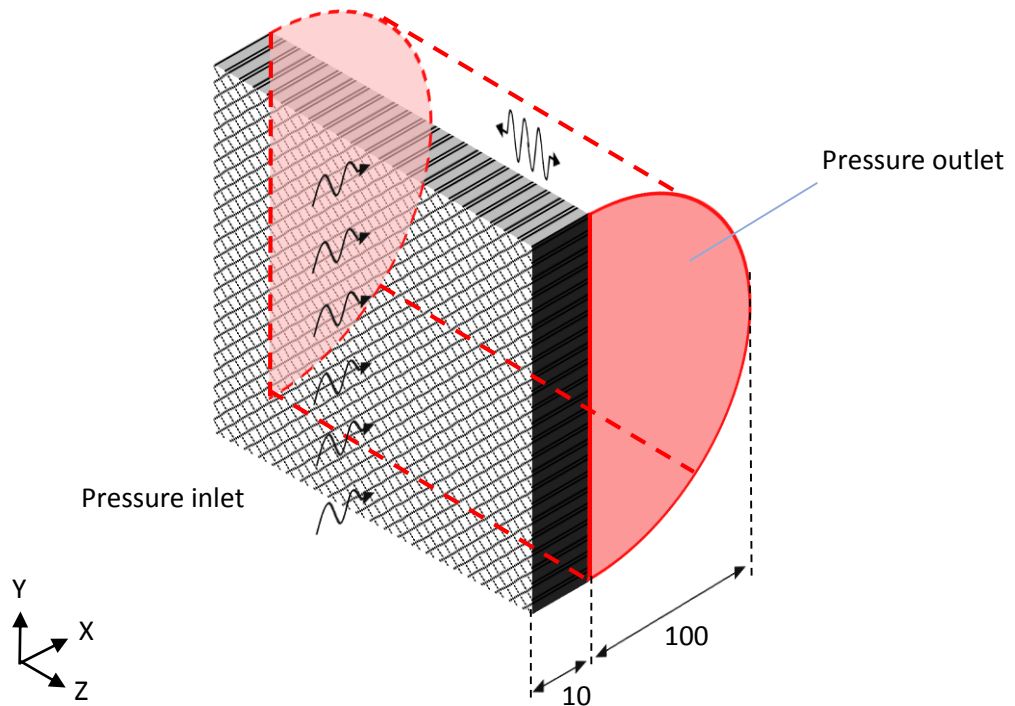
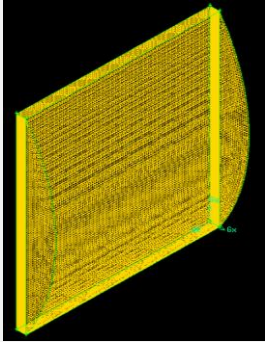
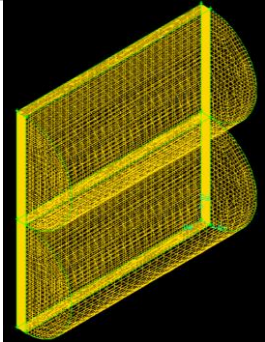
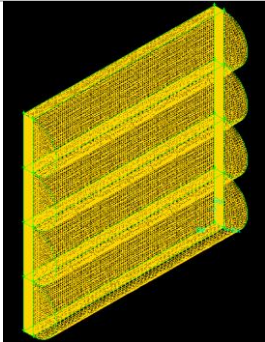
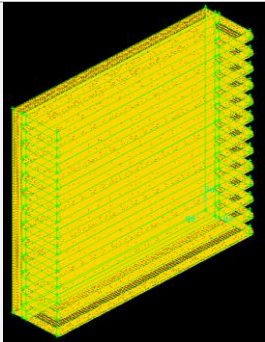


Figure 4.10: Three-dimensional representation of the bulge together with its dimension (in mm).

All the bulge dimensions are constructed in such a way that all the simulation models possess the same bulge surface areas of 0.0628 m^2 except bulge model A which has the same total bulge volume with the convolution model as shown in Table 4.4. The porous region dimensions for all the geometries are the same; each of 200 mm length, 200 mm width and 10 mm thickness. The two surfaces on the z-direction were assumed to be adiabatic wall on one side and an opening on the opposite one. The mesh generated for the geometries are to precisely determine the heat flow of the simulation models. In order to accurately simulate the models, hexahedral mesh was used to mesh the volume of all the four geometries. Meanwhile at the wall, it is made up of quadrilateral meshes which are expected to give better results over a mesh with full triangular grids. Uniform mesh or constant mesh spacing is generated for the geometries. These apply to both the porous and bulge regions. The mesh sizes were chosen based on the complexity of the geometries. Four different mesh sizes ranging from 46 to 500 thousands of cells were considered to perform mesh sensitivity study on bulge model B. Table 4.4 shows the mesh size for each of the cases.

Table 4.4: Mesh size, overall RHX surface area and total RHX volume excluding the porous media (regenerator) for all the four geometries.

Type of geometry	Mesh size (thousands of cells)	Overall RHX surface area (m ²)	Total RHX volume (m ³)
 Bulge A	101	0.0424	0.00123
 Bulge B	46	0.0628	0.00557
	100		
	250		
	500		
 Bulge C	181	0.001184	
 Convolution	566	0.231	0.00123

The models are then imported to Fluent Software 6.3 [103], a computational fluid dynamics (CFD) simulation environment. In order to supply a periodic flow for the model, a user defined function (UDF) is developed in C programming language. A harmonic pressure wave equation presented is used as an inlet pressure with the aid of UDF in Fluent as expressed by Equation (4.1):

$$p = p_o + D\sin(\omega t) \quad (4.1)$$

The time average pressure, $p_o = 670$ Pa is taken as the operating pressure and the coefficient $D = 100$ Pa is the pressure amplitude based on the experimental data [106]. $\omega = 2\pi f$ is the angular velocity and $f = 80$ Hz is the operating frequency of the model. The temperature of the periodic inlet pressure is assumed to have a constant temperature of 674 K. On the other hand, at the bulge surface, the temperature is set to be 1024 K based on the SCORE™ experimental data [106]. Constant emissivity, ϵ of 0.78 and no-slip boundary condition are assigned to all the stainless steel walls.

The most widely used and validated model, standard $k-\epsilon$ model is selected as the turbulence model to account for the fluid flow in both the porous media and the RHX regions. Thermal effects are also taken into consideration to enhance the heat transfer calculations near the walls. The Reynolds-Averaged Navier Stokes (RANS) equations are used in this work; Fluent solves numerically the usual Continuity, Momentum and Energy equations [107, 108]. Fluent solver uses a finite-volume procedure, which converts the different governing equation into algebraic form, together with the SIMPLE (Semi-Implicit-Method for Pressure Linked Equations) algorithm to solve these quantities numerically. For the discretization of the equations the second-order upwind scheme is selected for all the turbulent flow simulations carried out. A list of settings for the CFD model is presented in table 4.5.

Table 4.5: Fluent settings for all the four geometries.

Solver			Unsteady
Viscous model			$k-\epsilon$
Gravity			-ve 9.81 ms^{-2} in the Y direction
Material	Fluid		Ideal Gas approximation
	Solid		Stainless steel $\rho = 7800 \text{ kgm}^{-3}$, $c_p = 510 \text{ Jkg}^{-1}\text{K}^{-1}$, $k = 21.4 \text{ Wm}^{-1}\text{K}^{-1}$
Boundary condition	Pressure inlet		UDF $T = 674 \text{ K}$
	Bulge wall	0.001 m wall thickness	$T = 1024 \text{ K}$, $\epsilon = 0.78$
	Adiabatic wall		$\epsilon = 0.78$ (do not participate in S2S Radiation)
Discretization schemes			Pressure
			2 nd Order Upwind
			Density
			2 nd Order Upwind
			Momentum
			2 nd Order Upwind
			Turbulent Kinetic Energy
			2 nd Order Upwind
			Turbulent Dissipation Rate
			2 nd Order Upwind
			Energy
			2 nd Order Upwind
			Pressure-Velocity Coupling
			SIMPLE

Surface-to-surface (S2S) model is chosen to model the radiative heat transfer in this study. This model presents a method to obtain the intensity field of radiation exchange in an enclosure of gray-diffuse surfaces. The energy exchange between two surfaces depends on their size, separation distance, and orientation. These parameters are accounted for by the view factors [109, 110]. The main assumption of S2S model is that the exchange of radiative energy between surfaces is unaffected by the medium that separates them. Any absorption, emission or scattering of radiation can be ignored so only “surface-to-surface” radiation needs to be considered for analysis. The S2S model assumes that all surfaces are gray and diffuse. Thus according to the gray body model, if certain amount of radiant energy (E) is incident on a surface,

then a fraction (ρE) is reflected, a fraction (αE) is absorbed, and a fraction (τE) is transmitted. This radiation model also assumes that the heat transfer surfaces are opaque to thermal radiation. The transmissivity, therefore can be neglected. It follows, from the conservation of energy that the emissivity (ϵ) = absorptivity (α) and that reflectivity (ρ) = 1 - emissivity (ϵ). The energy flux leaving a given surface is composed of emitted and reflected energy. The reflected energy flux is dependent on the incident energy flux from the surroundings, which then can be expressed in terms of the energy flux leaving all other surfaces. Fluent uses the Equation (4.2) for the energy reflected from surface k [109, 110]:

$$\dot{q}_{out,k} = \epsilon_k \sigma T_k^4 + \rho_k \dot{q}_{in,k} \quad (4.2)$$

Where $\dot{q}_{out,k}$ is the energy flux leaving the surface, ϵ_k is the emissivity, σ is the Boltzman's constant and $\dot{q}_{in,k}$ is the energy flux incident on the surface from the surroundings.

The amount of incident energy upon a surface from another surface is a direct function of the S2S view factor, F_{jk} . The view factor, F_{jk} is the fraction of energy leaving surface k that is incident on surface j . The incident energy flux $\dot{q}_{in,k}$ can be expressed in terms of the energy flux leaving all other surfaces as Equation (4.3) [103]:

$$A_k \dot{q}_{in,k} = \sum_{j=1}^N A_j \dot{q}_{out,j} F_{jk} \quad (4.3)$$

Where A_k is the area of surface k and F_{jk} is the view factor between surface k and j (N is the number of surfaces). On another form of the aforementioned equation, Fluent utilises the radiosity J equation. The total energy given off a surface k is given by Equation (4.4) [103]:

$$J_k = E_k + \rho_k \sum_{j=1}^N F_{kj} J_j \quad (4.4)$$

Where E_k represents the emissive power of surface k .

4.4.1 Modelling of the Regenerator

According to the SCORETM experimental data [106], the regenerator comprises of 56 layers of stainless steel wire mesh which has a total thickness size of 10 mm. The material properties used for the porous zone is the same as the walls. A volumetric porosity, ϕ is 0.792 based on the SCORETM experimental data. The current study uses superficial velocity inside the porous media, based on volumetric flow rate, to ensure continuity of the velocity vectors across the porous media interface. Laminar zone option is disabled so that turbulence effect in porous media will also be taken under consideration. The effect of the porous media on the turbulence field is only approximated. In essence, the porous media is nothing more than an added momentum sink in the governing momentum equations. The porous media is modelled using additional momentum source term to the standard fluid flow equations. The source term composes of two parts; a viscous loss term and an inertia loss term as expressed in Equation (4.5) [111]:

$$S_i = - \left(\sum_{j=1}^3 D_{ij} \mu v_j + \sum_{j=1}^3 C_{ij} \frac{1}{2} \rho |v| v_j \right) \quad (4.5)$$

Where S_i is the source term for i th (x , y or z) momentum equation, v_j is the velocity component in j th (x , y or z) direction, $|v|$ is the velocity magnitude and μ is the fluid viscosity. The first term on the right hand side of Equation (4.5) is the viscous pressure loss term (Darcy term) due to the porous media structure whereas the second term (Forchheimer term) represents the pressure loss due to the momentum of the flow in the porous media zone. The parameter tensor

D_{ij} is called viscous resistance factor and C_{ij} is called inertial resistance factor, are defined by the user. Both constants have to be determined empirically. The inertial factor provides a correction for inertial losses in the porous medium at high flow velocity. This equation contributes to the pressure gradient in the porous cell, creating a pressure drop that is in proportion to the flow velocity (or velocity squared) [112]. The inertial and viscous resistance factors used in this work are derived based on the SCORE™ experimental results [106] as tabulated in Table 4.6:

Table 4.6: SCORE™ experimental data [7].

Data no.	Zone	Average gas particle displacement / mm	Velocity / ms^{-1}	Pressure / Pa	Pressure drop / Pa
1	Porous	2	1.01	447.2	2.36
	Bulge	8	4.02	444.8	-
2	Porous	3	1.52	670.8	4
	Bulge	12	6.03	667.2	-
3	Porous	4	2.02	894.4	4.72
	Bulge	16	8.04	889.6	-
4	Porous	7.1	3.57	1578.3	243.8
	Bulge	24	12.06	1334.5	-
5	Porous	14.2	7.12	3156.6	487.7
	Bulge	48	24.12	2668.9	-

The dependence between the pressure drop, Δp and velocity, v in the porous zone is approximated by means of a second-order polynomial function with the aid of MS Excel as shown in Figure 4.11.

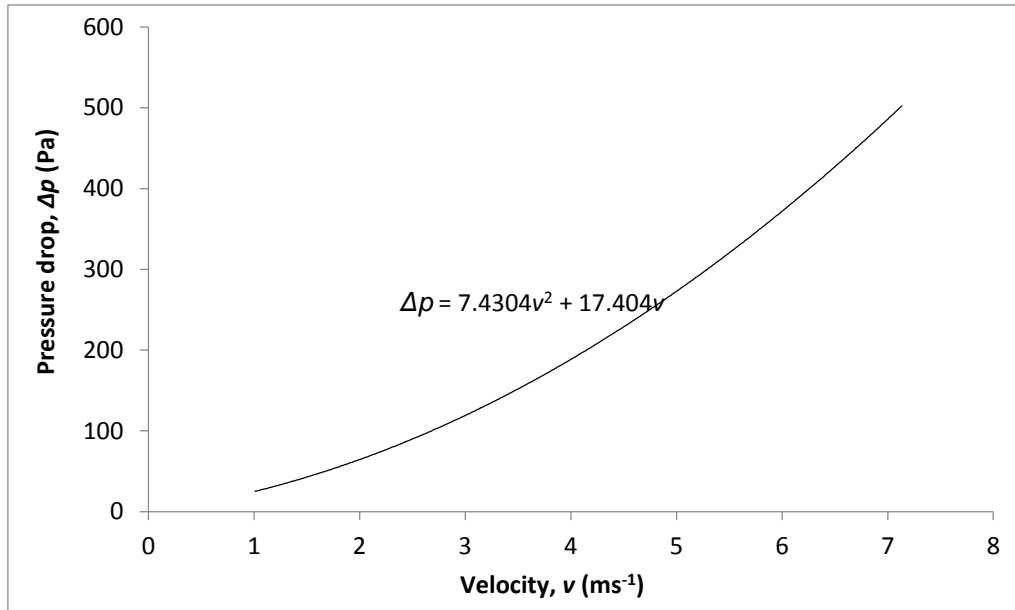


Figure 4.11: Pressure drop versus velocity along the regenerator.

The following Equation (4.6) is found from the graph:

$$\Delta p = 7.43v^2 + 17.4v \quad (4.6)$$

The air velocity can be defined as Equation (4.7):

$$v = \frac{\dot{m}}{A\rho} \quad (4.7)$$

Where \dot{m} is the mass flow rate of air, A is the cross-sectional area of porous region and ρ is the air density. Equation (4.13) implies that the unit of the constants are $\frac{kg}{m^3}$ and $\frac{kg}{m^2s}$ thus the Equation (4.6) can be written as Equation (4.8):

$$\Delta p = 7.43 \frac{kg}{m^3} v^2 + 17.4 \frac{kg}{m^2s} v \quad (4.8)$$

The simplified version of momentum equation for the homogenous porous media can be written as Equation (4.9) [112]:

$$\nabla p = S_i \quad (4.9)$$

Or for a particular direction as Equation (4.10) [112]:

$$\Delta p = -S_i \Delta n \quad (4.10)$$

Where S_i is the source term for the momentum equation in the i direction and Δn is the porous media thickness. In the case of simple homogenous porous media, the momentum source term S_i for the porous media is defined as Equation (4.11) [113]:

$$S_i = -\left(\frac{\mu}{\alpha} v_i + C_2 \frac{1}{2} \rho v_i^2\right) \quad (4.11)$$

Where α and C_2 are defined as the permeability and the inertial resistance factor of the porous medium respectively.

Thus:

$$\Delta p = \left(\frac{\mu}{\alpha} v_i + C_2 \frac{1}{2} \rho v_i^2\right) \Delta n \quad (4.12)$$

$$\Delta p = C_2 \frac{1}{2} \rho \Delta n v_i^2 + \frac{\mu}{\alpha} \Delta n v_i \quad (4.13)$$

The comparison of Equation (4.8) with (4.13) gives Equations (4.14) and (4.15):

$$\frac{\mu}{\alpha} \Delta n = 17.4 \frac{kg}{m^2 s} \quad (4.14)$$

$$C_2 \frac{1}{2} \rho \Delta n = 7.43 \frac{kg}{m^3} \quad (4.15)$$

Where μ denotes the dynamic viscosity. Therefore the viscous resistance factor (reciprocal of permeability) can be expressed by Equation (4.16):

$$\frac{1}{\alpha} = \frac{17.4 \frac{kg}{m^2s}}{0.01m \times 1.78 \times 10^{-5} \frac{kg}{ms}} = 97261652m^{-2} \quad (4.16)$$

The inertial resistance factor can be written as Equation (4.17):

$$C_2 = \frac{7.43 \frac{kg}{m^3}}{\rho \Delta n} = 2\chi \frac{7.43 \frac{kg}{m^3}}{1.225 \frac{kg}{m^3} 0.01m} = 1213m^{-1} \quad (4.17)$$

For all cases considered in these simulations the convergence criterion or normalised residual for the governing equations is set to be 1×10^{-6} . Transient simulations have a fixed time step size of 0.03142 seconds so that 20 time steps will complete a full period of oscillation in the inlet pressure. The maximum iterations per time step is set to be 20 which is sufficient to yield accurate results.

4.5 Results and Discussions

The radiation heat transfer between the convolution and the regenerator was first calculated based on simplified solution. The rate of radiation heat transfer is calculated by Equations (4.18) and (4.19):

$$\dot{Q}_{ij} = \frac{E_{bi} - E_{bj}}{R_{total}} \quad (4.18)$$

$$E_{bi} = \sigma T_i^4 \quad (4.19)$$

Where σ is the Stefan-Boltzman constant and T_i is the temperature of surface i . The convolution is divided into three sections and the radiation heat transfer

between each section and the regenerator is evaluated to compare the contribution of each section in the heat transfer between the two surfaces. It is important to mention that the entire surface of each of the bulge and the convolution are considered as isothermal because the wall thickness is very small. According to Figure 4.12, it can be seen that the top side of the convolution (section 5) is contributing more than the other two sections, the contribution of this section is about double the contribution of the other two sections on radiation heat transfer to the regenerator. Although the second section is bigger in area (section 3) but its contribution in heat radiation to the regenerator is found to be very limited due to the fact that this section is very narrow resulting in low view factor and hence high space resistance. It can be deduced that the current design of the convolution promotes convection rather than radiation which can be harmful and affect the performance of the engine.

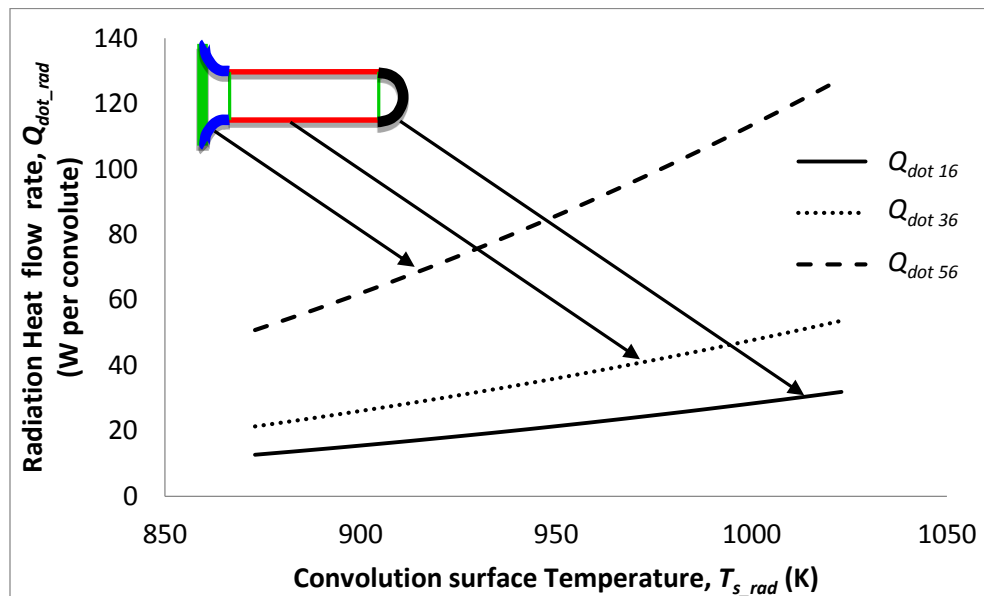


Figure 4.12: Heat flow from different sections of the convolution to the regenerator.

The comparison of the radiation heat transfer from the RHX to the regenerator surface indicates that the bulge is radiating more heat at the same temperature. The amount of heat radiated from the bulge is found to be around three times higher than the total radiation heat transfer from the convolution to the regenerator at the same temperature conditions. Figure 4.13 shows the radiation heat transfer from the convolution and from the bulge to the regenerator. The bulge has a deeper volume resulting in bigger distance between the hot surface of the bulge and the regenerator, this feature results in reducing the effect of having the hot surface of the bulge inside the engine as the air is oscillating away from this surface in comparison to the convolution in which the air is oscillating inside the convolution as it is representing part of the HHX.

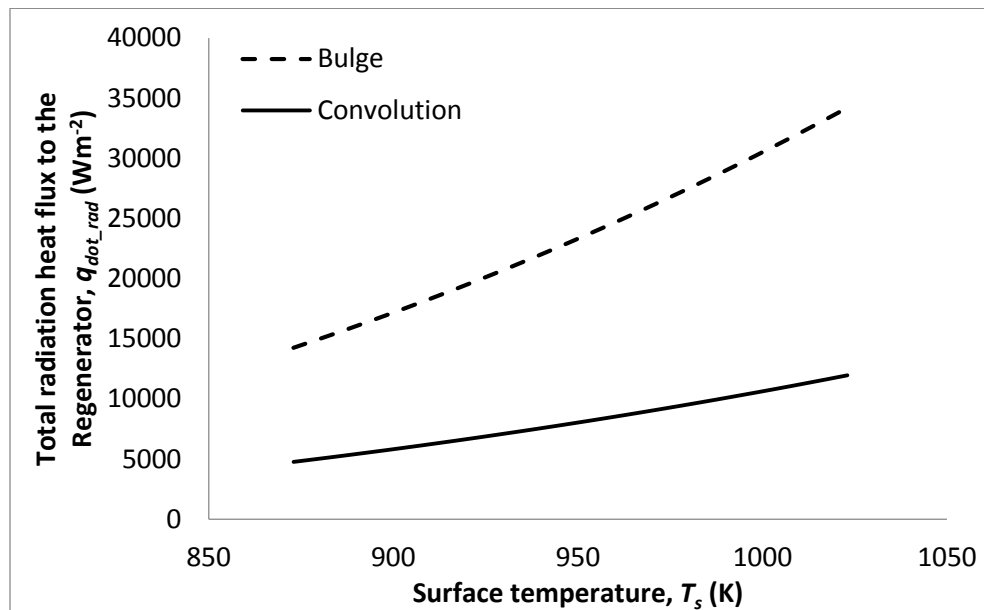


Figure 4.13: Radiation heat transfer from the convolution and from the bulge to the regenerator, with the comparison to the CFD simulation results.

Furthermore, the results of the numerical simulation are obtained based on the previous settings for the four stated conditions. Prior to the comparison of different CFD models, in order to study the influence of the mesh resolution on

the numerical results, a mesh sensitivity study was performed on the bulge B model to ensure that the solutions for all the models are independent of the mesh refinement. Accordingly to Figure 4.14, it can be seen that the different number of cells tested has insignificant effect on the heat flux predictions. Hence, it is unnecessary to increase the mesh density as it will generate almost the same results with longer computational time and slower convergence. There is only a slight difference between the results of radiation heat transfer from the 46k and 100k cells. This difference appears to be negligible in the cases of 250k cells and 500k cells. As a result, for less complicated geometries like bulge models A, B and C, the mesh independence can be achieved beyond 100k cells. On the other hand, due to the more complex design of the convolution model, a much finer mesh distribution was considered. The chosen mesh size for all the models were suitable and adequate to calculate accurately the heat flux in both regions.

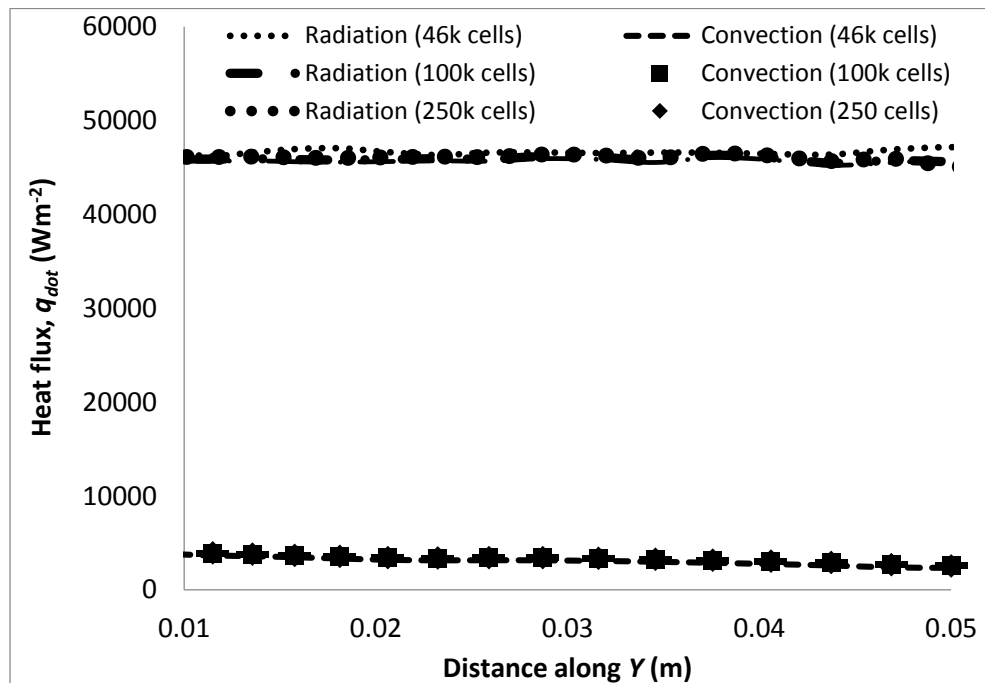


Figure 4.14: Convection heat flux and radiation heat flux for different mesh sizes for bulge B at $Z = 0.1$ m on the bulge surface at $t = 15.7$ s when the bulge surface temperature is 1024 K.

The convection and radiative heat fluxes from the surface of the bulge in the first three cases and for the convection are plotted and compared to each other. The cases of all the bulge models (bulge A, B and C) show a heat transfer by radiation in the range of 30000 Wm^{-2} to 48000 Wm^{-2} . As depicted in Figure 4.15, the convection heat flux prediction of the first three cases is very close with an average value of approximately 4000 Wm^{-2} . From the comparison of both modes of heat transfer, it is clear that that most of the heat is transferred by radiation in the first three cases.

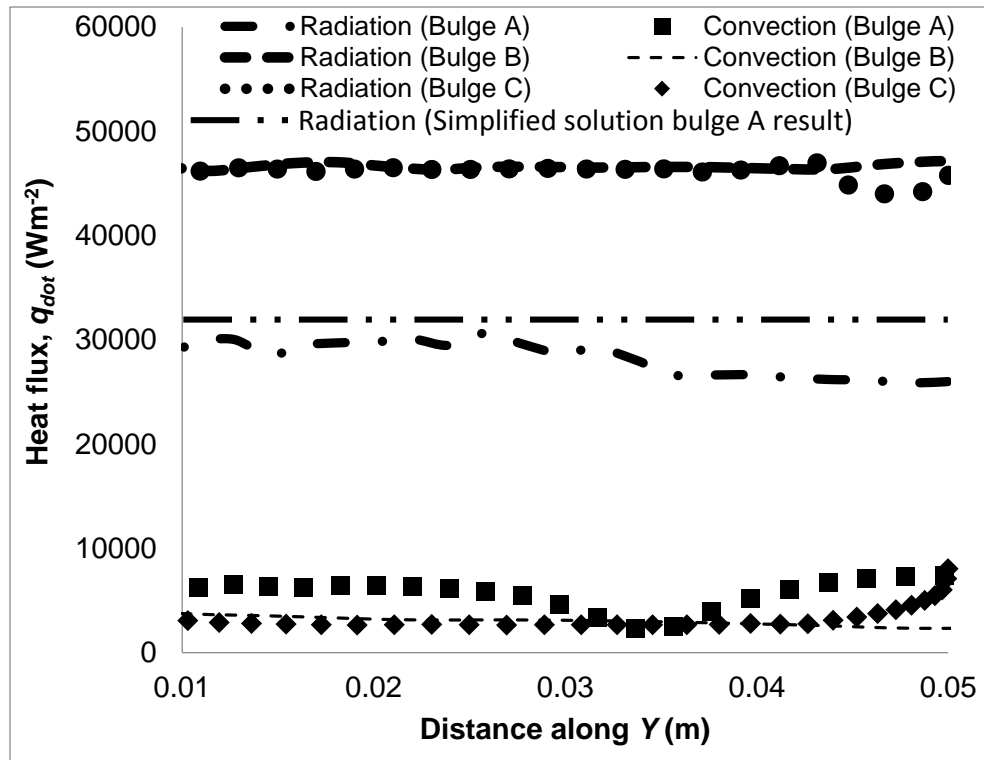


Figure 4.15: Convection heat flux and radiation heat flux for bulge A, B and C at $Z = 0.1 \text{ m}$ on the bulge surface at $t = 15.7 \text{ s}$ when the bulge surface temperature is 1024 K .

The study of two modes of heat transfer for the convection is also carried out as shown in Figure 4.16. It can be observed that the heat transfer by radiation is only a small fraction of the total heat flux. This indicates again that the current design of the convection promotes convection heat transfer over

radiation heat transfer. The convection case shows a very high convection heat flux especially beside the straight walls, this proves that the convection will have strong convection heat transfer to the air trapped within the convolutes. Figure 4.17 demonstrates the expected region which has greater radiative heat transfer in the convection. This makes physical sense because the majority of heat is reradiating to the convection's vertical walls.

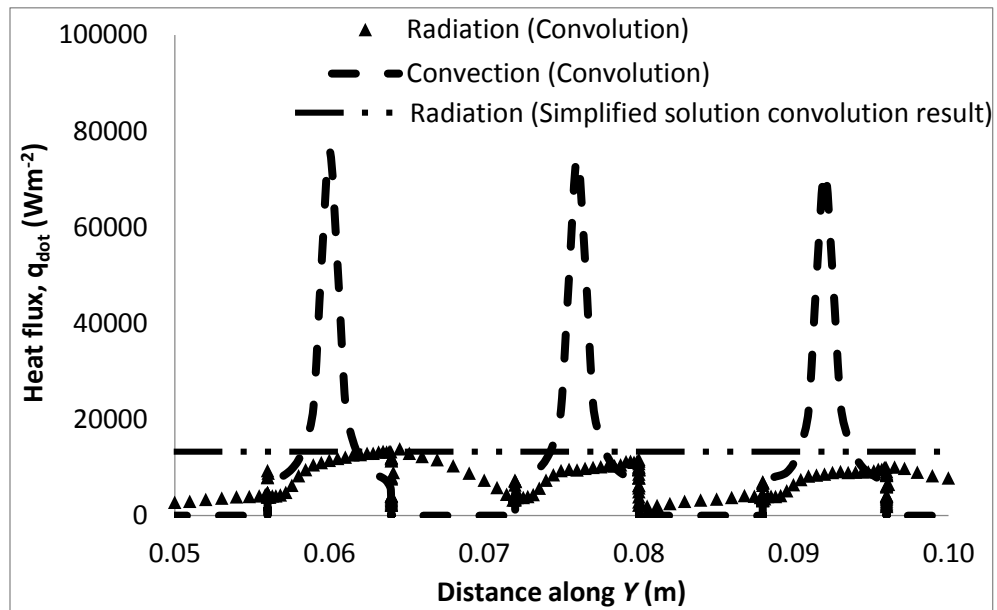


Figure 4.16: Convection heat flux and radiation heat flux for convection at $Z = 0.1$ m on the convection surface at $t = 15.7$ s when the convection surface temperature is 1024 K.

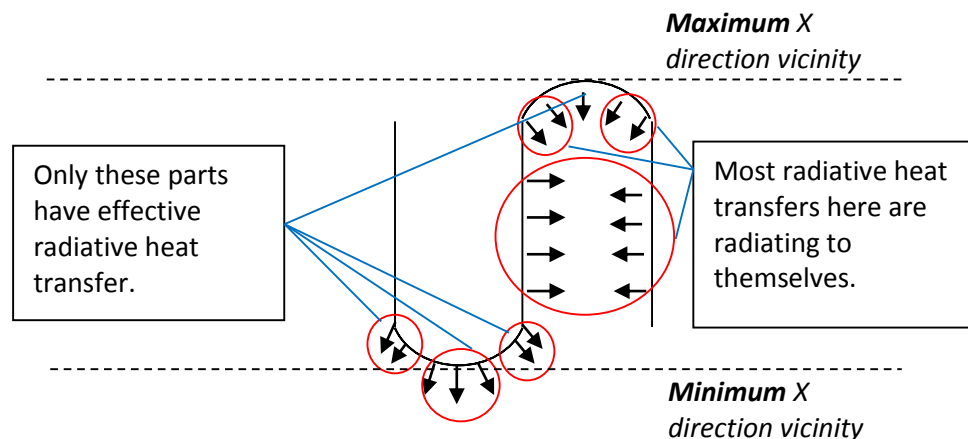


Figure 4.17: Cross-section of the convection model.

Moreover, the numerical simulation results are also compared against the results obtained by the simplified solution. It is found that the radiation heat transfer results obtained by the CFD simulation and the simplified solution have some discrepancies due to detailed shape of the RHX geometry is not taken into consideration in the simplified solution as shown in Figures 4.15 and 4.1.6. Nevertheless, both simplified solution and numerical results exhibit almost the same trend and reveal that bulge is about three times better in total radiation heat transfer compared to the convolution. Based on the numerical results obtained, the design of the bulge shows about five times more in total radiation versus convection to the regenerator top surface. The total amount of heat transferred from the convolution is found to be 2.5 times greater than bulge A and 1.8 times greater than bulge B and bulge C, but most of it is found to be by convection rather than radiation.

In addition, it can be found that the temperature of the air near the hot surface of the bulge is very high, but the temperature of the air away from the hot surface is relatively very low for all the bulge cases as illustrated in Figure 4.18, which depicts the preliminary temperature distribution of the geometries along the X direction when $t = 7.9$ seconds. The convolution has a visible hot spot in the entire convolution region, when the bulge models are compared to the convolution, it can be observed that the temperature of the air between the straight surfaces of the convolution is very hot, it is even hotter than the top surface of the regenerator. This behaviour may enhance convection versus radiation, which is not good for the performance of the engine. The temperature profiles are taken from YZ plane using area-weighted average method. A general trend can be seen, all the geometries show a gradual increase in temperature towards the bulge except the convolution which has an intense high temperature affecting big air volume away from the porous media.

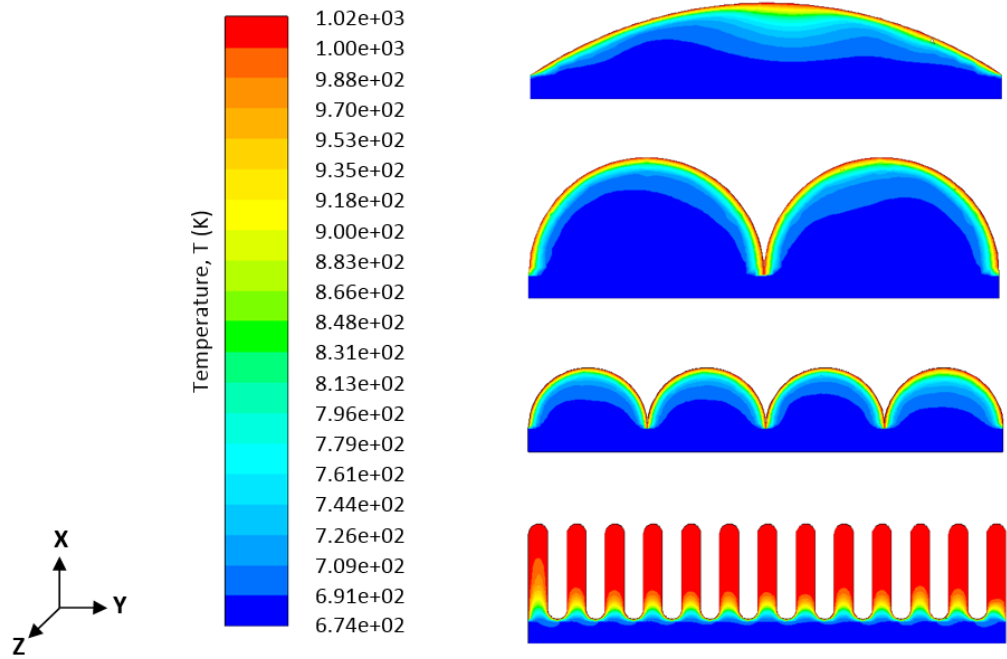


Figure 4.18: Contour of temperature distribution at XY plane when $Z = 0.1$ m for all the geometries at $t = 7.9$ seconds.

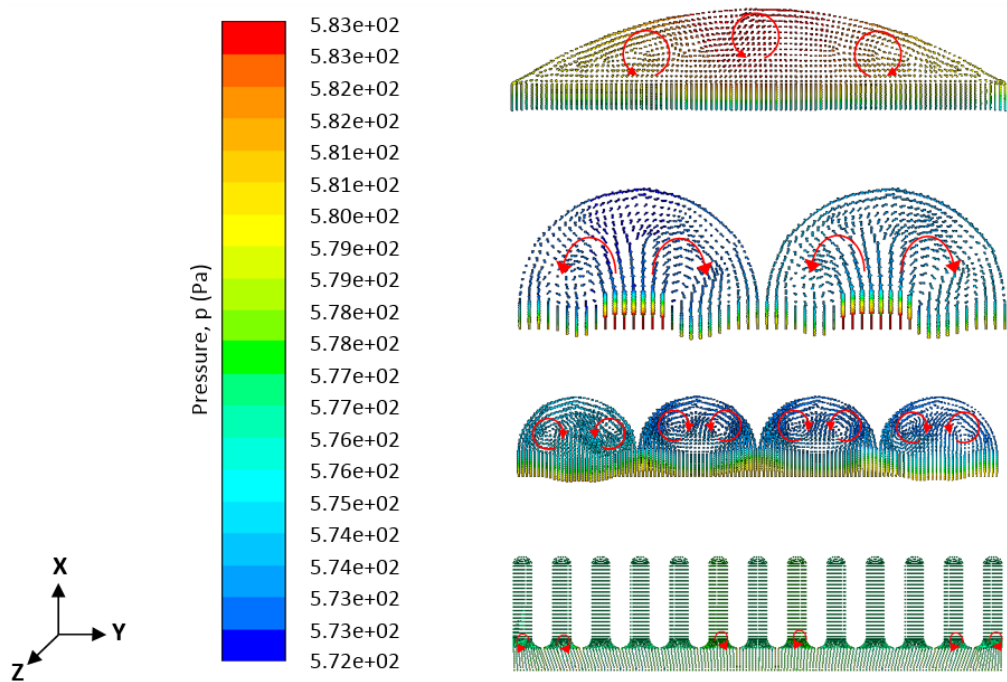


Figure 4.19: Contour of static pressure at XY plane when $Z = 0.1$ m for all the geometries at $t = 15.7$ seconds.

Convection need to be reduced or eliminated to enhance the performance of the TAE. This is because the heat leaking in the engine caused by convection leads to acoustic streaming. At the higher temperature region, the density of fluid is smaller and is replaced by the lower temperature fluid resulting in loss of acoustic energy. It can be noticed that, in the case of convolution RHX, there is a relatively huge amount of air volume at high temperature about 40% due to its proximity to the larger surface area of the convolution. As an extension to this investigation, an engine operating with a convolution RHX will be equipped with a bulge instead of the convolution to verify and validate the conclusions of this study in the following chapters. Figure 4.19 shows the contours of static pressure profiles. Four-concentric cylinder has obvious pressure flow circulations created at the bulge region. Only vague circulation patterns of pressure are seen from the convolution when $t = 15.7$ seconds.

4.6 Concluding Remarks

- A simplified solution is taken to study the radiation heat transfer between the regenerator and the RHX in two of the SCORE™ engine configurations.
- The feasibility of a new numerical approach has also been examined to study two modes of heat transfer, namely convection and radiation in the SCORE™ engine using CFD analysis.
- The radiation heat transfer results obtained by the CFD simulation and the simplified solution have some discrepancies due to detailed shape of the RHX geometry is not taken into consideration in the simplified solution.

- Both simplified solution and numerical results reveal that bulge is about three times better in total radiation heat transfer compared to the convolution.
- Convection need to be reduced or eliminated to improve the performance of the TAE.
- Based on the numerical results obtained, the design of the bulge show about five times more in total radiation versus convection to the regenerator top surface.
- The total amount of heat transferred from the convolution is found to be 2.5 times greater than bulge A and 1.8 times greater than bulge B and bulge C, but most of it is found to be by convection rather than radiation. It is also noticed that there is a relatively huge amount of air volume at high temperature about 40% due to its proximity to the larger surface area of the convolution.
- The CFD simulation carried out here have shown that some operating parameters including the temperature and the pressure as well as the geometry of the RHX can be of crucial importance in the heat transfer process between the hot surface subjected to the flames and the receiving top surface of the regenerator.
- To accurately predict the heat transfer in the model, conduction must also be included as well. Neglecting conduction heat transfer will result in underestimating the temperature and heat flux which will lead to the miscalculation of total heat flux and etcetera.

- It is important to mention the limitation of this study, as the convolution and the bulge are considered as isothermal surfaces because the wall thickness is very small.
- Part of this work was published in [114-117].

Chapter 5

Experimental Modelling of a Travelling-Wave Thermoacoustic Engine

5.0 Introduction

This chapter focuses on the experimental modelling of a TAE that works in travelling-wave mode by attenuating the sound wave using absorbing materials. The experimental setup is using a loudspeaker to generate an excitation signal at one end of a straight tube and an anechoic termination is placed at the other end by using different types of absorbing materials as described at the second section of this chapter. The third section presents the different types of excitation signals that are under examination. The multi-microphone least squares technique with the aid of impedance tube measurement method [43-45] used to determine the acoustic properties of the absorbing materials is also discussed. Then, the experimental results and discussions are presented. Concluding remarks are given in the final section. The comparison of the experimental results against the results produced by the numerical simulation using DeltaEC [46, 47] are discussed in chapter 7. The results of this

experimental work will be used to build the WHTAE model used to investigate the losses through the regenerator and the RHX in chapter 6.

5.1 Attenuation of Acoustic Waves

Instead of practically making the thermally induced acoustic waves of the investigated TAE to be travelling in a looped manner, the travelling-wave condition can alternatively be induced in other ways which were rarely reported in the past. Attenuation of acoustic waves was one of the important issues when creation of a travelling wave in an open loop is intended, this can be achieved through active or passive attenuation means. The travelling-wave condition can be created by making use of an anechoic termination in a system. In an active attenuation arrangement, the approximate travelling-wave condition can be developed by utilising a linear alternator to dissipate the acoustic energy as it propagates through a tube. Such a termination is done by tuning the termination impedance of a linear alternator to match with the impedance waveguide system in order to reduce reflections. It was found that this technique was not able to create a good travelling-wave phasing in the low frequency range, as the attenuation wave generated results in a very complicated wave condition inside the resonator [52]. Alternatively, passive attenuation is achieved by many different methods, such as by installing an extremely long straight tube filled with varying density of acoustic absorbing materials. This is not practicable because the footprint of the entire system will become very large. This study will develop an experimental modelling of a TAE that works in travelling-wave mode by using absorbing materials. When a speaker is used to emit the sound waves at one end of a straight tube, absorbing materials can be placed at the other extremity of the tube in order to experimentally obtain a travelling wave in an open loop, simulating the conditions of the engine while being able to control the frequency and

amplitude of the wave. The sound absorption coefficient is an important indicator which can effectively determine how much sound energy is dissipated and reflected back. This acoustic property can be determined if the sound reflection coefficient from a sample is known.

5.2 Experimental Setup

The experimental apparatus is composed of straight tubes and tapers which are made out of transparent acrylic plates. The total length of the system is 2.85 m and the wall thickness is 5 mm. The straight tubes have internal square cross-sectional area of 0.0081 m^2 and the tapers have internal rectangular cross-sectional area of 0.0122 m^2 respectively. Tapers are used at two ends of the tube to reduce energy losses and smoothen the acoustic flow. The working fluid is air at atmospheric pressure. One end of the tube is attached to a loudspeaker which acts as an acoustic excitation source while the tested sample is placed inside a wooden speaker box which is used as an absorbing termination at the other extremity. The loudspeaker generates an excitation signal which propagates down the tube and reflects from the other end of the tube whereas the tested sample in the wooden speaker box allows different termination impedance to be adjusted in order to match with the waveguide impedance to generate a travelling wave to propagate down the tube. The voltage supply to the loudspeaker is maintained at 2 V producing acoustic power of about 0.2-0.4 W for all the tested frequencies. Elastic gasket is used between the tubes and the tapers as well as the speaker boxes to provide sealing and avoid air leakage. Figure 5.1 shows the experimental setup of the impedance tube system when combinations of materials are under examination.

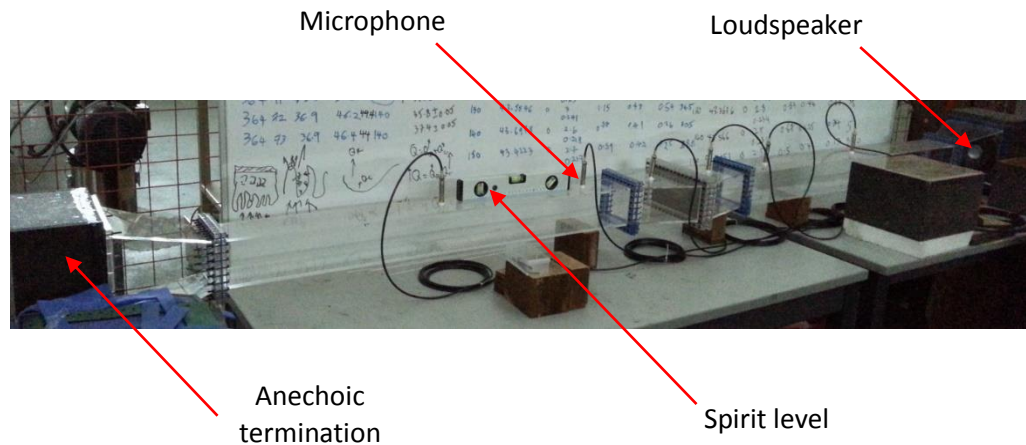


Figure 5.1: Experimental setup of multi-microphone impedance tube system.

A total of six microphones (PCB PIEZOTRONICS model 130E20) are used to measure the sound pressure along the length of the tube with the aid of a data acquisition system (DAQ). Holes are drilled on the top side of the straight tubes and tapers whereby the microphones can be slotted in and out easily to carry out the measurement. The microphones are sealed tightly to the mounting holes by using rubber and O-ring. All the microphones have different sensitivities and these microphones are calibrated with a GRAS Sound Calibrator Type 42AB for every experimental run before the experiment is conducted. The microphone signals are acquired using a National Instruments (NI) PXI-1031 chassis that consists of an 8 channel 24 bit NI PXI-6711 acquisition card and a NI PXIe-6672 module with a Window XP operating system. A Labview programme is specially written for data acquisition at a rate of 10 kHz. Using specifically written Matlab code, the data from each channel is converted to the frequency domain via a Fast Fourier Transform (FFT). A Hanning window with a 50% overlap is implemented in the averaging of data.

The measurements of acoustic properties are performed by varying the materials in the wooden speaker box. There are basically three different types of absorbing materials as shown in Figure 5.2: sponge, honeycomb filter and

egg tray. The experiment was also conducted on empty wooden speaker boxes which are believed to give a compliance volume. An 8 mm thick aluminium plate is also used as a rigid backing for verification purpose. All the materials are assumed to be isotropic which means that the physical properties will not vary with direction as only plane wave is taken into consideration.

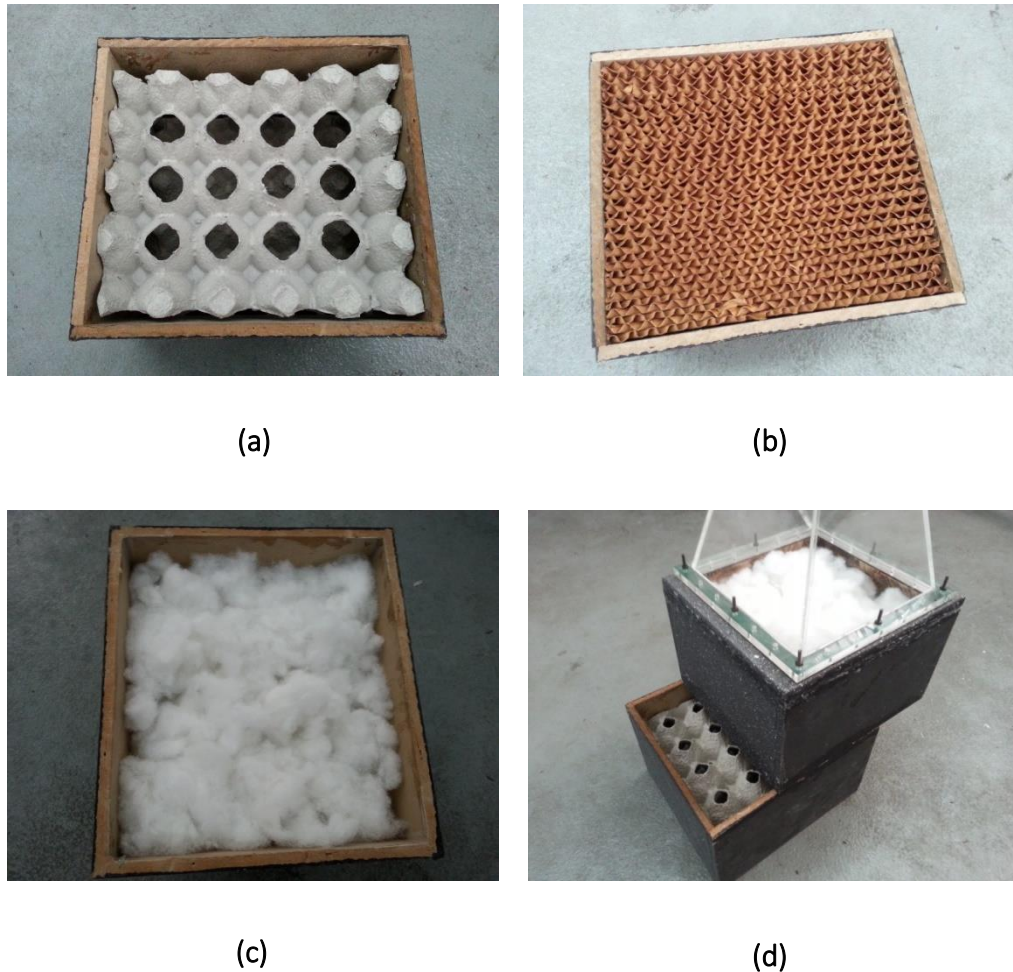


Figure 5.2: Four different types of materials that are under investigation: (a) Egg tray, (b) Honeycomb, (c) Sponge and (d) Egg tray and sponge combination.

5.3 Different types of Excitation Signals

It is extremely important to generate a suitable signal type that suits the application. At the beginning, the present study examined two different types

of excitation signals namely: Uniform white noise and Gaussian white noise. The measurements are done using a source of uniform white noise and repeated with a Gaussian white noise having a wide frequency band. The uniform white noise produces a uniformly distributed random signal with constant amplitude of unity, whereas the random signals produced by Gaussian white noise not systematically planned and the amplitude tends to vary with time because it relies on the mean and variance of the normally distributed signals. The selection of excitation signal is made based on the stability of the signal strength in the low frequency region. A comparison of different types of excitation signals and the results obtained by DeltaEC software are discussed in chapter 7.

5.4 Multi-Microphone Least Squares Technique

The formulation of this method was developed based upon an imaginary source equidistant from the specimen in an impedance tube but in the negative x-direction as depicted in Figure 5.3.

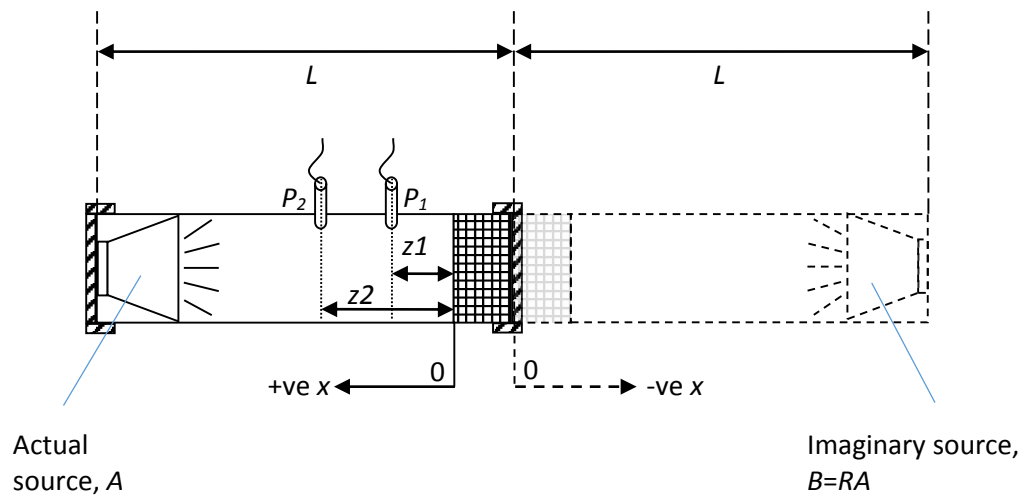


Figure 5.3: Impedance tube setup for two-microphone method.

The imaginary region is symmetrically mirrored at the end of the specimen from the actual source region. The amplitude of the imaginary source is given by Equation (5.1):

$$B = RA \quad (5.1)$$

Where R is the complex reflection factor and A represents the amplitude of the actual source in Equation (5.1). The relationship between the measured pressure from each microphone and both of the sources can be deduced with the aid of a Green's function as shown in Equations (5.2) and (5.3):

$$p_1 = Ag_{1A} + Bg_{1B} = A(g_{1A} + Rg_{1B}) \quad (5.2)$$

$$p_2 = Ag_{2A} + Bg_{2B} = A(g_{2A} + Rg_{2B}) \quad (5.3)$$

Where p_1 and p_2 are the pressures from the microphone 1 and 2 respectively. g_{1A} and g_{1B} are the Green's functions that relate the inputs to microphone 1 from the output of the actual source, A and the imaginary source, B respectively. Same relationship apply for Green functions, g_{2A} and g_{2B} with respect to microphone 2. Considering a plane wave is propagating in the tube, the Green functions can be expressed by Equations (5.4) to (5.7):

$$g_{1A} = \frac{\rho_0 c}{2s} e^{-ik(L-z_1)} \quad (5.4)$$

$$g_{1B} = \frac{\rho_0 c}{2s} e^{-ik(L+z_1)} \quad (5.5)$$

$$g_{2A} = \frac{\rho_0 c}{2s} e^{-ik(L-z_2)} \quad (5.6)$$

$$g_{2B} = \frac{\rho_0 c}{2s} e^{-ik(L+z_2)} \quad (5.7)$$

Where ρ_o is the air density, c is the speed of sound, s is the cross-sectional area of the tube, L is the total length of the system, z_1 and z_2 are the distances between the sample and the microphone 1 and 2 respectively. k represents the wave number which is defined as $2\pi f/c$. The transfer function, H_{12} is the pressure ratio between microphone 1 and 2 which can be rearranged to give the complex reflection coefficient, R as shown in Equations (5.8) and (5.9):

$$H_{12} = \frac{p_2}{p_1} = \frac{g_{2A} + g_{2B}R}{g_{1A} + g_{1B}R} \quad (5.8)$$

$$R = \frac{g_{2A} - g_{1A}H_{12}}{g_{1B}H_{12} - g_{2B}} \quad (5.9)$$

The absorption coefficient is an important indicator which can effectively determine the fraction of energy that is dissipated and reflected back. An absorption coefficient of unity means the reflection coefficient is zero. The theory above was initially applied to a two-microphone case. More microphones are needed in order to get a more accurate result. An optimised reflection coefficient, R_{opt} can be obtained by using a least squares solution with the aid of multi-microphone method. This optimized method will produce a single curve based on all the microphone combinations by taking the closest microphone to the sample as a reference.

$$R_{opt} = - \frac{\sum_{m=2}^M (g_{1A}H_{1m} - g_{mA})(g_{1B}H_{1m} - g_{mB})^*}{\sum_{m=2}^M |g_{1B}H_{1m} - g_{mB}|^2} \quad (5.10)$$

The purpose of this optimisation is to minimise the sum of errors between the measured and the analytically derived pressure. Equation (5.10) can be used for any number of microphone positions M , where m indicates number of each microphone in the tube. The absorption coefficient of the sample, α can be determined by Equation (5.11):

$$\alpha = 1 - |R_{opt}|^2 \quad (5.11)$$

5.5 Impedance Tube System

An impedance tube system is an acoustic measurement that provides an effective and easy way for measuring the acoustic properties of a specimen. This method has a frequency limitation as a consequence of the microphone positions. The working frequency range of interest is crucially important and is dictated by the shortest and farthest microphone separations. If the microphones are too close to each other, the pressure difference between them will be too small to be accurately measured and the errors will increase. The impedance tube system needs to be long enough, with the farthest microphone separation of approximately $1/20^{\text{th}}$ of the acoustic wavelength at the lowest required frequency of measurement. The low frequency limit is given by Equation (5.12):

$$f_l > \frac{0.05c}{|z_1 - z_2|} \quad (5.12)$$

This method is also sensitive to errors if the microphones are too far apart. As the distance between the microphones becomes equal to the acoustic wavelength the pressure at the two microphones will be the same at the corresponding frequency and the simultaneous equations will not be solvable. The upper frequency limit is given by Equation (5.13):

$$f_u < \frac{0.45c}{|z_1 - z_2|} \quad (5.13)$$

In addition, the microphone closest to loudspeaker should be at least two tube diameters away from the loudspeaker as by this distance any cross modes generated will have little effect, so that only plane waves will be measured by

the microphone. The closest microphone to sample should also be sufficiently far away from the sample. To ensure accurate measurements to be taken, at least a distance of half of the diameter of tube is needed in between them. The aforementioned multi-microphone least square technique is employed in conjunction with impedance tube measurement method to determine the acoustic properties of the tested specimen. The reason for using the multi-microphone least squares technique in this work is due to the fact that the additional microphones increase the working frequency range and it can also compute the transfer functions separately for each pair of microphone positions.

5.6 Results and Discussions

5.6.1 Absorption and Reflection Coefficients from an Approximate Rigid Surface

The multi-microphone least square technique is employed in conjunction with impedance tube measurement method to determine the acoustic properties of the tested specimen by using the aforementioned excitation signals. Generally the frequency is found to be the main parameter affecting the magnitude of reflection and absorption coefficients of the thick aluminium plate which is considered first to approximately represent a rigid end. In the range of the tested frequency, the types of input signal are found to be of small effect on the reflection and absorption coefficients. Both types of excitation signals decrease as the frequency increases until a minimum reflection coefficient of around 0.65 at 50 Hz, after 50 Hz a gradual increase of reflection coefficient is observed. Figure 5.4 presents the reflection coefficient of the rigid plate for different types of excitation signals from the source. The thick aluminium plate is found not to be a perfect rigid backing, but the reflection

coefficient is close to unity in the tested frequency range. The corresponding absorption coefficient results of the thick aluminium plate are also plotted against frequency as shown in Figure 5.5. Both excitation signals have almost the same trend showing an increase of absorption coefficient until a maximum value of around 0.55 at 50 Hz, after which a gradual decrease of absorption coefficient is noticed. Despite only a small difference between the two excitation signals, uniform white noise is chosen at the end to be the excitation signal for the rest of the experiments because of its intrinsic uniform spectral density distribution at all the frequencies.

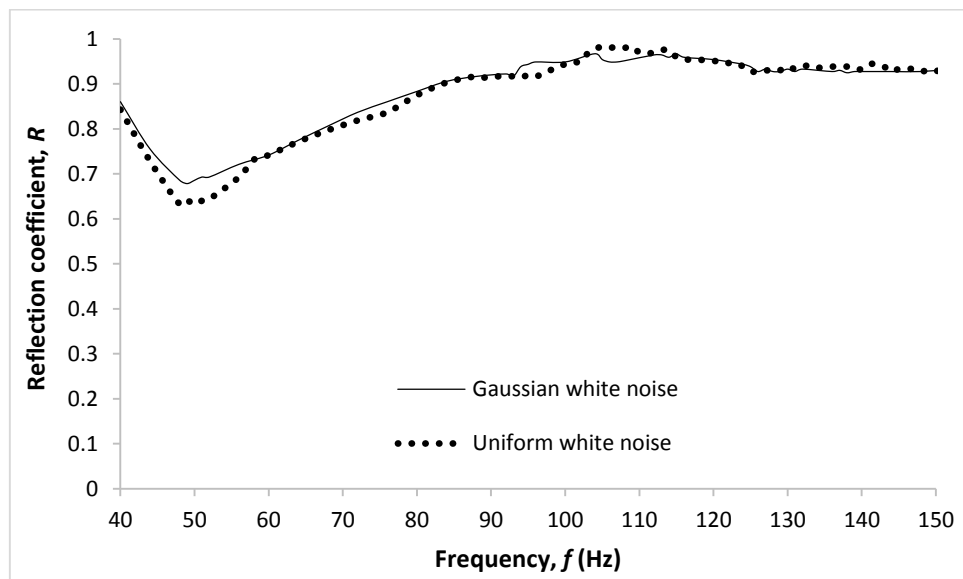


Figure 5.4: Reflection coefficient versus frequency when the thick aluminium plate is under examination.

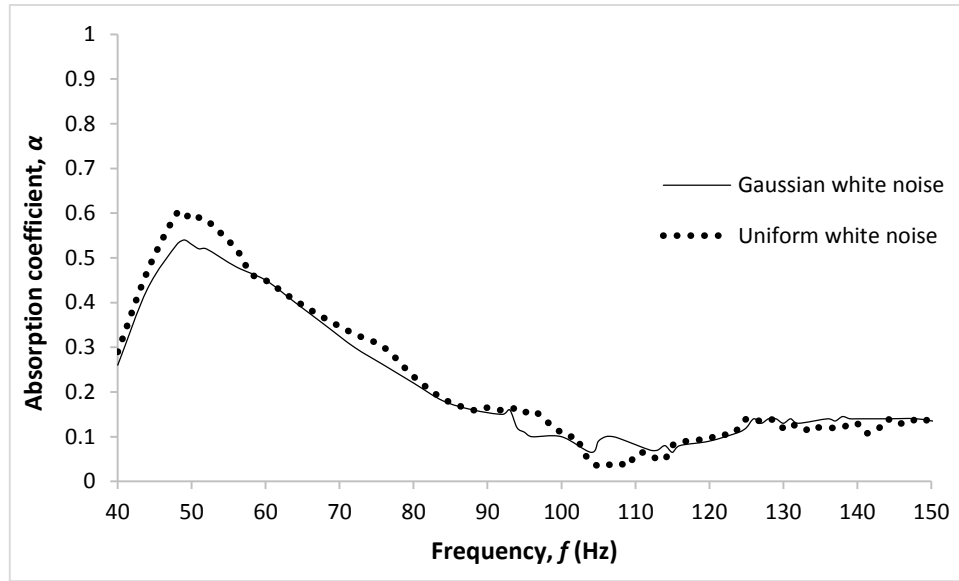


Figure 5.5: Absorption coefficient as a function of frequency when the thick aluminium plate is used as the rigid backing.

5.6.2 Performance of Potential Attenuation Alternatives

In order to find a potential attenuation arrangement suitable for the very low frequency range (below 150Hz), the performance of the different material combinations is under investigation. Therefore, eight different arrangements were investigated as well as the rigid aluminium plate which is taken as a reference. The absorption coefficient is found to change with the frequency for all types of attenuation arrangements. The elastic end shows the highest absorption coefficient relative to the other attenuation alternatives. The elastic end is essentially an acrylic plate with a thickness of 0.5 mm. Other attenuation arrangements work better at higher frequency range (few kHz) but for this very low frequency range, which is rarely investigated, the elastic end is found to be better as shown in Figure 5.6.

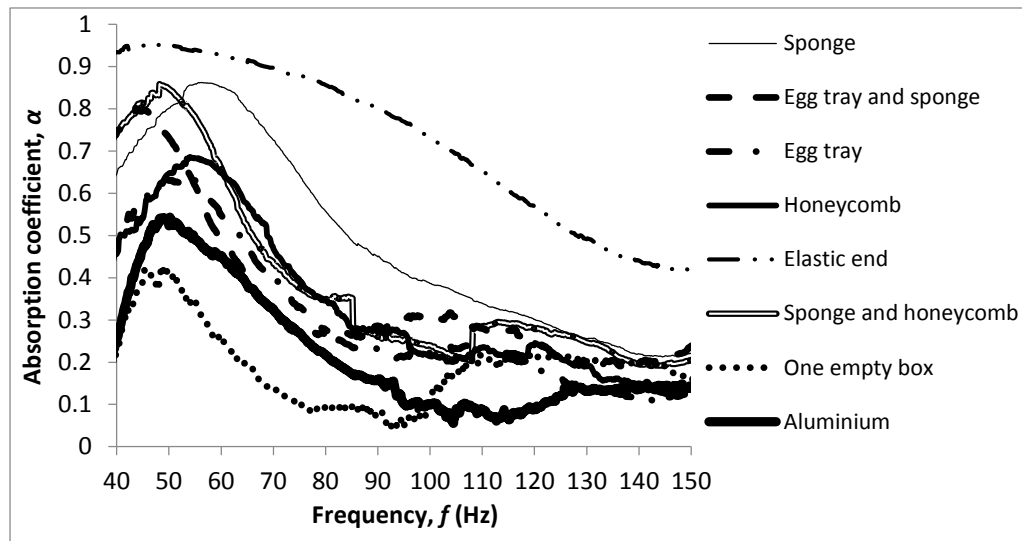


Figure 5.6: Absorption coefficient as a function of frequency for all the tested materials when uniform white noise is used as the excitation signal.

A general trend can be clearly observed that most of the tested materials exhibit a maximum absorption coefficient at the frequency of approximately 50 Hz which is the natural frequency of the system. At the resonant frequency, the system experiences a high acoustic impedance thus a higher absorption coefficient. The absorption coefficient is gradually decreased after the peak value with increasing frequency. A compliance volume (empty box) gives a rather low absorption coefficient as compared to the rigid end (thick aluminium plate) at the frequency below 100 Hz. Whereas the absorption coefficient obtained for the rest of the absorbing material arrangements are higher than the rigid plate regardless of the frequency, which gives confidence to the validity of the results. Noting that the thick aluminium plate is approximately a rigid end which should reflect back most of the incident acoustic waves. Besides that, the sponge is found to have lower absorption coefficient compared to the elastic end, but it has a better absorption coefficient compared to all other materials or combinations of materials used in the frequency range above 50 Hz. All combinations of two materials performed better in the frequency range below 55Hz. With the inclusion of the sponge, all materials investigated

exhibited a higher absorption coefficient when used in a combination of a pair of two materials together, compared with the case when each one is used separately. The sponge and honeycomb combination is found to have a better absorption coefficient than the combination of egg tray and sponge.

5.7 Concluding Remarks

- The selection of the attenuation material or combination of materials should be done very carefully and is strongly dependent on the target frequency.
- Eight materials and combinations are investigated to realise that using an elastic end works best for low frequency attenuation applications.
- No material can work better for all frequencies. Some of the materials are suitable for high frequency but not suitable for low frequency attenuation applications.
- The outcomes of this experimental work are used to build the WHTAE model used to investigate the losses through the regenerator and the RHX in chapter 6.
- Part of this work was published [118].

Chapter 6

Losses through the Regenerator and the Radiant Heat Exchanger

6.0 Introduction

In this chapter, details regarding the energy fluxes in both the regenerator and the resonator in association with RHXs of two different configurations are discussed. Analysis of the acoustic field is also implemented to further understand the energy losses in the thermoacoustic system. The experiments are conducted by setting up two different configurations namely: straight tube and RHX configurations. Owing to the complexity of the complete experimental setup, experiments were first carried out in an acrylic straight tube configuration to investigate the acoustic energy losses through the regenerator before proceeding to the more complicated setup that consists of RHX. At the beginning, an introduction of losses in the regenerator is presented. The experimental apparatus of straight tube configuration is then described. In addition, the instrumentation and experimental procedure for the straight tube configuration as well as the microphone technique employed to determine the acoustic energy dissipation in the engine are presented. It then goes on to discuss the formulations used to obtain the energy dissipation in the engine and some important parameters including Womersley number and

standing wave ratio (SWR). The experimental results and discussions of losses in the regenerator are then presented. The acoustic energy dissipation due to the U-shaped flow path and the performance of the two RHXs are examined by the RHX configuration in the second stage of the experiment. Moreover, the losses in the RHX is presented. It then goes on to detail the experimental setup of RHX configuration as well as the instrumentation and experimental procedure for RHX configuration. The experimental results and discussions of losses through the RHXs are then presented. The concluding remarks are given in the final section. The experimental results obtained are then used for validation against the DeltaEC simulation results as discussed in chapter 7.

6.1 Losses in the Regenerator

The regenerator is the heart of the thermoacoustic device. It is sandwiched between two heat exchangers, one to supply heat at high temperature, the other withdraw heat from the system at low temperature. The temperature gradient across this porous section results in amplification of pressure disturbances in the working gas. In order for amplification to occur, this temperature gradient has to be larger than the critical temperature gradient [32]. It is intuitive that the acoustic wave in the thermoacoustic device as it propagates through the regenerator will experience energy losses. The acoustic energy dissipation is mainly due to the interaction between the narrow flow channels and the oscillating working fluid. The acoustic energy transportation in the regenerator of a straight tube configuration is discussed in detailed in the following sections.

6.2 Experimental Setup of the Straight Tube Configuration

The experimental setup for the straight tube system is the same configuration as the aforementioned passive attenuation experiment in chapter 5. Nonetheless instead of having an empty cross section, a regenerator is installed in the system. Based on the previous results in chapter 5, the elastic end is selected as the anechoic termination throughout this experiment. Air is also used as the working gas in this experiment. Basically, the experiment is carried out in two conditions: ambient and hot conditions. In the ambient condition, the experiment is implemented in room temperature whereas in the hot condition, a heating element is used to provide heat energy in the system at one side of the regenerator. The electrical power is supplied to the heating element by an AC power supply with the aid of a heater controller to ease the control of temperature. Mica plates with a thickness of 10 mm is attached between the flanges to protect the acrylic tubes from melting and also served as a regenerator holder. The CHX is placed in contact at the other end of the regenerator, withdrawing heat from the system using chilled water of constant flow rate via a water jacket. To reduce the radiative heat fluxes produced by the HHX, aluminium foil sheets are attached on the acrylic walls at the test section. A small fan is used to cool down the external walls of the system near the test section. Figure 6.1 shows the experimental setup of the straight tube configuration. The details of the regenerator, hot and cold heat exchangers are discussed as below.

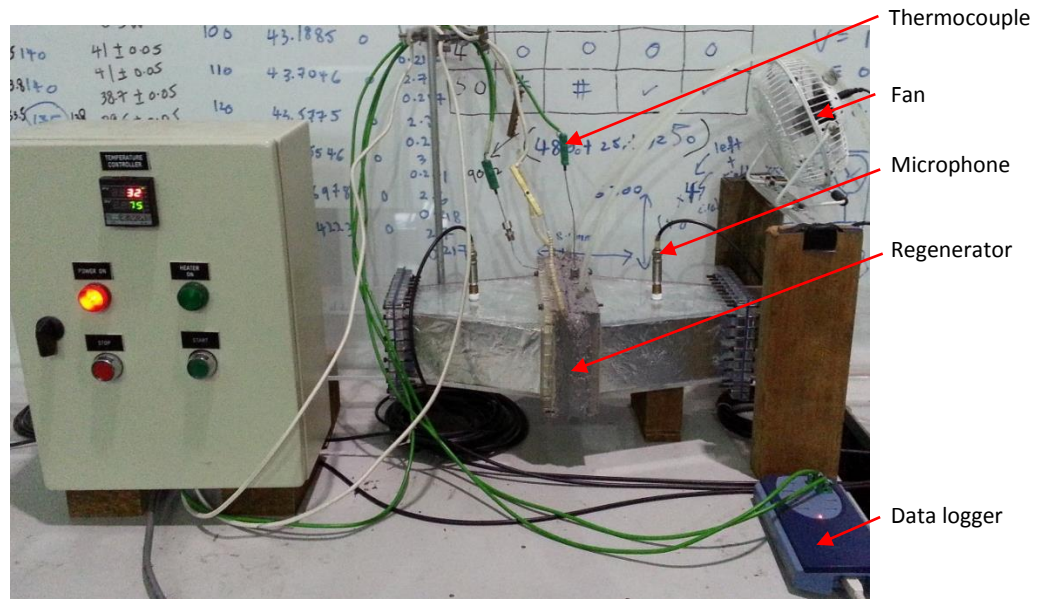


Figure 6.1: Layout of the test section for the straight tube configuration in hot condition.

6.2.1 Regenerator

The regenerator has a rectangular shape and is composed of layers of stainless steel wire meshes. Before inserting the meshes to the rig, the desired number of meshes are sewed together as one regenerator as depicted by the white circles in Figure 6.2. This is because the mesh is expandable when being compressed resulting on separation of the regenerator layers. The wire diameter of the regenerator is 0.12 mm and the corresponding porosity can be calculated based on Equation (1.9) as 0.792. The close-up view of the dimensions of the stainless steel wire mesh is produced using a magnification scale of 400% to the actual size as shown in Figure 6.3.

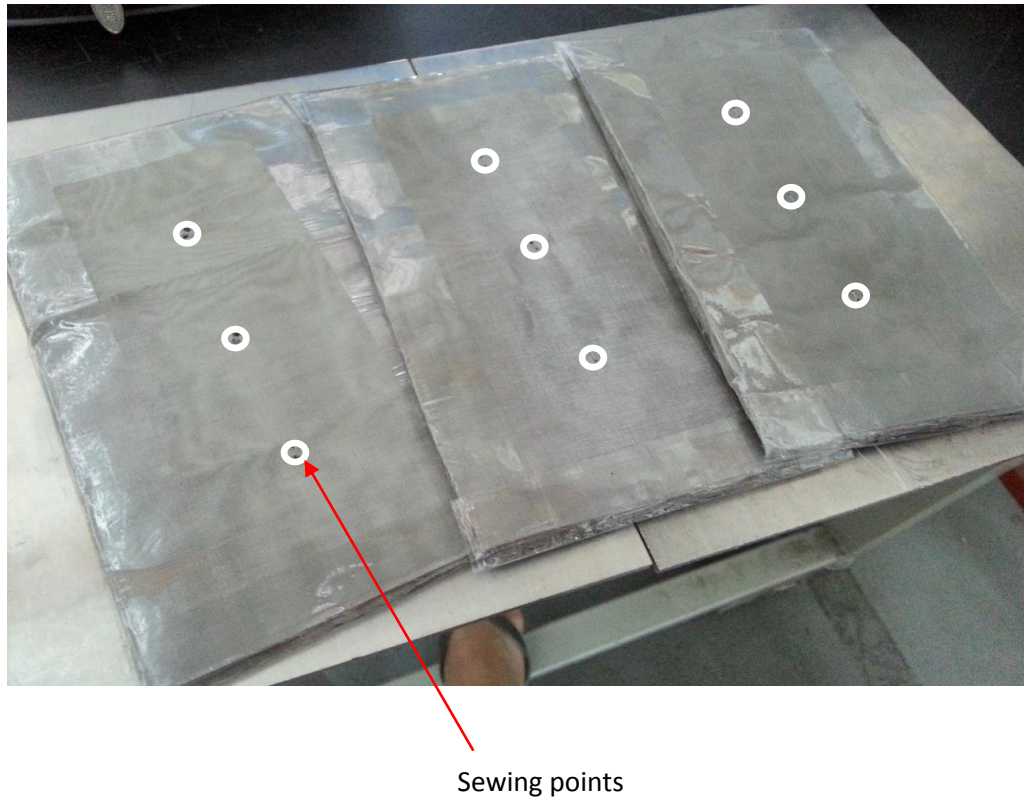


Figure 6.2: Stainless steel wire meshes that are stacked together using sewing.

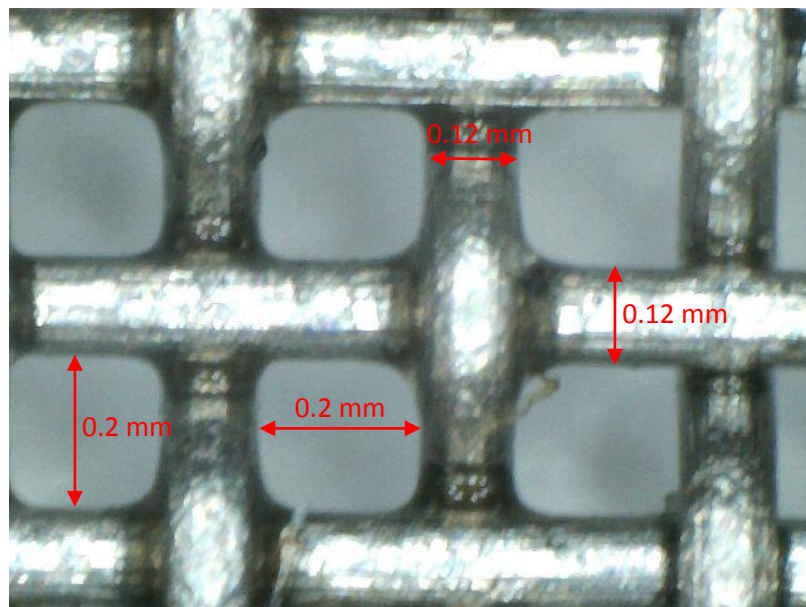


Figure 6.3: Close up (400% magnification) of the regenerator wires.

6.2.2 Hot Heat Exchanger

An electric heater is used to supply heat at one side of the regenerator. The heater is essentially a flexible heating wire insulated by ceramic material with a heating power of 1 kW. The heating element is mounted around the circumference of the first layer of the regenerator to provide uniform heat flux as well as to reduce the acoustic wave blockage. The working gas passes through the hot part of the regenerator and oscillates forming a part of the thermoacoustic system.

6.2.3 Cold Heat Exchanger

The CHX of the engine is a commercial motorcycle radiator with a geometry of louvered plate-fin type. It is made out of aluminium material which has a reasonably good thermal conductivity. The thickness of the fins is 0.16 mm and the corresponding void fraction can be obtained based on Equation (1.9) as 0.646. Figure 6.4 shows the heating element and the CHX used in the experiment.

(a)



(b)

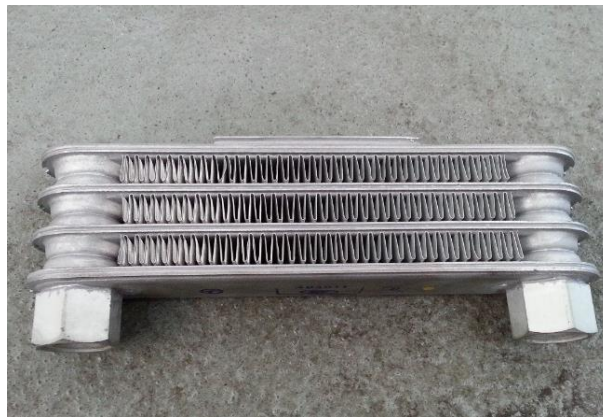


Figure 6.4: Heat exchangers of the system: (a) heating element and (b) cold heat exchanger.

6.3 Instrumentation and Experimental Procedure for Straight Tube Configuration

In the experiments, the main measuring quantities are the oscillating pressure and temperatures at selected locations along the system. The temperature measurements are performed in three different locations of the system by using Type-K thermocouples: inside the radiator, last layer of the regenerator and the top layer of the regenerator. Moreover, the acoustic pressure readings are measured using pressure transducers with the aid of the data acquisition system. A total of six microphones (PCB PIEZOTRONICS model 130E20) are installed in the system to monitor the distribution of sound pressures along the

length of the tube whereby three microphones are placed upstream of the tube and the other three are placed at the downstream. All the microphones have different sensitivity and these microphones are calibrated with a GRAS Sound Calibrator Type 42AB for every experimental run before the experiment is conducted. A Labview programme is specially written for data acquisition at a rate of 10 kHz. Using specifically written Matlab code, the data from each channel is converted to the frequency domain via a Fast Fourier Transform (FFT). A Hanning window with a 50% overlap is implemented in the averaging of data. In order to investigate some of the important frequencies of interest, a single frequency acoustic wave is generated by the loudspeaker with the aid of a signal generator.

Experiments are taken under two different conditions: ambient and hot conditions. In the ambient condition, experiments are implemented in room temperature with approximately 300 K without the inclusion of neither a heating element nor a cold heat exchanger. On the other hand, in the hot condition, the tested temperature ranges from 333 K to 373 K with an increment of 20 K. The temperature at the CHX is fixed at 290 K. The experimental investigation is carried out by varying the thickness of the stainless steel mesh. The tested number of regenerator layers are ranging from 10 to 50 layers with increments of 20 layers. The multi-microphone travelling-wave technique is performed to determine the traveling-wave components in the complex pressure equation in order to determine the acoustic energy dissipation of the regenerator.

6.4 Multi-Microphone Travelling-Wave Technique

The complex pressure in a tube is the sum of two travelling waves which can be expressed by Equations (6.1) and (6.2) [100-102]:

$$p_1 = C_+ e^{-i\varepsilon dx_1} + C_- e^{i\varepsilon dx_1} \quad (6.1)$$

$$p_2 = C_+ e^{-i\varepsilon dx_2} + C_- e^{i\varepsilon dx_2} \quad (6.2)$$

Where p_1 is the complex pressure at microphone 1 and dx is the distance between the microphone and the sample. ε represents the complex wave number which is given by Equation (6.3) [119]:

$$\varepsilon = \frac{w}{c} \sqrt{\frac{1+(\gamma-1)f_k}{1-f_v}} \quad (6.3)$$

Where f_k and f_v are the thermal Rott function and the viscous Rott function respectively which are given by Equations (6.4) and (6.5) [119]:

$$f_k = \frac{(1-i)\delta_k}{2R_H} \quad (6.4)$$

$$f_v = \frac{(1-i)\delta_v}{2R_H} \quad (6.5)$$

For cylindrical resonator ducts, $R=2R_H$. δ_k is the thermal penetration depth and δ_v is the viscous penetration depth which are defined by Equations (1.4) and (1.5) respectively. Hence the complex wave number can also be written as the sum of a real and imaginary component as given by Equation (6.6) [119]:

$$\varepsilon = k' - ik'' \quad (6.6)$$

In a one dimensional wave propagation field, the two pressure waves can be decomposed into incident wave, C_+ and reflected wave, C_- respectively. The coefficients C_+ and C_- can be obtained by rearranging Equations (6.1) and (6.2) to become Equations (6.7) and (6.8) [100-102]:

$$C_+ = \frac{p_2 e^{i\varepsilon dx_1} - p_1 e^{i\varepsilon dx_2}}{2i \sin \varepsilon (dx_1 - dx_2)} \quad (6.7)$$

$$C_- = \frac{p_1 e^{-i\varepsilon dx_2} - p_2 e^{-i\varepsilon dx_1}}{2i \sin \varepsilon (dx_1 - dx_2)} \quad (6.8)$$

However when using the two-microphone method to determine the leftward and rightward travelling wave amplitudes, the distance between the two microphones is very critical. The two-microphone method fails if Equation (6.9) not equals to zero:

$$\sin \varepsilon (dx_1 - dx_2) \neq 0 \quad (6.9)$$

And even when $\sin \varepsilon (dx_1 - dx_2)$ is close to zero, this method is very sensitive to errors. This situation can be avoided easily when the measurements are done at a fixed frequency by choosing the microphone positions correctly, but for the whole frequency range this is a real problem. One way to overcome this problem is to use more than two microphones in what is known as the multi-microphone method. When a number of n microphones are used, at positions dx_1, dx_2, \dots, dx_n measuring pressure p_1, p_2, \dots, p_n the travelling wave components C_+ and C_- are described by the following over-determined linear matrix equation (for $n > 2$) as shown in Equations (6.10) through (6.17) [100-102]:

$$Kx = P \quad (6.10)$$

Where

$$K = \begin{bmatrix} \exp(-i\varepsilon dx_1) & \exp(i\varepsilon dx_1) \\ \exp(-i\varepsilon dx_2) & \exp(i\varepsilon dx_2) \\ \vdots & \vdots \\ \exp(-i\varepsilon dx_n) & \exp(i\varepsilon dx_n) \end{bmatrix} \quad (6.11)$$

$$x = \begin{bmatrix} C_+ \\ C_- \end{bmatrix} \quad (6.12)$$

$$P = \begin{bmatrix} p_1 \\ p_2 \\ \vdots \\ p_n \end{bmatrix} \quad (6.13)$$

One can compute the optimal solution for x using the least-squares method. The best approximate solution for x ($\|P-Kx\|$) is obtained by using the Moore-Penrose generalised inverse K^+ [120]:

$$x = K^+P = (K^H K)^{-1} K^H P \quad (6.14)$$

Where K^H denotes the Hermitian matrix of K . Using the matrix definition of K in Equation (6.10) [100-102]:

$$K^H K = \begin{pmatrix} \sum_{j=1}^n \exp(2k'' dx_j) & \sum_{j=1}^n \exp(2ik' dx_j) \\ \sum_{j=1}^n \exp(2k'' dx_j) & \sum_{j=1}^n \exp(2ik' dx_j) \end{pmatrix} \quad (6.15)$$

By applying Cramer's rule to Equation (6.14) and substituting Equation (6.15) x is obtained by the following expression [100-102]:

$$x = \frac{1}{\det(K^H K)} \begin{pmatrix} \sum_{j=1}^n p_j e^{i\varepsilon^* dx_j} \sum_{l=1}^n e^{-2k'' dx_l} - \sum_{j=1}^n p_j e^{-i\varepsilon^* dx_j} \sum_{l=1}^n e^{2ik' dx_l} \\ \sum_{j=1}^n p_j e^{-i\varepsilon^* dx_j} \sum_{l=1}^n e^{2k'' dx_l} - \sum_{j=1}^n p_j e^{i\varepsilon^* dx_j} \sum_{l=1}^n e^{-2ik' dx_l} \end{pmatrix} \quad (6.16)$$

Where (*) denotes the complex conjugate. The denominator in Equation (6.16) is equal to zero when $\det(K^H K) = 0$. As

$$\det(K^H K) = \left(\sum_{j=1}^n e^{2i\varepsilon dx_j} \right) \left(\sum_{l=1}^n e^{-2i\varepsilon dx_l} \right) - n^2 \quad (6.17)$$

By using $n = 3$ in Equation (6.17) (because three microphones are used in both upstream and downstream of the tube) and the $\det(K^H K) = 0$ if $\cos 2\varepsilon(dx_1 - dx_2)$

= 1. The travelling-wave components, C_+ and C_- can be determined with the aid of the multi-microphone travelling-wave technique by using Equations (6.1) through (6.17) which are then used to calculate the acoustic energy losses in the next section.

6.5 Acoustic Energy Losses

The acoustic energy flow in the system is determined by using microphones. Acoustic energy loss is an important indicator that can effectively determine how much sound energy is dissipated in the regenerator. The dissipation of acoustic energy in the regenerator is obtained by employing the multi-microphone travelling-wave technique. This method is based on measuring the acoustic pressures at two or more different positions in the engine. The calculations are performed on both the upstream and the downstream of the tubes. The total amount of acoustic energy loss is obtained by taking the difference of the resultant acoustic energy between upstream and downstream of the system [102]:

$$\dot{W} = \frac{A}{2\rho c} (|C_+|^2 - |C_-|^2) \quad (6.18)$$

Where A is the cross-sectional area of the resonator, ρ is the density of air and c is the speed of sound.

6.6 Womersley Number and the Standing Wave Ratio

It is more convenient to describe the problem with dimensionless parameters as it reduces the number of variable required to completely describe a problem. There are several dimensionless numbers used in this study. Womersley

number denotes the ratio of hydraulic radius to viscous penetration depth as expressed by Equation (6.19):

$$W_o = \sqrt{2} \frac{r_h}{\delta_v} \quad (6.19)$$

Where r_h and δ_v are the hydraulic radius and the viscous boundary layer thickness of the regenerator respectively.

Standing waves occur when two traveling waves with the same frequency and mode, but travelling in two opposite directions are combined. Standing waves are characterised by a static pattern of nodes and antinodes, areas where there is no propagation of energy. When an acoustic wave encounters a surface, part of the energy will be reflected. If entire wave is reflected with no shift in phase, this will lead to a node, a point where the sum of the amplitude of the incident wave and reflected wave is zero. However, very often the reflection coefficient is not unity, and the standing wave pattern is not complete. In this case, the amplitude at the nodes is no longer zero and the wave field is regarded as being partly standing wave and partly travelling wave. This is commonly described by the standing wave ratio, SWR which is expressed by the following Equation (6.20) [121]:

$$SWR = |p_{max}| / |p_{min}| \quad (6.20)$$

Where $|p_{max}| = |p_i|(1+|R|)$ is the maximum pressure and $|p_{min}| = |p_i|(1-|R|)$ is the minimum pressure, R represents the reflection coefficient and p_i is the incident pressure wave. The maximum pressure occurs when the incident and reflected waves are in phase, and the minimum pressure happens when the waves are out of phase. The SWR can also be determined in terms of complex amplitudes of the waves as given by Equation (6.21) [121]:

$$SWR = (A+B)/(A-B) \quad (6.21)$$

Where the amplitude at the maximum pressure is $A+B$, and the amplitude at the minimum pressure is $A-B$.

6.7 Results and Discussions of Losses in the Regenerator

The regenerator is the heart of a thermoacoustic device. The acoustic energy dissipation in the engine is mainly contributed by the thermoviscous losses in the regenerator. Despite the amount of useful work could be increased by using more regenerator layers but attenuation would be increased at the same time. Therefore the regenerator length must be chosen wisely by compromising between amplification and attenuation effects. The regenerator length should be kept short with respect to the acoustic wavelength, so that the acoustic field is not significantly altered. As the regenerator length is increased, the viscous and thermal dissipation will also be increased, reducing the overall efficiency of the system. Nevertheless, if the regenerator length is increased then more heat can be converted into useful work. As a result, higher temperature difference and larger power output can be obtained. The optimal regenerator length should be obtained by balancing these effects.

6.7.1 Thermal Energy Flow in the Regenerator

The thermal energy flow in the regenerator is examined under a static acoustic flow when the loudspeaker is turned off. Temperatures are recorded at both hot and cold heat exchangers of the straight tube configuration. The time taken for the heat to transfer from one side to the other side of the regenerator depends on the regenerator length. This time is measured by the time lag for peak of heat pulse to reach from the hot end to the cold end of the regenerator.

Figure 6.5 demonstrates the normalised time lag for the heat waves to transfer between both ends of the regenerator. The normalised time lag is obtained by using Equation (6.22).

$$t_N = \frac{t_{lag}}{t_{lag_10\ mesh}} \quad (6.22)$$

Where t_{lag} is the time lag and $t_{lag_10\ mesh}$ is the time lag obtained for 10 mesh. It can be observed that the normalised time lag is increased linearly with the number of mesh layers used. This is because the increase in the number of regenerator layers leads to an increase of the time taken for the heat waves to transfer from the hot end to the cold end through the solid part of the regenerator.

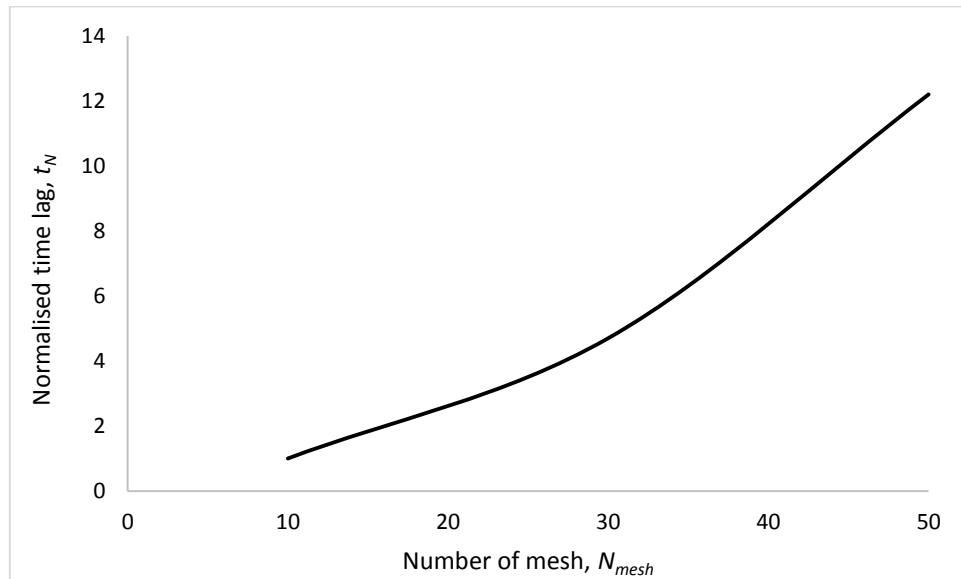


Figure 6.5: Normalised time lag for the heat to transfer from hot end to cold end of regenerator.

Figure 6.6 shows the normalisation of temperature for both heat exchangers. The normalised temperature is determined using the Equation (6.23).

$$T_N = \frac{T}{T_{cold_50\ mesh}} \quad (6.23)$$

Where T is the temperature of the heat exchanger and $T_{cold_50\ mesh}$ is the temperature of the CHX when 50 mesh is investigated. When 10 regenerator layers are tested, the normalised temperature difference, ΔT_N between the hot and the cold heat exchangers is lower as compared to the higher number of mesh layers as shown in Figure 6.6.

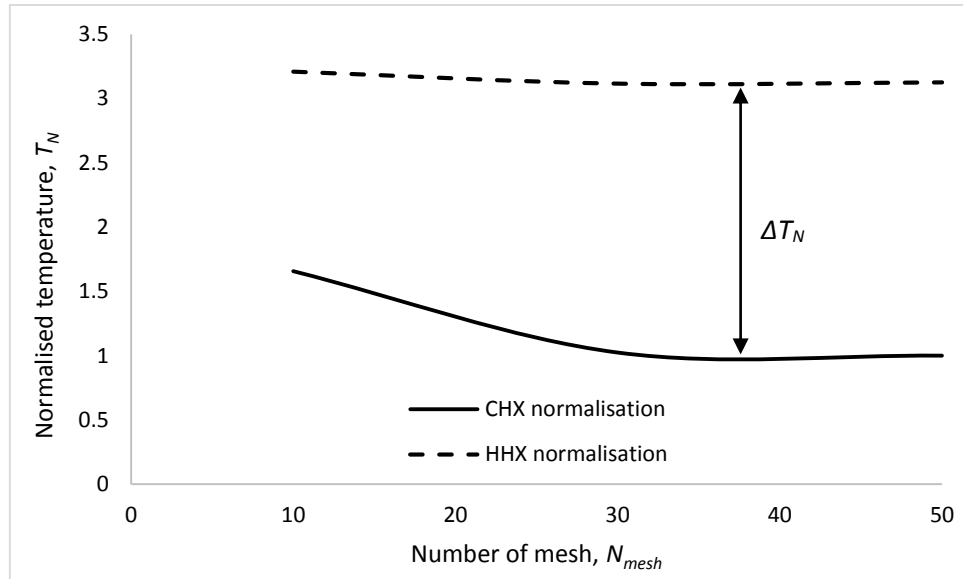


Figure 6.6: Normalised temperature for cold and hot heat exchangers.

As the regenerator layer increases, the total heat transfer from hot end to the cold end decreases. This behaviour tally with the results obtained in Figure 6.5 because as the regenerator becomes thicker, the thermal resistance of the regenerator increases, hence longer time is needed for the heat wave to transfer from the hot end to the cold end. It can be deduced that when the tested mesh is less than 30 layers, both conduction through the solid part of regenerator and convection of the gas parcel are contributing to the total heat transfer between both ends of the regenerator. However, when more than 30 layers of mesh are used, the heat transfer is dominated by conduction in the regenerator. More flow resistance is generated after 30 mesh while the

normalised temperature difference remains constant. Hence, it is unbeneficial to add more meshes after 30 mesh as shown in Figure 6.6.

The real time temperature difference profile between the cold and the hot heat exchangers is depicted in Figure 6.7. The higher the number of regenerator layers, the higher the temperature difference between the cold and the hot exchangers. This is because the increase of the regenerator layers will increase the distance and the resistance for the heat wave to flow from the hot end to the cold end of the regenerator. It can be seen that 10 layers of mesh is dissipating the heat faster in a shorter period time as compared to the other two tested meshes which take a longer time to dissipate the heat in the regenerator. After 30 mesh, there is no significant increase in the regeneration effect which is supported with the behaviour in Figure 6.6.

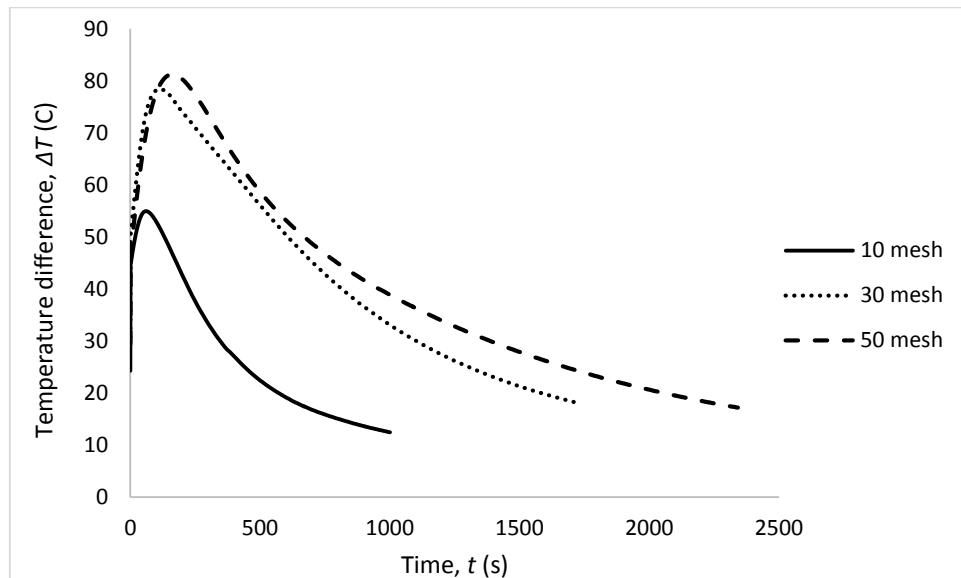


Figure 6.7: Real time temperature difference between the cold and the hot heat exchangers in degree Celsius for different number of meshes.

6.7.2 Acoustic Losses in the Regenerator

Acoustic energy loss is a performance indicator which can effectively determine the flow resistance of the regenerator. There are total four different number of meshes under examination including zero mesh where there is no regenerator in the test section. Both upstream and downstream energies were normalised against the upstream energy. The downstream normalised energy is obtained using the Equation (6.24).

$$E_N = \frac{E_D}{E_U} \quad (6.24)$$

Where E_D and E_U are the downstream energy and the upstream energy respectively. The acoustic energy loss through the regenerator is obtained as the difference between the upstream and downstream energies. Since a loudspeaker is used to drive the acoustic oscillation in the system, it can be considered as a travelling wave heat pump instead of an engine. In room temperature condition, the acoustic energy is studied without the inclusion of heat exchangers. The general trend found is that the acoustic energy loss decreases as the frequency increases. Figure 6.8 illustrates the effect of changing the frequency of the speaker on the acoustic energy dissipation for different mesh arrangements. When zero mesh is considered, majority of acoustic energy is dissipated on the internal surfaces of the resonator (viscous interaction with the resonator wall). The loss of acoustic energy is also due to the change in cross-sectional area when the acoustic field experiences sudden expansion and contraction at the test section. The order of acoustic energy dissipation can be seen clearly as manifested in Figure 6.8. Highest acoustic energy loss is obtained when 50 layers of mesh is tested and zero number of mesh has the least acoustic energy loss. The interactions between the oscillating fluid and the regenerator causes viscous dissipation which is known

to be the main contributor to the acoustic energy loss through the regenerator. The viscous losses are due to the viscosity that dissipates acoustic energy by viscous shear in the viscous boundary layer. In essence, a regenerator possesses extremely narrow pores, smaller than the viscous penetration depth. Owing to the perfect thermal contact between the working fluid (gas parcels) and the solid material, the dissipation in the regenerator is dominated by viscous losses.

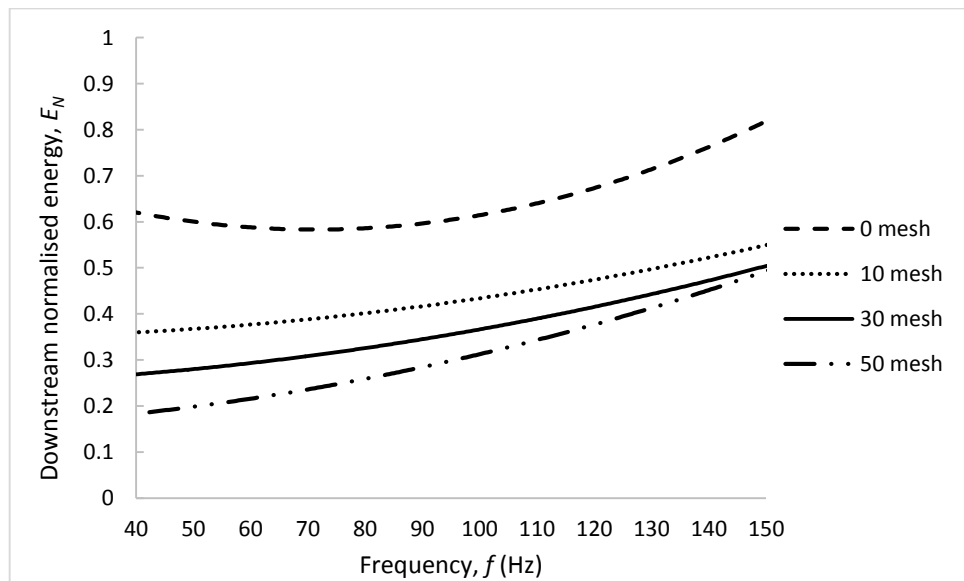


Figure 6.8: Downstream normalised energy against frequency for different number of regenerator meshes in ambient condition.

To give physical insight to the problem, Womersley number is plotted with respect to frequency as displayed in Figure 6.9. At lower frequencies, the acoustic energy loss is high because of low Womersley number which corresponds to large viscous penetration depth. At higher frequencies, on the other hand, Womersley number is high which means small viscous penetration depth thus lower acoustic energy dissipation. The change in temperature at the HHX only have a small influence on the Womersley number, meaning that

viscous losses are slightly unaffected by the input thermal energy. Figure 6.10 shows the Womersley number versus temperature for different frequencies.

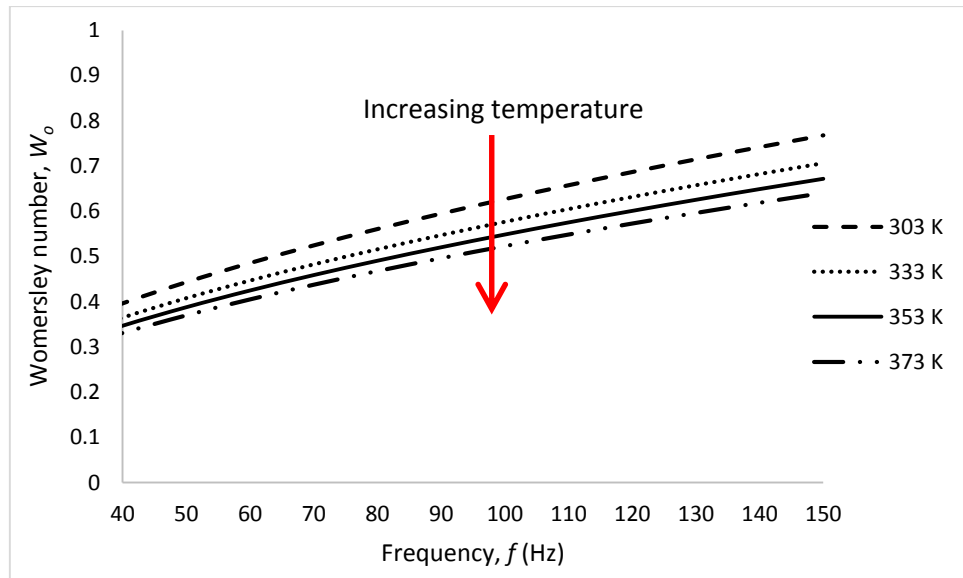


Figure 6.9: Womersley number as a function of frequency for different temperatures at the HHX.

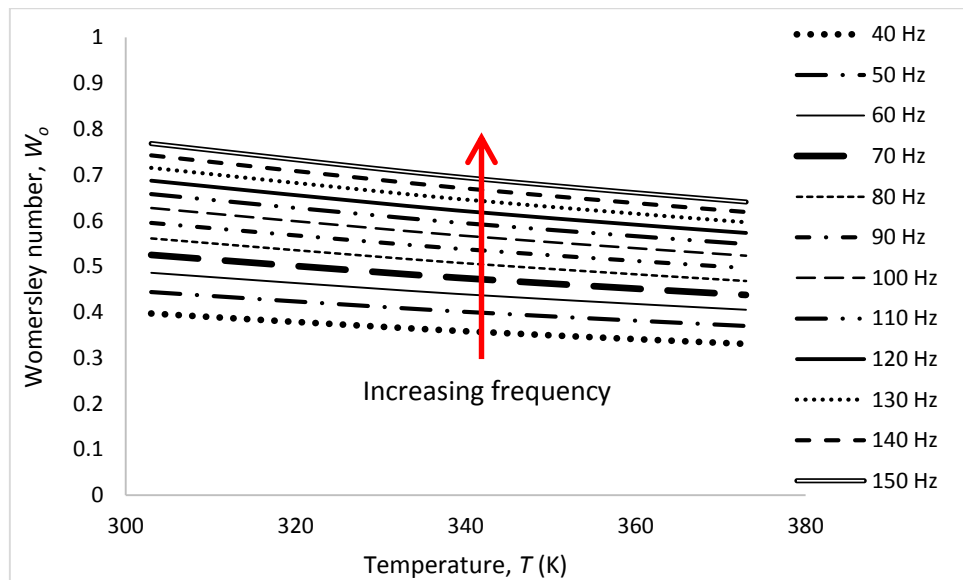


Figure 6.10: Womersley number versus temperature for different frequencies.

Similar behaviours are exhibited on the tested number of meshes when heat is supplied to the HHX. When heating is involved, the loudspeaker plays a role to drive the travelling-wave TAE to bring the pressure disturbance. The downstream normalised energy increases almost monotonically with the frequency as depicted in Figure 6.11. Comparing Figures 6.8 and 6.11, it can be observed that the influence of different mesh arrangements on the acoustic energy dissipation in ambient temperature condition is very significant. However, this effect is reduced especially at the low frequency range when heat is supplied to the system through the HHX. Besides that, at higher temperature, the thermal losses however are minimum, acoustic energy dissipation is mainly due to viscous penetration depth as by adding the same number of meshes have only a small impact on the increase in losses when compared to ambient condition. Because at high temperature, the viscous losses is dominant as well. Moreover, there are small amount of losses occur at the regenerator ends due to the vortices formed when sudden change of cross-sectional area of the gas. Figure 6.12 shows the implication of varying the temperature at the HHX on the acoustic energy loss. It can be deduced that only minor losses are due to thermal boundary layer as the amount of acoustic energy dissipation is almost the same when varying the temperature.

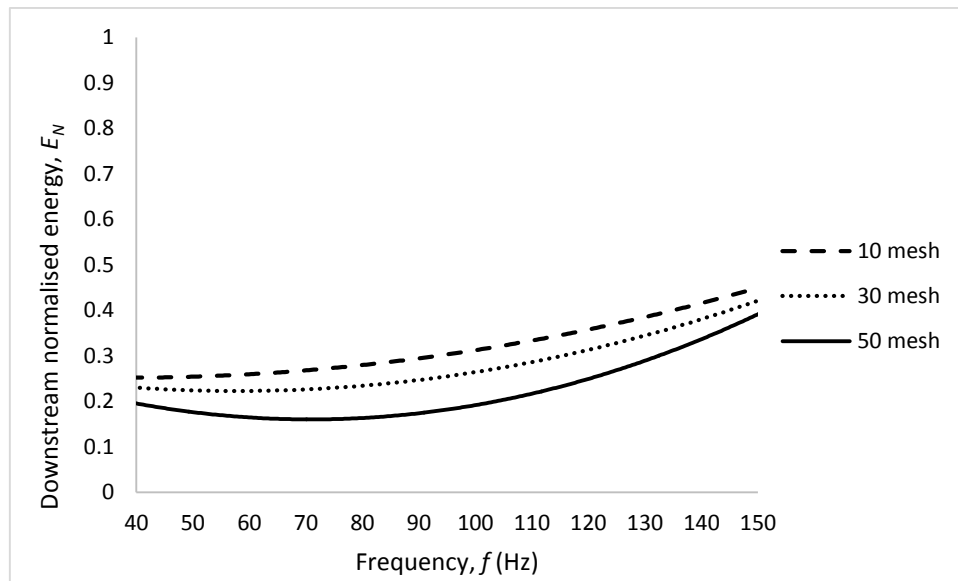


Figure 6.11: Downstream normalised energy against frequency for different number of regenerator meshes when the temperature at the HHX is 373K.

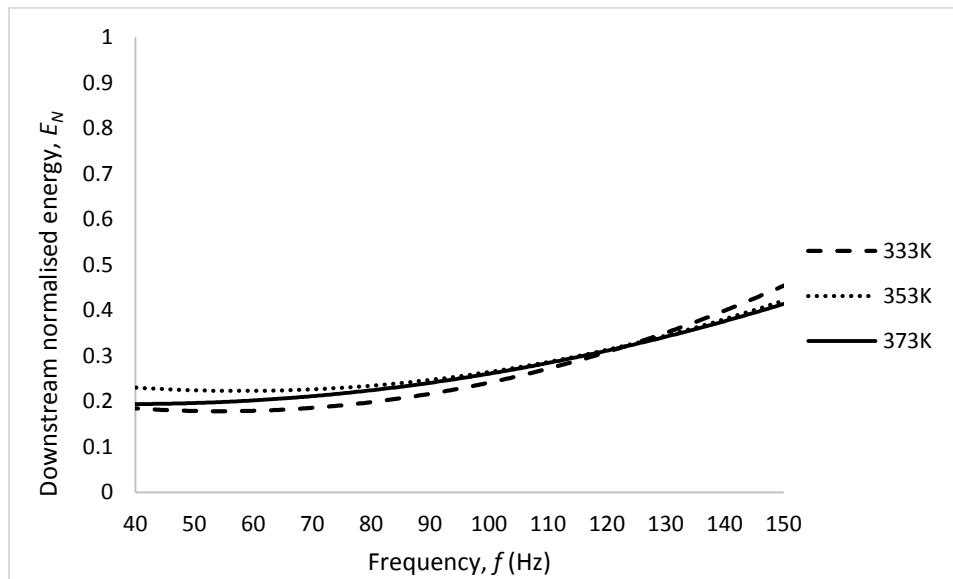


Figure 6.12: Downstream normalised energy against frequency for different temperatures at the HHX when 30 layers of regenerator.

Furthermore, the loss in acoustic energy in hot condition is slightly lower than that in the ambient condition. As described by Ceperley [31] and demonstrated in detail by Biwa et al. [122], traveling waves passing through the regenerator

will experience thermoacoustic energy conversion resulting in both amplification or attenuation of the wave depending on whether it propagates against or along the temperature gradient within the regenerator. In another words, amplification or attenuation of the wave depends strongly on the incident and reflection components of the wave. In thermoacoustic context, the standing wave component is the result of the impedance mismatch between the incident sound waves and the regenerator or the termination end in a tube. SWR also acts as an important indicator which can determine how much reflection in both upstream and downstream of the system. The incident component of the acoustic wave is always higher than the reflected component in both upstream and downstream of the resonator. This can be found by the SWR at the upstream and downstream is always positive and more than unity as seen in Figures 6.13 and 6.14. Nevertheless, the SWR at the upstream is lower than that at the downstream. At upstream, zero mesh and 50 mesh have highest and lowest SWR respectively, as oppose to the downstream, where 50 mesh is found to be the highest and zero mesh has the SWR closely equal to its upstream. As the regenerator thickness is increased, a decrease of SWR is experienced at the upstream because the reflected component of the acoustic waves as it passes through the resonator at the upstream from the downstream is decreased as well. When imposing a temperature gradient across the regenerator, the system encounters more amplification than attenuation. This can be explained because the standing wave components of the downstream in hot condition are relatively lower than in the room temperature condition, indicating a lower acoustic energy that is flowing in the opposite direction which results in a lower acoustic energy dissipation. The following sections of this chapter are discussed on the losses through the RHX in a RHX configuration experimental setup.

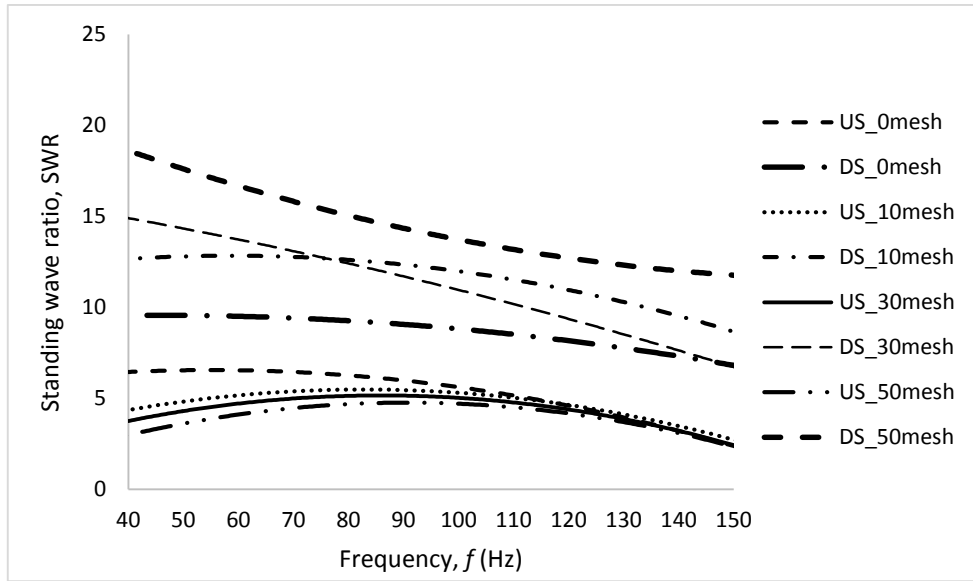


Figure 6.13: SWR against frequency for different number of regenerator meshes at both upstream (US) and downstream (DS) of the system in ambient condition.

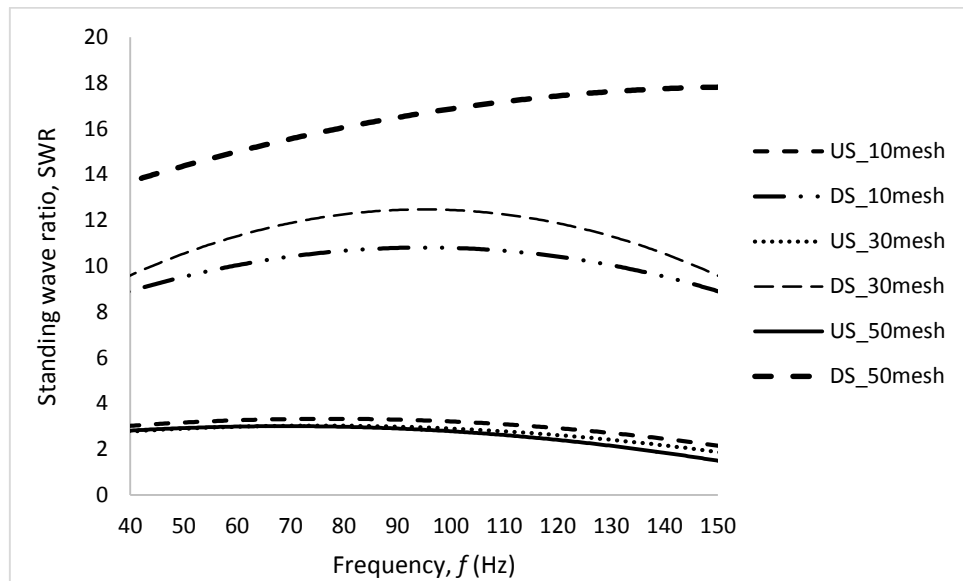


Figure 6.14: SWR against frequency for different number of regenerator meshes at both upstream (US) and downstream (DS) of the system when the temperature at the HHX is 373K.

6.8 Losses through the Radiant Heat Exchanger

The RHX (bulge or convolution) serves as a heating surface that transports the waste heat into the SCORE™ engine. However, the complex design of the investigated TAE experiences acoustic energy dissipation at the curvatures of tube (bends) in association with the RHXs. The energy transportation of the acoustic wave as it passes through the RHX of a RHX configuration is discussed in detailed in the following sections.

6.9 Experimental Setup of Radiant Heat Exchanger Configuration

To accurately simulate the condition of the SCORE™ engine, the experimental setup is designed to be as closely similar as possible to the actual existing TAE [41] by integrating with a RHX to form a RHX configuration. Figure 6.15 illustrates the experimental setup of RHX configuration that is under investigation in this work. The complete experimental apparatus is essentially a RHX configuration constituting of two short resonators and a long resonator with a total length of 3.575 m and a wall thickness of 5 mm. The internal cross-sectional areas of the resonator and the regenerator section are 0.0081 m² and 0.0122 m² respectively. Perspex is chosen as the material for the tubes and tapers. Instead of heating the regenerator directly, heat is supplied through an external RHX to the top layer of the regenerator. The heating element is clipped at the RHX to suit the operation of the actual engine. A short rectangular duct is placed between the resonators and the RHX. An aluminium heater box filled with insulation material is constructed and connected to the RHX externally to reduce thermal energy losses. The physical geometry of the RHXs is depicted in Figure 6.16.

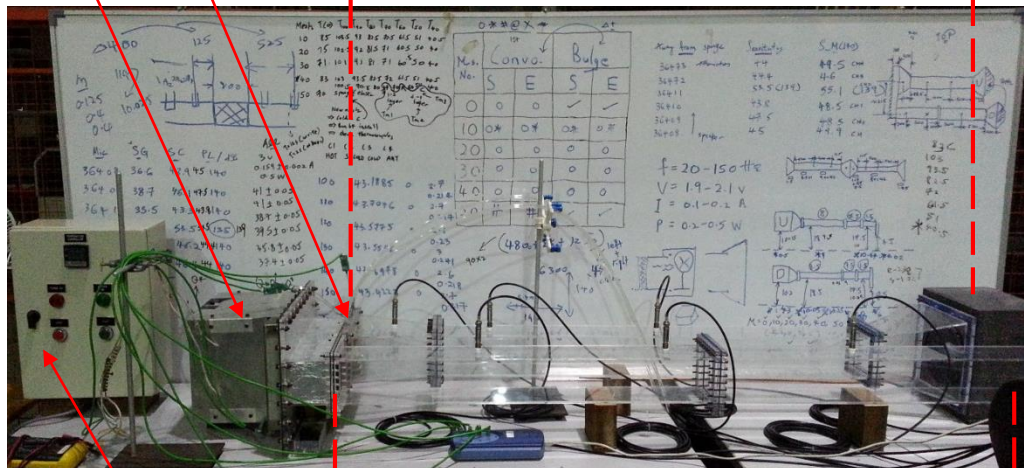


Regenerator

(a)

Aluminium
heater box

Upstream resonator



Heater
controller

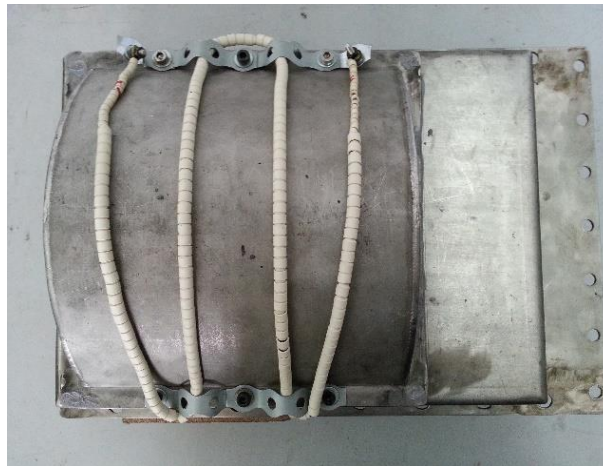
Downstream resonator

(b)

Figure 6.15: Layout of the RHX configuration in (a) ambient condition and (b) hot condition.

6.9.1 Radiant Heat Exchangers

The RHX serves as the hot heat exchanger in the second part of the experiment when RHX configuration is under investigation. It is responsible to transport the heat from the heating element into the thermoacoustic system. There are two types of RHXs: bulge and convolution as displayed in Figure 6.16. These RHXs are made to be easily installed to the engine so that the experiment could run with different configurations. Both the RHXs and their holder are machined out of stainless steel block.



(a)



(b)

Figure 6.16: Pattern of the heating element on the two types of RHX: (a) bulge and (b) convolution.

6.10 Instrumentation and Experimental Procedure for Radiant Heat Exchanger Configuration

Same measuring tools and experimental procedures are used for the RHX configuration. However, temperature measurements are carried out on the surface of the RHX instead of measuring the temperature at the first layer of the regenerator. The experimental investigation is implemented by changing the types of RHX while fixing the thickness of the regenerator. The multi-microphone travelling-wave technique is also performed to determine the acoustic losses through the RHX.

6.11 Results and Discussions of Losses through the Radiant Heat Exchanger

To study the travelling wave engine more precisely, the straight tube is integrated with a RHX in the downstream of the system to form to a RHX configuration. The complete setup of the RHX configuration is designed to be as closely similar as possible to the existing WHTAE [8]. Figures 6.17 and 6.18 show the downstream normalised energy in relation to the frequency for different temperatures at the RHX when 30 layers of regenerator for bulge and convolution respectively. It can be observed that the downstream normalised energy increases with the frequency in a linear manner for both RHXs regardless of the temperatures. The effect of changing the temperature on the RHXs is almost negligible as it only causes a small difference in the acoustic energy dissipation.

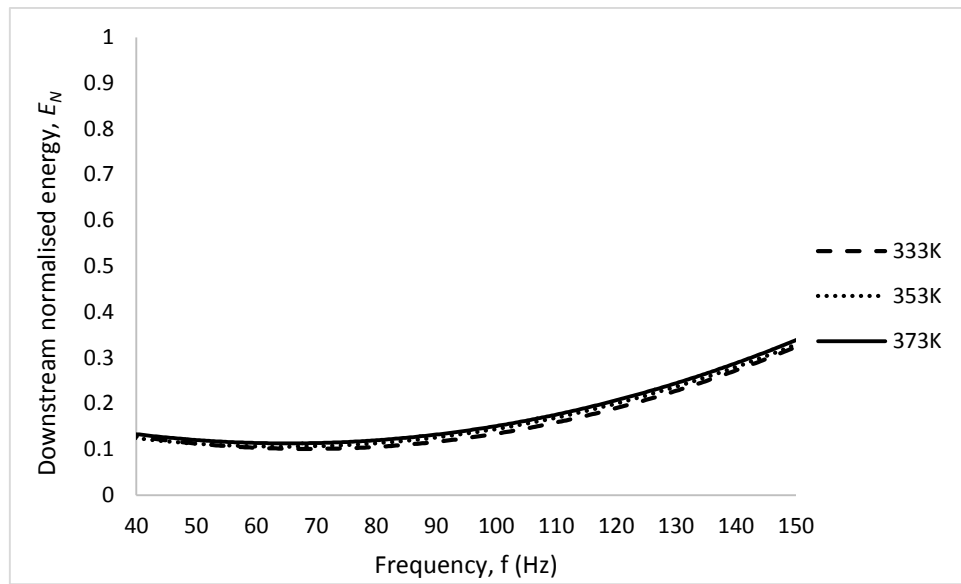


Figure 6.17: Downstream normalised energy against frequency for different temperatures at the RHX when 30 layers of regenerator for bulge.

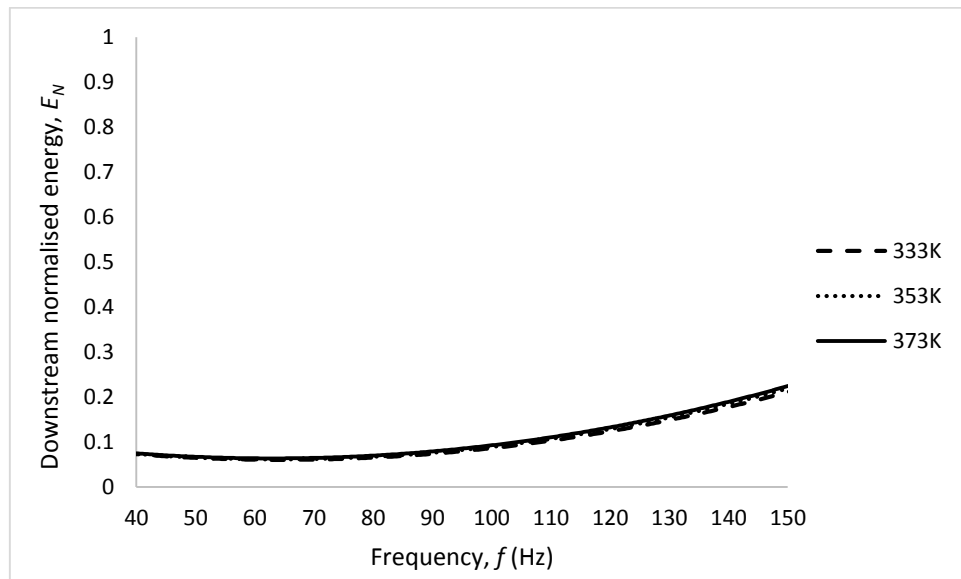


Figure 6.18: Downstream normalised energy against frequency for different temperatures at the RHX when 30 layers of regenerator for convolution.

Figures 6.19 and 6.20 depict the comparison of different configurations in terms of acoustic energy dissipation. The straight tube has the least acoustic energy dissipation follows by RHX configuration when bulge is used as the RHX

and the highest loss in acoustic energy is obtained for convolution RHX configuration. In the RHX configuration, the effect of the two sharp bends that forms the U-shaped flow path is significant. It can be inferred that the loss in acoustic energy for the straight tube is mainly due to the viscous losses in the regenerator while the acoustic dissipation for the RHX configuration is mainly caused by the vortices generated at the two sharp bends which form the U-shaped flow passage and the sudden change of cross-sectional area as the acoustic field propagates through the RHX.

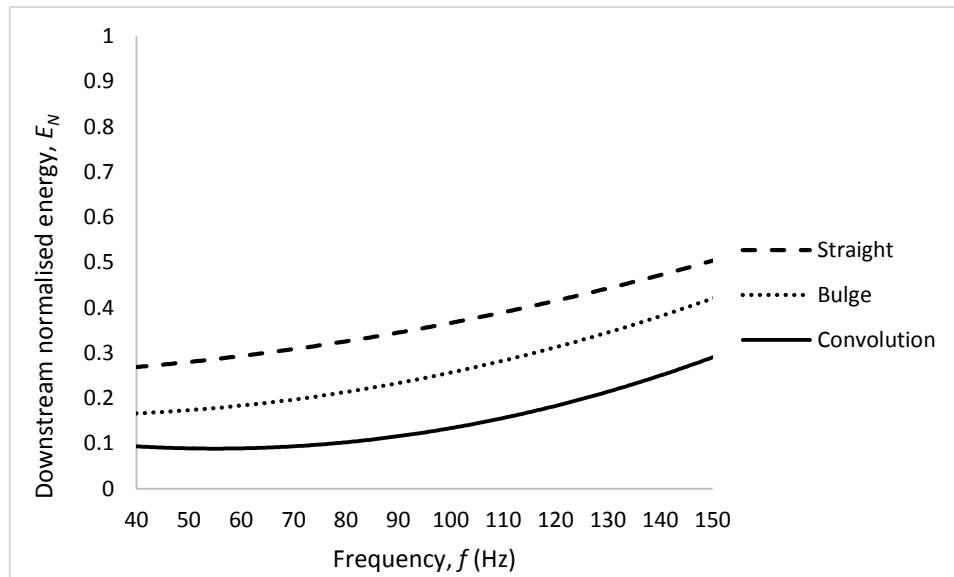


Figure 6.19: Downstream normalised energy as a function of frequency in ambient condition when 30 layers of regenerator for different configurations.

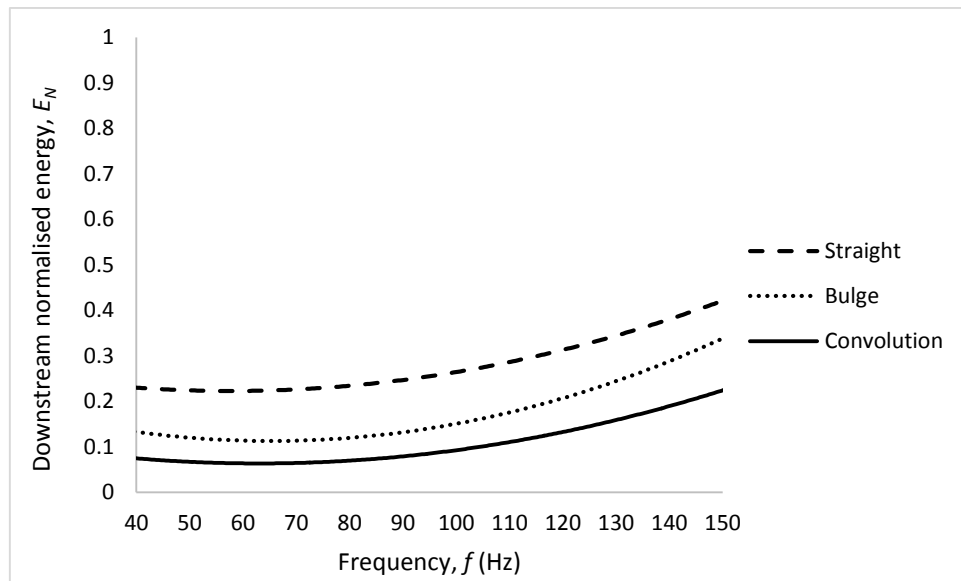


Figure 6.20: Downstream normalised energy against frequency when 30 layers of regenerator and the temperature at the HHX is 373K for different configurations.

Looking at the RHX configuration respective SWR results, it can be found that the SWR at the resonator upstream is nearly unity when 30 layers of mesh is examined regardless of the types of RHX, indicating a nearly pure travelling wave condition as shown in Figures 6.21 and 6.22. Both RHXs have SWR that are following the similar trend, with higher downstream SWR obtained by the convolution as compared to the bulge. This can be due to the propagation of acoustic field through many narrow and long channels of the convolution, as a result more reflections and viscous losses are produced as compared to the bulge which has a wider channel for the acoustic field to pass through.

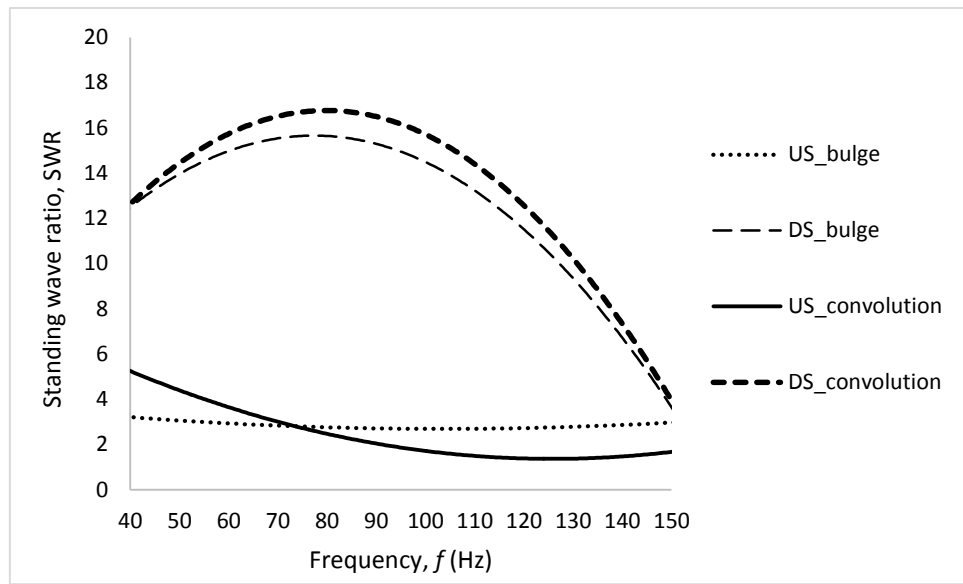


Figure 6.21: SWR as a function of frequency at both upstream (US) and downstream (DS) of the system in ambient condition when 30 layer of regenerator for different RHxs.

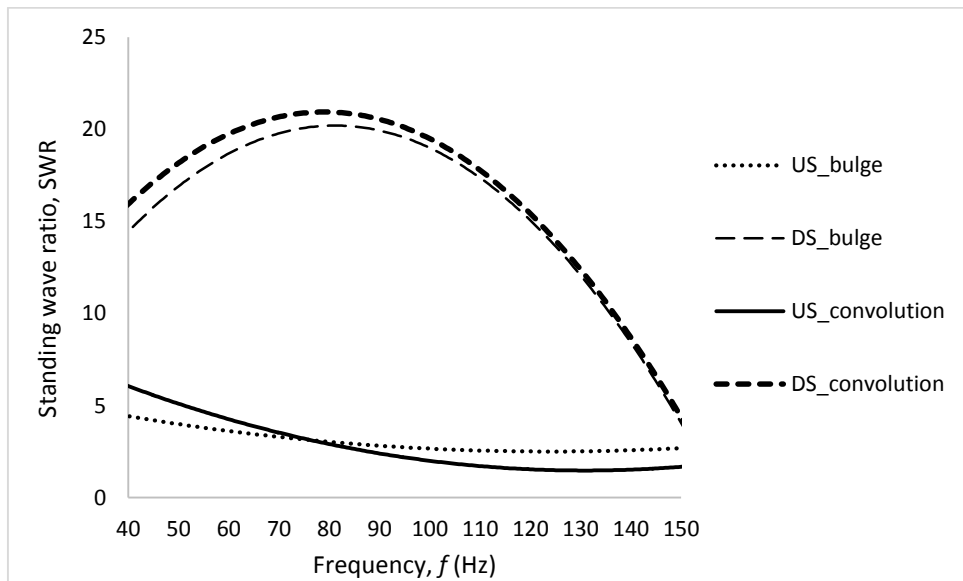


Figure 6.22: SWR against frequency at both upstream (US) and downstream (DS) of the system when 30 layers of regenerator and the temperature at the hot heat exchanger is 373K for different RHxs.

6.12 Concluding Remarks

- As the regenerator layer increases, the thermal resistance of the regenerator increases, hence longer time needed for the heat waves to transfer sufficient of heat to the cold end. When less than 30 layers of mesh, both conduction through the solid part of regenerator and convection of the gas parcel are contributing to the total heat transfer between both ends of the regenerator. However, when more than 30 layers of mesh are used, the heat is transferred mainly by conduction in the regenerator. After 30 mesh, more flow resistance is generated, there is no significant increase in the regeneration effect. Therefore, it is unbeneficial to add more meshes after 30 mesh.
- When zero mesh is considered, majority of acoustic energy is dissipated on the internal surfaces of the resonator. The loss of acoustic energy is also due to the sudden change in cross-sectional area when the acoustic field experiences sudden expansion and contraction at the test section.
- Highest acoustic energy loss is obtained when 50 layers of mesh is tested. Owing to the perfect thermal contact between the working fluid (gas parcels) and the solid material, the dissipation in the regenerator is dominated by viscous losses.
- The influence of different mesh arrangements on the acoustic energy dissipation is reduced especially at the low frequency range when heat is supplied to the system through the HHX.
- At higher temperature, only minor losses are due to thermal boundary layer, acoustic energy dissipation is mainly due to viscous penetration

depth as continue adding the same number of meshes have only a small impact on the increase in losses when compared to ambient condition.

- When imposing a temperature gradient across the regenerator, the system encounters more amplification than attenuation. Because the standing wave components of the downstream in hot condition are relatively lower than in the room temperature condition, indicating a lower acoustic energy that is flowing in the opposite direction which results in a lower acoustic energy dissipation.
- The effect of changing the temperatures on the RHXs is almost negligible as it only causes a small difference in the acoustic energy dissipation.
- Straight tube has the least acoustic energy dissipation follows by RHX configuration when bulge is used as the RHX and the highest loss in acoustic energy is obtained for convolution RHX configuration.
- The loss in acoustic energy for the straight tube is mainly due to the viscous losses in the regenerator while the acoustic dissipation for the RHX configuration is mainly caused by the vortices generated at the two 90° sharp bends and the sudden change of cross-sectional area.
- Convolution RHX configuration has higher downstream SWR as compared to the bulge RHX configuration. Because the acoustic field is propagating through many narrow and long channels of the convolution, as a result more reflections and viscous losses are produced as compared to the bulge which has a wider channel for the acoustic field to pass through.

Chapter 7

Numerical Modelling of the Waste-Heat Driven Thermoacoustic Engine

7.0 Introduction

Numerical modelling is an inexpensive alternative to study the effect of different parameters on the efficiency of WHTAE without the need of conducting costly experiments. This chapter makes use of the results from the previous chapters to validate the numerical models which can be used for further investigation of different parameters on the performance of WHTAE. DeltaEC software is fully utilised to model the thermoacoustic systems previously shown in chapter 5 and 6. First and foremost, the overview of DeltaEC modelling is introduced. Then, the governing equations used to model the WHTAE in DeltaEC is presented. The design of the DeltaEC models is divided into two stages. The first stage is the DeltaEC modelling and simulation of the attenuation effectiveness. The second stage consists of the numerical study of the acoustic energy dissipation in the WHTAE. The boundary conditions in the modelling of both the attenuation effectiveness and the acoustic losses in the WHTAE are also presented. By using the aforementioned multi-microphone

methods with the aid of user-defined function in DeltaEC, the numerical results obtained by DeltaEC are compared with the experimental results from the previous chapters. This is followed by detailed discussions on the comparison of results. The final section presents the concluding remarks of this chapter.

7.1 DeltaEC Modelling

Design environment for low-amplitude thermoacoustic energy conversion (DeltaEC) developed by Ward and Swift in Los Alamos National Laboratory, USA is an open-source thermoacoustic software, extensively used by researchers to evaluate the performance of the thermoacoustic devices with various operational and geometrical parameters [82]. DeltaEC can be used to study a variety of complicated thermoacoustic devices in the low-amplitude pressure range. It solves the one-dimensional wave equation in a gas or liquid, in a geometry defined by the user as a sequence of segments, such as ducts, compliances, transducers, and thermoacoustic stacks or regenerators. For each of these segments, the computer solves a one dimensional wave equation with temperature evolution by matching the pressure, volume velocity (also denoted as volume flow rate) and temperature at the interface of each segment as boundary conditions. The software uses a system of “guesses” and “targets” vectors, the former being generally uncontrolled parameters such as frequency or pressure amplitude, and the latter being parameters that can be controlled, such as dimensions or boundary conditions. The suitable selection of ‘guesses’ and ‘targets’ is the key to successful use of the program : the program will iteratively adjust the variables listed as ‘guesses’ to achieve the ‘target’ values. Another extraordinary useful and very versatile feature of DeltaEC is the Reverse Polish Notation (RPN) which is the user-defined function of the software. RPN allows the user to create nonstandard guesses, targets and simple algebraic calculations anywhere in a DeltaEC model.

7.2 Model Development

7.2.1 Governing Equations

The linear thermoacoustic theory for thermoacoustic effect was established by Rott [13, 15]. Equation (7.1) is the Rott's wave equation which is also known as Helmholtz equation [13, 15].

$$[1 + (\gamma - 1)f_k]U_1 + \frac{\gamma p_m}{w^2} \frac{d}{dx} \left(\frac{1-f_v}{\rho_m} \frac{dp_1}{dx} \right) - \frac{A^2}{w^2} \frac{f_k - f_v}{1-\sigma} \frac{1}{T_m} \frac{dT_m}{dx} \frac{dp_1}{dx} = 0 \quad (7.1)$$

Where p , U , T , ρ , σ , w , a and γ are the pressure, volume velocity, temperature, density, prandtl number, angular frequency, speed of sound and ratio of specific heat capacities of the gas respectively. f_k and f_v represent the spatially averaged thermal and viscous functions. The subscripts m and "1" indicate the mean and the first order of a variable, which usually has complex amplitude. A is the cross-sectional area. Equation (7.1) is established based on Rott's acoustic approximation and hence for the convenience of numerical computations, Equation (7.1) can also be written in the form of Equations (7.2) and (7.3) which are essentially the thermoacoustic version of momentum and continuity equations respectively.

$$dp_1 = - \frac{i w \rho_m dx / A}{1-f_v} U_1 \quad (7.2)$$

$$dU_1 = - \frac{i w A dx}{\gamma p_m} [1 + (\gamma - 1)f_k] p_1 + \frac{(f_k - f_v)}{(1-f_v)(1-\sigma)} \frac{dT_m}{T_m} U_1 \quad (7.3)$$

Based on the linear model, the Deltaec software integrates Equations (7.2) and (7.3) numerically, segment by segment, throughout the whole device based on the low amplitude acoustic approximation and sinusoidal time dependence [42, 46, 47, 123].

7.2.2 Boundary Conditions

7.2.2.1 Absorption Coefficient Experiment

The model is constructed by 83 segments including the 6 RPN segments which are used to indicate the microphone locations and 63 RPN segments after the HARDEND for the calculations of least squares technique. The impedance tube system is made out of 6 CONE segments and 6 DUCT segments. A total number of 3 GUESSES and 3 TARGETs are chosen. The very first segment (zeroth segment) has always been a BEGIN segment and will be used as a loudspeaker that generates a sinusoidal wave in this case. This segment contains global variables such as mean pressure, frequency, mean temperature and gas type. Calculations are done using a mean pressure $P_m = 1$ bar and a mean temperature $T_m = 300$ K. Air is used as the working gas. Perspex is selected as the material for the components in the model with the aid of User Defined Function (UDF). The HARDEND acts as a rigid backing to reflect the acoustic wave. Table 7.1 shows the dimensions and other details of the thermoacoustic system. The GUESS vector, which has three components in this case, shows what variables DeltaEC targets for a solution: the frequency, acoustic pressure and the volume flow rate. The initial guess of the frequency is 20 Hz, 50 Pa of acoustic pressure and the initial value of the volume flow rate is $0.005 \text{ m}^3\text{s}^{-1}$. Basically, DeltaEC integrates the wave equation from BEGIN to END. Refine the GUESS vector to find a solution to this acoustics problem that arrives at the HARDEND with zero complex volume flow rate amplitude. This is accomplished by getting the '0' values of the real and imaginary part of the inverse of the normalised specific impedance for the HARDEND segment into DeltaEC's TARGET vector. In addition, the experimental results of absorption coefficient when a rigid aluminium plate is chosen as the termination end in chapter 5 are

set to be the third component of the TARGET vector. The DeltaEC model for the complete experimental setup is shown schematically in Figure 7.1.

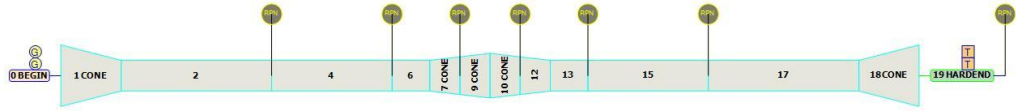


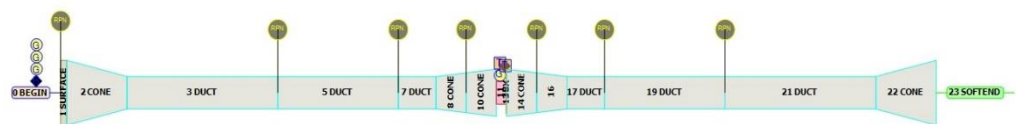
Figure 7.1: Schematic diagram of the impedance tube system produced in DeltaEC.

Table 7.1: Summary of the dimensions and other details of the impedance tube system.

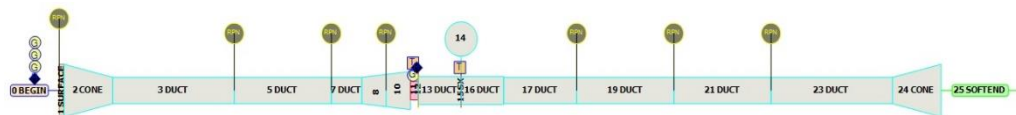
Segment	Area (m ²)	Length (m)	Material
0 BEGIN	-	-	-
1 CONE	A_1 0.0324 A_2 0.0081	0.2	Perspex
2 DUCT	0.0081	0.5	Perspex
3 RPN	-	-	-
4 DUCT	0.0081	0.4	Perspex
5 RPN	-	-	-
6 DUCT	0.0081	0.125	Perspex
7 CONE	A_1 0.0081 A_2 0.01215	0.1	Perspex
8 RPN	-	-	-
9 CONE	A_1 0.01215 A_2 0.0171	0.1	Perspex
10 CONE	A_1 0.0171 A_2 0.01215	0.1	Perspex
11 RPN	-	-	-
12 CONE	A_1 0.01215 A_2 0.0081	0.1	Perspex
13 DUCT	0.0081	0.125	Perspex
14 RPN	-	-	-
15 DUCT	0.0081	0.4	Perspex
16 RPN	-	-	-
17 DUCT	0.0081	0.5	Perspex
18 CONE	A_1 0.0081 A_2 0.0324	0.2	Perspex
19 HARDEND	-	-	-

7.2.2.2 Acoustic Energy Dissipation Experiment

The DeltaEC models for the two different configurations: straight tube and RHX configurations are shown schematically in Figure 7.2. The former model is basically the same as the designed model in the absorption coefficient experiment except now a regenerator which is sandwiched by two heat exchangers is included for investigation. On the other hand, the latter model comprises a compliance volume near the regenerator which is used to indicate the volume of the RHX. The numerical models for both configurations have two phases (phase 1 and phase 2) which are different from the number of GUESSES and TARGETs chosen.



(a)



(b)

Figure 7.2: Schematic diagram of the acoustic energy dissipation experiments in hot condition produced in DeltaEC: (a) straight tube configuration and (b) RHX configuration.

The straight tube configuration is constructed by 95 segments including the 6 RPN segments which are used to indicate the microphone locations and 71 RPN segments which are used to carry out the calculations of acoustic energy dissipation by using the multi-microphone method based on travelling-wave technique. The thermoacoustic system is made out of 6 CONE segments, 6

DUCT segments, 1 HX (parallel-plate CHX) segment, 1 STKSCREEN (stacked-screen regenerator) segment and 1 SX (stacked-screen HHX) segment. The first phase (phase 1) of the numerical model for the straight tube configuration has 5 GUESSES and 5 TARGETs whereas the second phase (phase 2) of its numerical model has a total number of 6 GUESSES and 6 TARGETs.

The first segment is a BEGIN segment followed by a SURFACE segment which is used to account for oscillatory thermal losses at the first end of the resonator and also used to target the acoustic power of the speaker. DUCTs and CONEs are used to form the upstream and downstream resonators of the system. Heat exchangers are used to inject or remove heat. The first law of thermodynamics insists that this heat must equal to the difference between the upstream and the downstream total power (\dot{H}_{tot}). Aluminium is selected as the material for the parallel-plate CHX with the aid of RPN. The material selected for both the stacked-screen regenerator and the stacked-screen HHX is stainless-steel. Perspex is used for the rest of the components in the TAE. Air is used as the working gas.

Moreover, the RHX configuration is made out of 100 segments including 6 RPN segments which are used to indicate the microphone locations and 74 RPN segments for the calculations of acoustic energy dissipation. The TAE is constructed by 4 CONE segments, 9 DUCT segments, 1 HX (parallel-plate CHX) segment, 1 STKSCREEN (stacked-screen regenerator) segment, 1 SX (stacked-screen HHX) segment and 1 COMPLIANCE segment. The simulations of the RHX configuration are carried out using the same number of GUESSES and TARGETs as chosen above for the two phases of its model.

The main difference between the two configurations is the modelling of the HHX. As mentioned in the previous chapters, the HHX in the RHX configuration is a RHX which has complicated geometry and is customised to suit the

application [41]. However, DeltaEC only consists of heat exchangers used in common thermoacoustic devices. The DeltaEC software also does not take into account the design of U-bend tube in association with the RHX. Another limitation would be the non-linear viscous mechanisms are not considered by the linear modelling software. Therefore, a compliance volume is integrated to the system to distinguish between the bulge and convolution RHXs. The compliance volume is defined as a lumped acoustic volume element which can be used to represent the physical volumes of the RHXs. Because DeltaEC is based on one-dimensional linear acoustic approximation, the amplitude of the acoustic oscillation will always keep to a minimum value to eliminate the non-linear effect [82]. The dimensions and other details of the RHX configuration is shown in Table 7.2.

Both configurations perform the calculations using an acoustic power of 0.2 W, a constant temperature at the CHX $T_c = 290$ K and a heat input of 1000W at the HHX. The regenerator length is varied from 1.8×10^{-3} m to 9×10^{-3} m whereas the temperature at the HHX is ranging from 333 K to 373 K. Another two target values are the real and imaginary part of the normalised specific impedances at the SOFTEND based on the results obtained from the absorption coefficient experiment when an elastic end is selected as the termination end. An additional component of the TARGET vector is included for the second phase of the numerical model by using the experimental results of the upstream normalised energy in chapter 6. The GUESS vector on the other hand consists of the same number of components as well. The initial guess of the mean temperature, acoustic pressure and volume velocity are taken as 300 K, 100 Pa and $1 \times 10^{-4} \text{ms}^{-1}$ respectively. A heat rate value of -50 W is chosen to be the initial value for the cold heat exchanger (HX) and the initial guess of the frequency is taken as 40 Hz. The porosity of the regenerator is chosen to be the additional component of the GUESS vector for the second phase of numerical model.

Equations (6.1) to (6.21) are used to carry out the acoustic energy dissipation calculations.

Table 7.2: Summary of the dimensions and other details of the RHX configuration.

Segment	Area (m ²)	Length (m)	Porosity	Material
0 BEGIN	-	-	-	-
1 SURFACE	0.0324	-	-	-
2 CONE	A_1 0.0324 A_2 0.0081	0.2	-	Perspex
3 DUCT	0.0081	0.5	-	Perspex
4 RPN	-	-	-	-
5 DUCT	0.0081	0.4	-	Perspex
6 RPN	-	-	-	-
7 DUCT	0.0081	0.125	-	Perspex
8 CONE	A_1 0.0081 A_2 0.01215	0.1	-	Perspex
9 RPN	-	-	-	-
10 CONE	A_1 0.01215 A_2 0.0171	0.1	-	Perspex
11 HX	0.00624	0.032	0.646	Aluminium
12 STKSCREEN	0.0171	0.00018 per layer	0.792	Stainless steel
13 DUCT	0.009	0.175	-	Perspex
14 COMPLIANCE	Surface_ A_{Bulge} 0.0424 Surface_ $A_{Convolution}$ 0.231	-	-	Perspex
15 SX	0.0171	0.00054	0.792	Stainless steel
16 DUCT	0.009	0.175	-	Perspex
17 DUCT	0.0081	0.3	-	Perspex
18 RPN	-	-	-	-
19 DUCT	0.0081	0.4	-	Perspex
20 RPN	-	-	-	-
21 DUCT	0.0081	0.4	-	Perspex
22 RPN	-	-	-	-
23 DUCT	0.0081	0.5	-	Perspex
24 CONE	A_1 0.0081 A_2 0.0324	0.2	-	Perspex
25 SOFTEND	-	-	-	-

Table 7.3: Summary of the number of GUESSES and TARGETs in both phases of the numerical model.

Phase		GUESSES	TARGETs
1	2	Frequency at BEGIN	Acoustic power of speaker
		Temperature at BEGIN	Temperature at HX (CHX)
		Acoustic pressure at BEGIN	Real part of normalised specific impedance of SOFTEND
		Volume velocity at BEGIN	Imaginary part of normalised specific impedance of SOFTEND
		Heat output of HX (CHX)	Heat input of SX (HHX)
		Porosity of STKSCREEN regenerator	Experimental results of upstream normalised energy

7.3 Results and Discussions

7.3.1 Comparison between the Different Types of Excitation Signals in the Absorption Coefficient Experiment

Two different types of excitation signals as described in section 4.3 are compared with the results predicted by DeltaEC. The numerical results produced by DeltaEC are found to be in an excellent agreement with the experimental results throughout all of the frequency range. However the coefficients are slightly overestimated by the numerical simulation at the frequency above 120 Hz as shown in Figures 7.3 and 7.4. Despite the chosen white noises are deemed to be suitable excitation signals but these signals cover a big range of frequency, making the data captured at the lower frequency range limited. However, it is a good evidence that the two types of experimented white noises are not affecting the attenuation as compared with the single frequency used in DeltaEC. It is difficult to obtain an ideal single frequency condition experimentally because of several factors such as the unwanted noises. On the other hand, in the DeltaEC environment, the software does not account for nonlinear effects as it solves only one-dimensional linear

discrete approximation problems. Besides that, DeltaEC uses ideal gas properties as well as adiabatic acoustic components in the calculations.

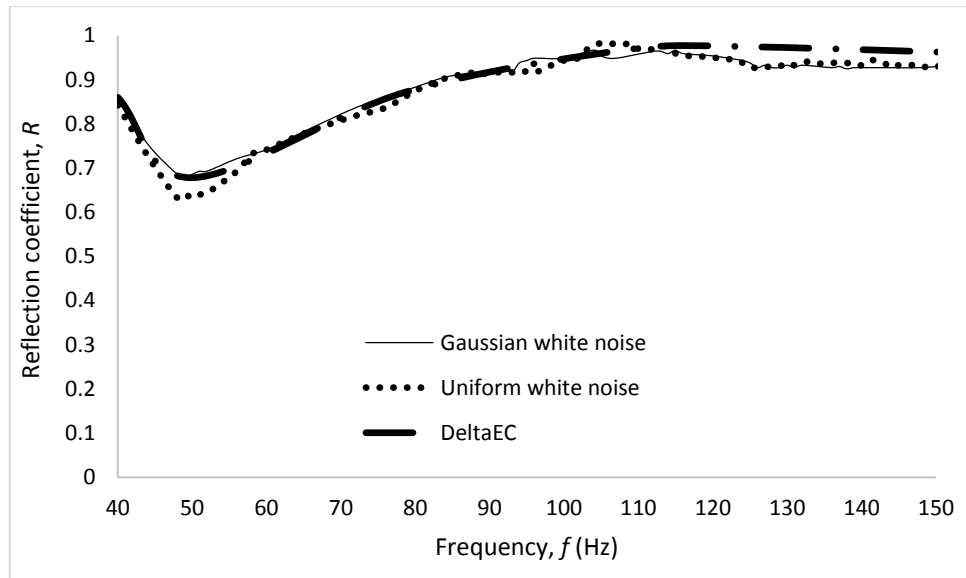


Figure 7.3: Reflection coefficient versus frequency when aluminium plate is under examination.

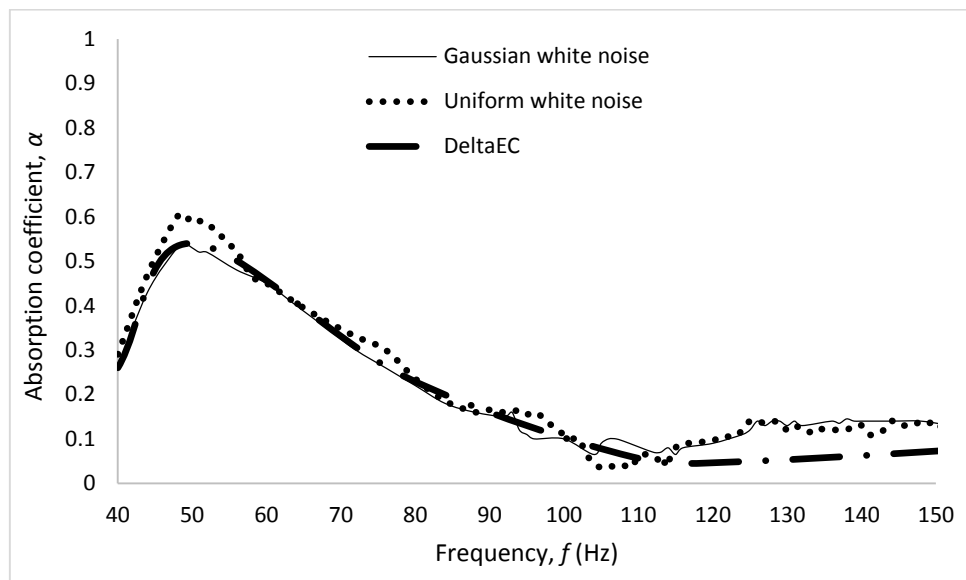
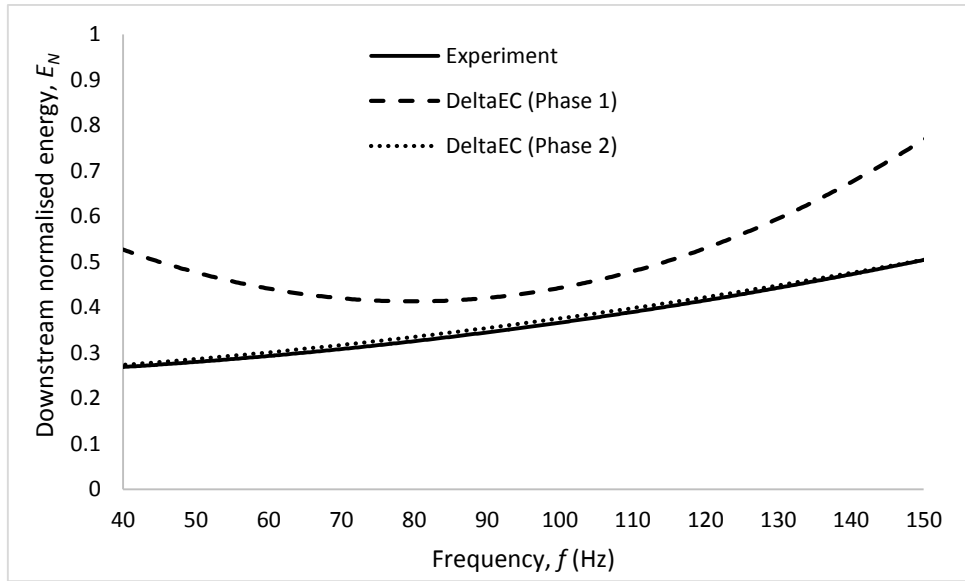


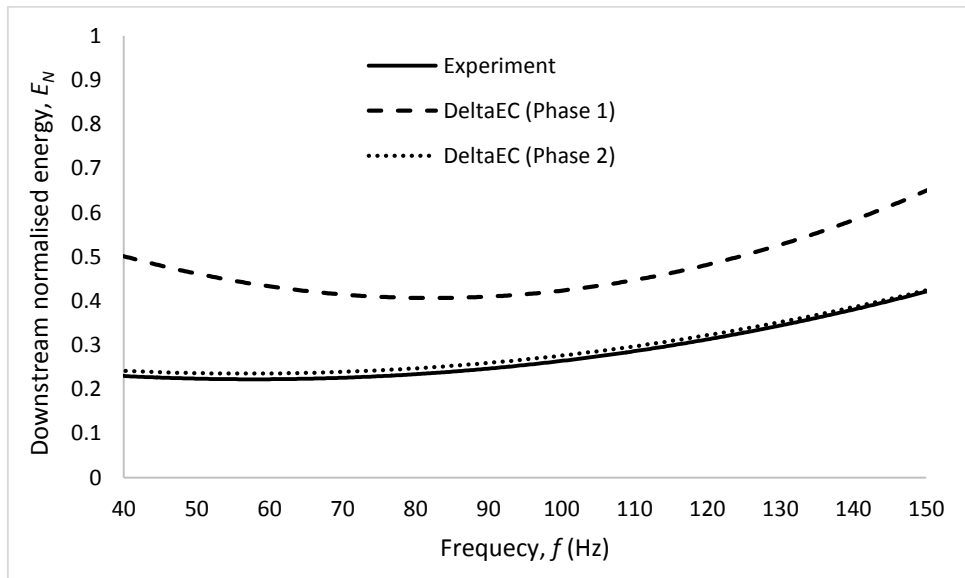
Figure 7.4: Absorption coefficient as a function of frequency when aluminium plate is used as the rigid backing.

7.3.2 Validation against the Experimental Results obtained in the Acoustic Dissipation Experiment

Figure 7.5 demonstrates the normalised downstream acoustic energy as a function of frequency for the straight tube configuration in both ambient and hot conditions. In the case when 30 mesh layers are used, phase 1 of the numerical model overestimates the downstream normalised energy in both ambient and hot conditions. The obvious deviation is probably due to the non-linear effect of the acoustic field is neglected in the numerical simulation. The discrepancies are also caused by the change of acoustic impedance at the attenuation end as the change of mesh numbers and frequencies would affect the acoustic properties of the absorbing material. It is noteworthy that the meshes are not symmetrically aligned to each other in series which leads to different in porosity, thus different of acoustic energy attenuation through the regenerator. The same number of mesh might not be completely identical in every experimental run. Therefore the acoustic energy loss is expected to be considerably lower as predicted by the phase 1 of the numerical model. In order to predict the experimental results more accurately, an additional pair of GUESS and TARGET components are chosen in the phase 2 of the numerical model. It can be observed that the phase 2 of the numerical model and experimental results agree well to each other, displaying almost the same amount of acoustic energy dissipation throughout the tested frequency as shown in Figure 7.5. The same behaviour is also exhibited in the results of SWR versus frequency where the phase 2 of the numerical model makes a better comparison with the experimental results as shown in Figure 7.6.



(a)



(b)

Figure 7.5: Downstream normalised energy versus frequency in (a) ambient condition and (b) hot condition when the temperature at the HHX is 373K for 30 layers of regenerator in straight tube configuration.

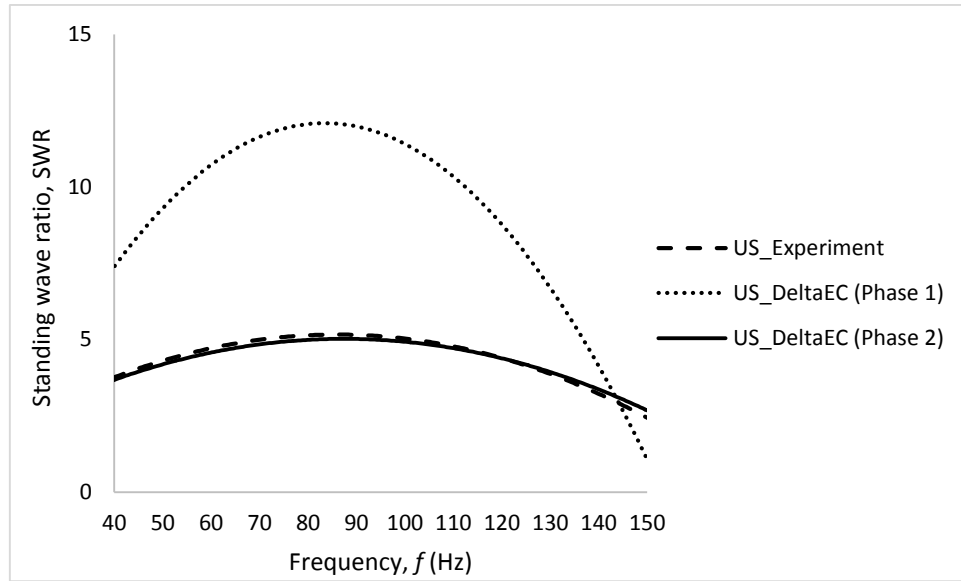
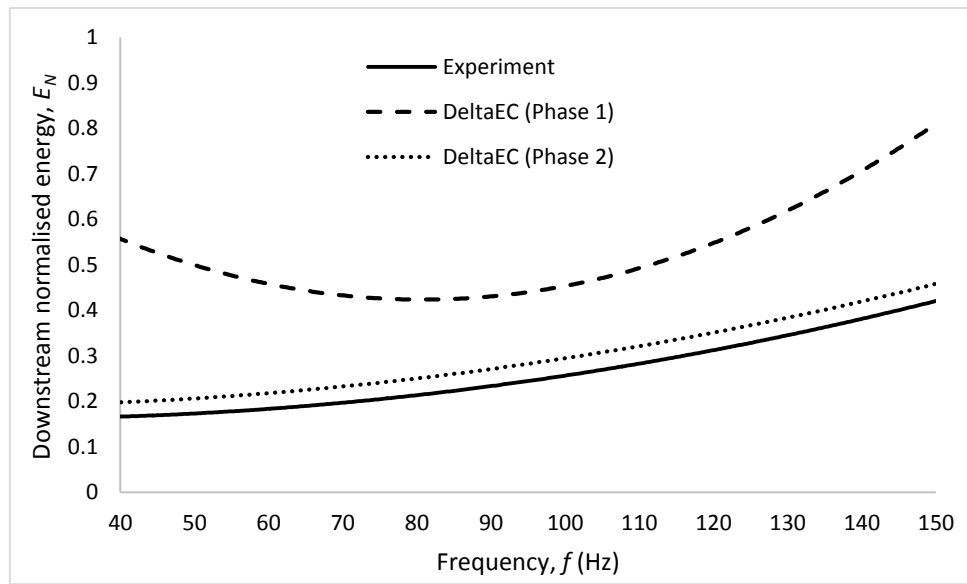


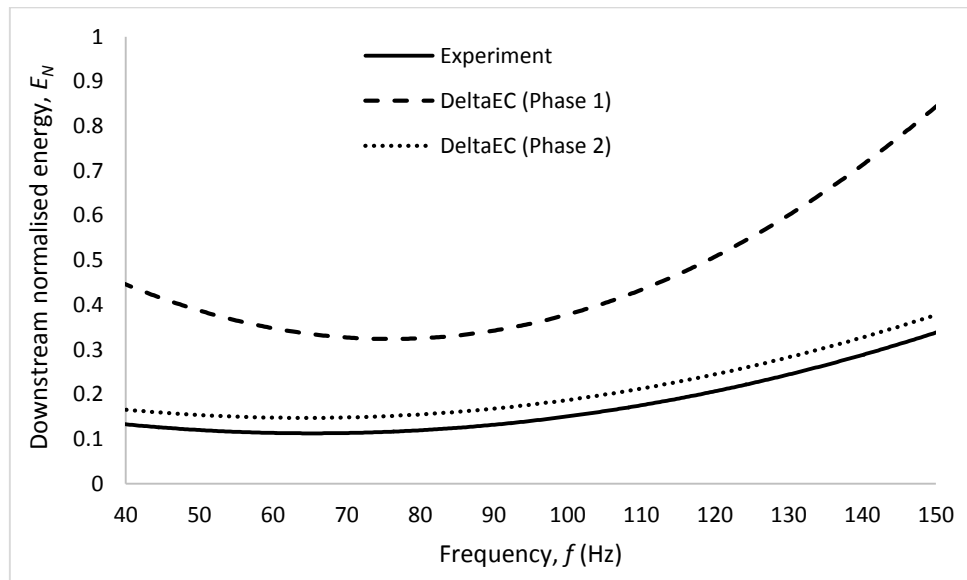
Figure 7.6: SWR versus frequency regenerator meshes at upstream (US) of the system in ambient condition when 30 layers of regenerator for straight tube configuration.

Figures 7.7 and 7.8 present the comparison of the DeltaEC results along with the experimental results plotted in terms of downstream normalised energy as a function of frequency at 373 K when 30 mesh is used as the regenerator for bulge and convolution respectively in both ambient and hot conditions. Phase 1 of the DeltaEC model is found to predict a higher downstream normalised energy in both ambient and hot conditions for both types of RHXs. The experimental results show almost linear increase of normalised downstream energy as frequency increases whereas the results of the phase 1 of the numerical model display a higher normalised downstream energy in the tested frequency range. The overestimation of results by the phase 1 of the numerical model is mainly due to the modelling of the RHXs. Both RHXs are modelled as a compliance in the DeltaEC which is essentially an enclosure with only its volume and area taken under consideration. Thus, the exact physical geometries for both bulge and convolution are not taken into account in the numerical simulation. Another restriction in DeltaEC is that when modelling the RHX configuration, the U-shaped flow path is treated as a straight duct instead

of a sharp U-bend configuration. Furthermore, the nonlinear behaviour of the acoustic waves are neglected, only one-dimensional linear approximation is considered. The prediction of the numerical results are improved but overestimated with the experimental results approximately 15% after an additional selection of GUESS and TARGET components. Despite the overestimation of results by the phase 2 of the numerical model, a similar trend as compared to the experimental results can be observed in both ambient and hot conditions for both types of RHXs as shown in Figures 7.7 to 7.10. Phase 1 of the DeltaEC model provides pre-estimation of results for some of the DeltaEC components which are then use as the initial estimation for the phase 2 of the numerical model hence more accurate and faster convergence of results obtained.

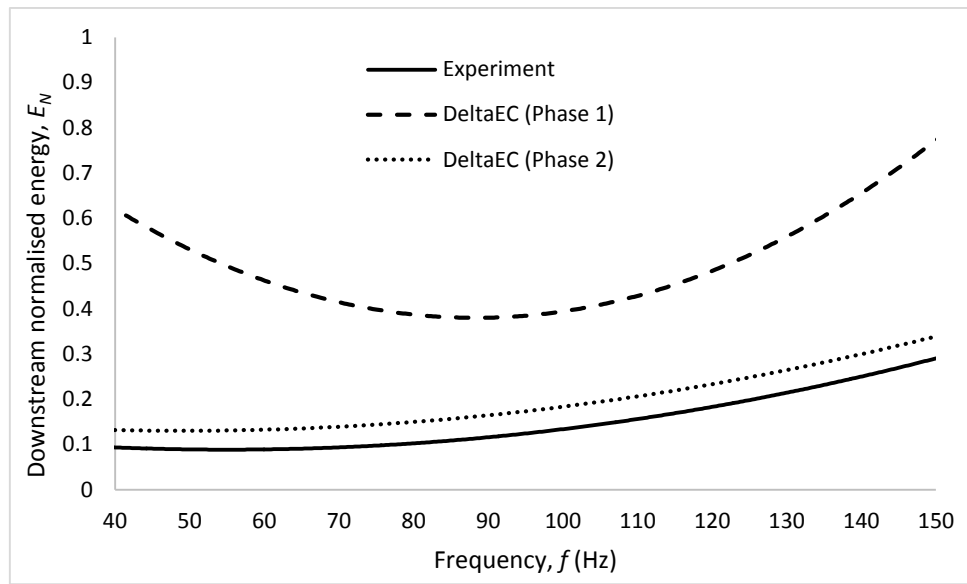


(a)

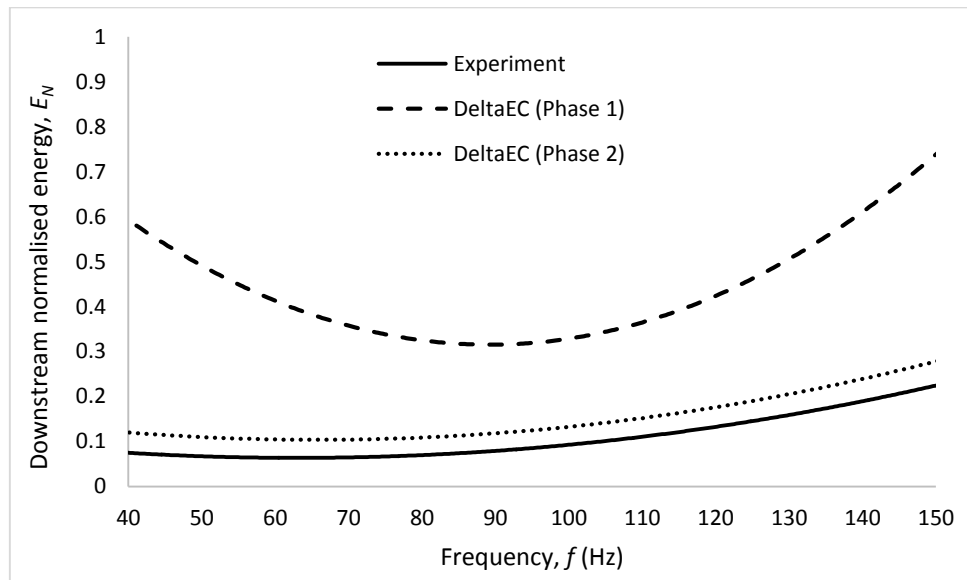


(b)

Figure 7.7: Downstream normalised energy versus frequency in (a) ambient condition and (b) hot condition when the temperature at the RHX is 373K for 30 layers of regenerator in bulge RHX configuration.



(a)



(b)

Figure 7.8: Downstream normalised energy versus frequency in (a) ambient condition and (b) hot condition when the temperature at the RHX is 373K for 30 layers of regenerator in convolution RHX configuration.

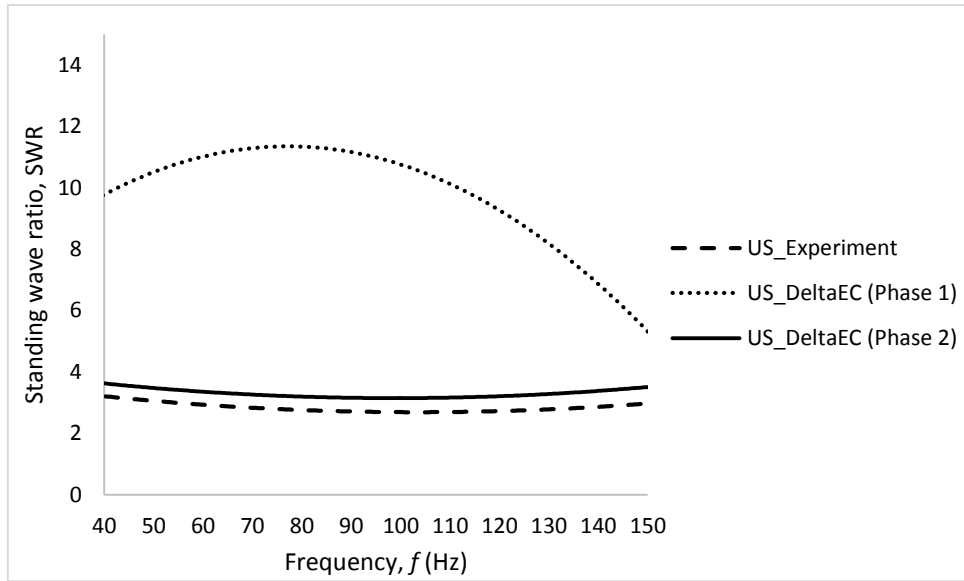


Figure 7.9: SWR versus frequency regenerator meshes at upstream (US) of the system in ambient condition when 30 layers of regenerator for bulge RHX configuration.

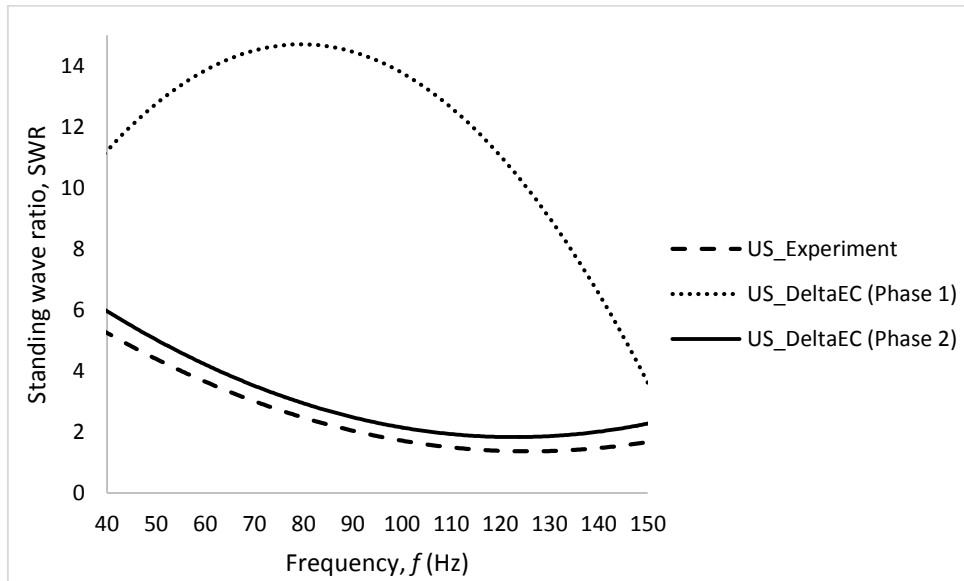


Figure 7.10: SWR versus frequency regenerator meshes at upstream (US) of the system in ambient condition when 30 layers of regenerator for convolution RHX configuration.

7.4 Concluding Remarks

- Numerical models of an impedance tube system was successfully developed in DeltaEC.
- The comparison of the experimental and the numerical results show a very good agreement for a rigid end situation.
- Numerical models of a straight tube and a RHX configurations were successfully created in DeltaEC.
- The phase 2 of the DeltaEC model is found to predict the experimental results more accurately as compared with the phase 1 of the DeltaEC model.
- Adding more GUESS and TARGET components improve the accuracy of numerical results but lead to the complexity of calculations.
- The DeltaEC simulation results here have shown that the selection of the GUESS and TARGET components can be of crucial importance in order to predict the experimental results more precisely.
- Part of this work was published [118].

Chapter 8

Conclusions and Future Work

8.0 Introduction

The research work reported here has addressed the important issues related to the losses in the WHTAE. All the research outcomes have successfully met the overall aim and the objectives of this work which were stated at the beginning of the thesis. The achievements of this work are detailed in the following sections of this chapter. This chapter also highlights some of the limitations encountered during this research work. Some suggestions for the future work are given in the final section.

8.1 Achievements of this Work

A simplified solution is proposed to study the radiation heat transfer between the regenerator and the RHX in two of the SCORE™ engine configurations. Besides that, the feasibility of a new numerical approach has also been examined to study two modes of heat transfer, namely convection and the radiation in the SCORE™ engine using CFD analysis. The radiation heat transfer results obtained by the CFD simulation and the simplified solution have some discrepancies due to detailed shape of the RHX geometry is not taken into consideration in the simplified solution. Both simplified solution and numerical results reveal that bulge is about three times better in total radiation heat

transfer compared to the convection. It is believed that convection need to be reduced or eliminated to improve the performance of the TAE. Based on the numerical results obtained, the design of the bulge shows about five times more in total radiation versus convection to the regenerator top surface. The total amount of heat transferred from the convection is found to be 2.5 times greater than the bulge but 85% is found to be by convection. The CFD simulation carried out here have shown that some operating parameters including the temperature and the pressure as well as the geometry of the RHX can be of crucial importance in the heat transfer process between the hot surface subjected to the flames and the receiving top surface of the regenerator.

An experimental model of a travelling-wave TAE that operates in low frequency is successfully developed by means of passive attenuation using different materials and combinations. The experimental results are compared with the numerical results predicted by DeltaEC. The comparison of the two results shows a very good agreement for a rigid end situation. The selection of the attenuation material or combination of materials should be done carefully and is strongly dependent on the target frequency. A total of eight materials and combinations are investigated to realise that using an elastic end works better for low frequency attenuation applications. According to the experimental results, it is found that the elastic end is up to 250% higher in absorption coefficient compared to the other tested materials and combinations. It is also noticed that no material can work better for all frequencies.

As the regenerator's number of layers increases, the thermal resistance of the regenerator increases. However, when more than 30 layers of mesh are used, there is no significant increase in the regeneration effect. Therefore, it is unbeneficial to add more than 30 layers of mesh. Owing to the perfect contact

between the working fluid and the solid material, the dissipation in the regenerator is dominated by viscous losses. It is also found that the effect of changing the temperature on the RHXs is almost negligible as it only causes a small difference in the acoustic energy dissipation. Furthermore, the convolution RHX configuration is found to have about 30% and 10% higher loss in acoustic energy than the straight tube and the bulge RHX configurations respectively in ambient condition and around 12% and 6% higher in acoustic energy dissipation than the straight tube and the bulge RHX configurations respectively in hot condition. The loss in acoustic energy for the straight tube is mainly due to the viscous losses in the regenerator while the acoustic dissipation for the RHX configuration is mainly caused by the vortices generated at the two 90 ° sharp bends and the sudden change of cross-sectional area. Convolution RHX configuration has higher downstream SWR as compared to the bulge RHX configuration. Because the acoustic field is propagating through many narrow and long channels of the convolution, as a result more reflections and viscous losses are produced as compared to the bulge which has a wider channel for the acoustic field to pass through. DeltaEC is employed to predict the acoustic energy dissipation through the regenerator and the RHX. The numerical model is found to predict the experimental results of the acoustic energy losses accurately for the straight tube configuration but overestimate with the experimental results of about 15 % for the RHXs configuration. The designed DeltaEC models aid the understanding of the physics behind the WHTAE and will be used to determine the design of future prototypes for better performance.

Based on the findings in this work, for future improvement of the design of SCORE™ engine, it is recommended to have a bulge as the RHX to transport most of the heat energy to the top layer of the regenerator in order to enhance the overall efficiency of the engine. Besides that, 30 layers of regenerator can

be a wise decision to have an optimum regeneration effect while producing less attenuation. Numerous sections of this work have been presented at international conferences and meeting as well as published in international journals and conference proceedings.

8.2 Limitations

It is important to mention the limitations encountered during this research work especially when using CFD for investigation. The CFD software uses ideal assumptions and boundary conditions to simplify the model. When using the CFD software for the investigation of the heat transfer between the regenerator and the RHX, the convolution and the bulge are considered as isothermal surfaces, assuming that they have a very small wall thickness and good thermal conductivity which might not be absolutely true but can be taken as a good approximation. Another limitation would be air was assumed to be an ideal gas which is correct only for small variations of the operating conditions.

When conducting the experiment, there are also few common experimental limitations. It is very difficult to measure the temperature at the same point correctly for every experimental run as well as the time constant of the thermocouples used and how they are related to the period of oscillations. Another experimental limitation would be the inherent limited accuracy of the capacitive microphones used for the pressure measurements.

Besides that, the DeltaEC software also has a few limitations. The non-linear effect of the acoustic field is neglected in the numerical simulation, only one-dimensional linear approximation is considered. Another restriction in DeltaEC is that the DeltaEC software uses ideal gas properties and adiabatic acoustic

components in the calculations. The bulge and the convolution RHXs are modelled as compliance volumes. This is due to the fact that only heat exchangers used in common thermoacoustic devices are available in the DeltaEC software. Another limitation would be the DeltaEC software does not take into account the design of U-bend tube in association with the RHX. The U-shaped flow path of the RHX configuration is treated as a straight duct instead of a sharp U-bend configuration.

8.3 Recommendation of Future Work

This research work forms the basis for more future effort in the area of the TAE in particular the WHTAE that operates at low pressure and low frequency. The challenge of the heat transfer from an external source like wood fire to a TAE requires more development based on the outcomes of this work. Further work can also be extended by developing more different design of RHX in order to optimise the overall heat transfer of the engine.

Moreover, the DeltaEC model developed by this work can be used to investigate a wider range of alternative operating conditions for better optimisation. Absorption coefficient can be improved by optimising the elasticity of the elastic termination end. A tuning stub integrated with an elastic end can also be considered in the future which is believed to work as a better alternative at very low frequency.

In additional, further investigations of losses in the regenerator of different materials and porosity could be undertaken for better alternative of regenerator material. Besides that, turbulence characteristic of oscillatory flows in the engine could also be an interesting area to study in the future. For further refinement, particle image velocity (PIV) technique can be considered

to evaluate the unsteady flow pattern in the engine at low frequency and low pressure.

References

1. J. W. S. Rayleigh, R.B.L., *The theory of sound*. Vol. 2. 1945, New York: Dover.
2. O. G. Symko, E.A.-R., Y. S. Kwon, M. Emmi, R. Behunin, *Design and development of high-frequency thermoacoustic engines for thermal management in microelectronics*. *Microelectronics Journal*, 2004. **35**(2): p. 185-191.
3. M. Hatazawa, H.S., T. Ogawa, Y. Seo, *Performance of a thermoacoustic sound wave generator driven with waste heat of automobile gasoline engine*. *Trans of the Japan Society of Mechanical Engineering Part B*, 2004. **70**: p. 292-299.
4. J. A. Adef, T.J.H., *Design and construction of a solar-powdered, thermoacoustically driven, thermoacoustic refrigerator*. *Journal of Acoustical Society of America*, 2000. **107**(6): p. L37.
5. H. Babaei, K.S., W. A. Chishty, *Sustainable thermoacoustic refrigeration system for gas turbine power plants, in 17th symposium of industrial application of gas turbine (IGAT)*. 2007.
6. L. Zoontjens, C.H., A. Zander. *Feasibility study of an automotive thermoacoustic refrigerator*. in *Proceedings of Acoustic 2005*. Busselton, Western Australia.
7. P. H. Riley, C.S., C. J. Johnson, *Designing a low-cost, electricity-generating cooking stove*, in *Tehnology and Society Magazine*. 2010, IEEE. p. 47-53.
8. B. M. Chen, P.H.R., Y. A. Abakr, K. Pullen, D. B. Hann, C. M. Johnson, *Design and development of a low-cost, electricity-generating cooking stove* *Proceedings of the Institution of Mechanical Engineers, Part A: Journal of Power and Energy*, 2013. **227**(7): p. 803-813.
9. S. Garrett, S.B., *The power of sound*, in *American Scientist* 2000. p. 516-525.

10. Sondhauss, C., *Ueber die schallschwingungen der luft in erhitzten glasröhren und in gedeckten pfeifen von ungleicher weite*. Annals of Physics, 1850. **155**(1): p. 1-34.
11. Rijke, P.L., *Notiz über eine neue art, die in einer an beiden enden offenen röhre enthaltene luft in schwingungen zu versetzen*. Annals of Physics, 1859. **183**(6): p. 339-343.
12. T. Yazaki, A.T., Y. Narahara, *Experiments on thermally driven acoustic oscillations of gaseous helium*. Journal of Low Temperature Physics, 1980. **41**(1-2): p. 45-60.
13. Rott, N., *Damped and thermally driven acoustic oscillations in wide and narrow tubes*. Journal of Applied Mathematics and Physics (ZAMP), 1969. **20**(2): p. 230-243.
14. Rott, N., *Thermally driven acoustic oscillations, Part 2: Stability limit for helium*. Journal of Applied Mathematics and Physics (ZAMP), 1973. **24**(1): p. 54-72.
15. Rott, N., *Thermally driven acoustic oscillations, Part 3: Second-order heat flux*. Journal of Applied Mathematics and Physics (ZAMP), 1975. **26**(1): p. 43-49.
16. Rott, N., *Thermally driven acoustic oscillations, Part 4: Tubes with variables cross-section*. Journal of Applied Mathematics and Physics (ZAMP), 1976. **27**(2): p. 197-224.
17. Rott, N., *Thermally driven acoustic oscillations, Part 5: Excitation and power*. Journal of Applied Mathematics and Physics (ZAMP), 1983. **34**(5): p. 609-626.
18. Hofler, T.J., *Thermoacoustic refrigerator design and performance*, in *Physics department*. 1986, University of California: San Diego.
19. W. E. Gifford, R.C.L., *Surface heat pumping*. Advances in Cryogenic Engineering, 1966. **11**: p. 171-179.
20. E. I. Mikulin, A.A.T., M. P. Shkrebyonock, *Low temperature expansion pulse tubes*. Advances in Cryogenic Engineering 1984. **29**: p. 629-637.

21. S. Backhaus, G.W.S., *A thermoacoustic-Stirling heat engine: detailed study*. Journal of Acoustical Society of America, 2000. **107**(6): p. 3148-3166.
22. Feldman, K.T., *Review of the literature on sondhauss thermoacoustic phenomena*. Journal of Sound and Vibration, 1968. **7**(1): p. 71-82.
23. Swift, G.W., *Thermoacoustic engines and refrigerators*. Encyclopedia of Applied Physics 1997. **21**: p. 245-264.
24. J. Wheatley, T.H., G. W. Swift, A. Migliori, *Understanding some simple phenomena in thermoacoustics with applications to acoustical heat engines*. American Journal of Physics, 1985. **53**(2): p. 147-162.
25. Swift, G.W., *Thermoacoustic engines*. Journal of Acoustical Society of America, 1988. **84**(4): p. 1145-1180.
26. J. Wheatley, T.H., G. W. Swift, A. Migliori, *Experiments with an intrinsically irreversible acoustic heat engine*. Physical review letters, 1983. **50**: p. 499-502.
27. M. E. H. Tijani, J.C.H.Z., A. T. A. M. de Waele, *Design of thermoacoustic refrigerators*. Cryogenics, 2002. **42**(1): p. 49-57.
28. S. L. Garrett, J.A.A., T. J. Hofler *Thermoacoustic refrigerator for space applications*. Journal of Thermophysics and Heat Transfer, 1993. **7**(4): p. 595-599.
29. Swift, G.W., *Analysis and performance of a large thermoacoustic engine*. Journal of Acoustical Society of America, 1992. **92**(3): p. 1551-1563.
30. S. C. Ballister, D.J.M., *Shipboard electronics thermoacoustic cooler*, in *Naval Postgraduate School Monterey CA*. 1995.
31. Ceperley, P.H., *A pistonless stirling engine - The travelling wave heat engine*. Journal of Acoustical Society of America, 1979. **66**(5): p. 1508-1513.
32. Swift, G.W., *Thermoacoustics: a unifying perspective for some engines and refrigerators* 2002, Melville, New York: Acoustical Society of America.

33. Z. Yu, A.J.J., S. Backhaus, *A low-cost electricity generator for rural areas using a travelling-wave looped-tube thermoacoustic engine*. Proceedings of the Institution of Mechanical Engineers, Part A: Journal of Power and Energy, 2010. **224**(6): p. 787-795.
34. C. Gardner, C.L., *Design of a standing-wave thermoacoustic engine*, in *The 16th International Congress on Sound and Vibration (ICSV16)*. 2009: Krakow, Poland.
35. Riley, P.H., *Towards a transient simulation of thermo-acoustic engines using an electrical analogy*. Procedia Engineering, 2013. **56**: p. 821-828.
36. B. Chen, A.A.Y., P. H. Riley, D. B. Hann, *Development and assessment of thermoacoustic generators operating by waste heat from cooking stove*. Scientific Research Engineering, 2012 **4**(12): p. 894-902.
37. M. M. Bassem, Y.U., A. Akisawa, *Design and construction of a travelling wave thermoacoustic refrigerator* International Journal of Refrigeration, 2011. **34**(4): p. 1125-1131.
38. M. P. Mitchell, D.G., G. Wood, M. Ibrahim, *Results of tests of etched foil regenerator material*. Cryocoolers, 2007. **14**: p. 381-387.
39. B. Wang, L.Q., D. Sun, K. Wang, W. Yang, J. Zhou, *Visualisation observation of onset and damping behaviors in a travelling-wave thermoacoustic engine by infrared imaging*. International Journal of Heat and Mass Transfer, 2011. **54**(23-24): p. 5070-5076.
40. G. Ding, F.W., G. Zhou, X. Zhang, J. Yu, *An identified study on the active network of a thermoacoustic regenerator*. Scientific Research Engineering, 2009. **1**(1): p. 16-22.
41. B. Chen, Y.A.A., J. H. Goh, P. H. Riley, *Development and assessment of a score demo2.1 thermo-acoustic engine*. Journal of Engineering Science and Technology, 2013. **8**(2): p. 253-263.
42. J. P. Clark, W.C.W., G. W. Swift, *Design environment for low-amplitude thermoacoustic energy conversion (DeltaEC)*. Journal of Acoustical Society of America, 2007. **122**(5): p. 3004-3014.

43. Y. Cho, P.A.N., *Least squares estimation of acoustic reflection coefficient*, in *Institute of Acoustics Spring Conference*. 2002: Salford, UK.
44. Cho, Y., *Least squares estimation of acoustic reflection coefficient*. 2005, University of Southampton.
45. R. Oldfield, F.B. *Accurate low frequency impedance tube measurements*. in *Proceedings of the Institute of Acoustics Autumn Conference (IOA)*. 2008. Oxford, UK.
46. W. C. Ward, G.W.S., *Design environment for low-amplitude thermoacoustic engines*. *Journal of Acoustical Society of America*, 1994. **95**(6): p. 3671-3674.
47. W. C. Ward, J.P.C., G. W. Swift, *Design environment for low amplitude thermoacoustic energy conversion (DeltaEC)*. 2008, Los Alamos National Laboratory: USA.
48. Sanchez, T., *Lessons from project implementation on cook stoves and rural electrification, the practical action experience*. 2008, Energy Technology and Policy Advisor: Rugby, UK.
49. Z. Yu, A.J.J., S. Backhaus. *Design of a low-cost thermoacoustic electricity generator and its experimental verification*. in *Proceedings of the 10th Biennial Conference on Engineering Systems Design and Analysis*. 2010. Istanbul, Turkey: ASME.
50. Z. Yu, P.S., A. J. Jaworski, *A method of characterising performance of audio loudspeakers for linear alternator applications in low-cost thermoacoustic electricity generators*. *Applied Acoustics*, 2011. **72**(5): p. 260-267.
51. C. R. Saha, P.H.R., J. Paul, Z. Yu, A. J. Jaworski, C. M. Johnson, *Halbach array linear alternator for thermo-acoustic engine*. *Sensors and Actuators A: Physical*, 2012. **178**: p. 179-187.
52. S. T. Wee, D.B.H., Y. A. Abakr, P. Riley. *PIV wave propagation investigation of non-linear losses through 90 degree bends in a thermoacoustic engine's feedback loop*. in *Proceedings of the 4th International Meeting of Advances in Thermofluids (IMAT)*. 2011. Melaka, Malaysia: American Institute of Physics.

53. S. T. Wee, D.B.H., Y. A. Abakr, P. Riley, *PIV based wave decomposition technique for waveguide acoustic analysis*, in *International Conference on Low-Cost, Electricity Generating Heat Engines for Rural Areas*. 2012: Nottingham, UK.
54. Y. Ueda, B.M.M., K. Tsuji, A. Akisawa, *Optimisation of the regenerator of a travelling-wave thermoacoustic refrigerator*. *Journal of Applied Physics*, 2010. **107**(3): p. 1-5.
55. Y. B. Tao, Y.W.L., F. Gao, X. Y. Chen, Y. L. He, *Numerical analysis on pressure drop and heat transfer performance of mesh regenerators used in cryocoolers*. *Cryogenics*, 2009. **49**(9): p. 497-503.
56. Z. B. Yu, Q.L., X. Chen, F. Z. Guo, X. J. Xie, *Experimental investigation on a thermoacoustic engine having a looped tube and resonator*. *Cryogenics*, 2005. **45**(8): p. 556-571.
57. S. Backhaus, G.W.S. *Fabrication and use of parallel plate regenerators in thermoacoustic engines*. in *Proceedings of 36th Intersociety Energy Conversion Engineering Conference*. 2001. Savannah, Georgia.
58. S. Backhaus, G.W.S., *A thermoacoustic Stirling heat engine*. *Letters to Nature*, 1999. **399**(6734): p. 335-338.
59. A. S. Abduljalil, Z.Y., A. J. Jaworski, *Selection and experimental evaluation of low-cost porous materials for regenerator applications in thermoacoustic engines*. *Materials and Design*, 2011. **32**(1): p. 217-228.
60. R. Gheith, F.A., S. B. Nasrallah, *Study of the regenerator constituting material influence on a gamma type stirling engine*. *Journal of Mechanical Science and Technology*, 2012. **26**(4): p. 1251-1255.
61. F. Zink, J.V., L. Schaefer, *CFD simulation of a thermoacoustic engine with coiled resonator*. *International Communications in Heat and Mass Transfer*, 2010. **37**(3): p. 226-229.
62. G. Y. Yu, E.C.L., W. Dai, Z. H. Wu, *An energy-focused thermoacoustic stirling heat engine reaching a high pressure ratio above 1.40*. *Cryogenics*, 2007. **47**: p. 132-134.

63. G. Zhou, Q.L., Z. Y. Li, Q. Li, *A miniature thermoacoustic stirling engine*. Energy Conversion and Management, 2008. **49** (6): p. 1785-1792.
64. E. C. Luo, H.L., W. Dai, G. Y. Yu, *Experimental study of the influence of different resonators on thermoacoustic conversion performance of a thermoacoustic-Stirling heat engine*. Ultrasonics, 2006. **44**: p. 1507-1509.
65. K. Tang, G.B.C., T. Jin, R. Bao, X. M. Li, *Performance comparison of thermoacoustic engines with constant-diameter resonant tube and tapered resonant tube*. Cryogenics, 2006. **46**(10): p. 699-704.
66. Y. Liu, P.Y., *Influence of inner diameter and position of phase adjuster on the performance of the thermo-acoustic Stirling engine*. Applied Thermal Engineering, 2014. **73**(1): p. 1141-1150.
67. D. K. W. Yang, Y.A.A., N. M. Ghazali, *Experimental investigations on the effects of coiling and bends on the sound energy losses through a resonator tube*. Procedia Engineering, 2013. **56**: p. 842-848.
68. D. K. W. Yang, Y.A.A., *Experimental determination of acoustic losses in an acoustic resonator using impedance tube technique*. Applied Mechanics and Materials, 2014. **471**: p. 361-366.
69. Y. Zhang, Y.C., W. Dai, E. Luo, *Investigation on the influence of the phase difference between pressure and velocity on the minor losses for a duct with sudden area change*. Cryo and Supercond, 2010. **38**(7): p. 9-19.
70. T. Yazaki, A.I., T. Maekawa, A. Tominaga, *Travelling wave thermoacoustic engine in a looped tube*. Physical review letters, 1998. **81**(15): p. 3128-3231.
71. M. E. H. Tijani, S.S., *A high performance thermoacoustic engine*. Journal of Applied Physics, 2011. **110**(9): p. 093519-093519-6.
72. Blok, C.M.D., *Thermoacoustic system. Dutch patent*. 1998.
73. Blok, K.D. *Low operating temperature integral thermo acoustic devices for solar cooling and waste heat recovery*. in *Proceedings of Acoustic 08*. 2008. Paris, France.

74. Z. Yu, A.J.J., S. Backhaus, *Travelling-wave thermoacoustic electricity generator using an ultra-compliant alternator for utilisation of low-grade thermal energy*. Applied Energy, 2012. **99**: p. 135-145.
75. A. J. Jaworski, X.M., *Development of thermoacoustic devices for power generation and refrigeration*. Proceedings of the Institution of Mechanical Engineers, Part A: Journal of Power and Energy, 2013. **227**(7): p. 762-782.
76. D. L. Gardner, G.W.S., *A cascade thermoacoustic engine*. Journal of Acoustical Society of America, 2003. **114**(4): p. 1905-1919.
77. Blok, K.D. *Novel 4-stage travelling wave thermoacoustic power generator*. in *Proceedings of ASME 2010 3rd Joint US-European Fluids Engineering Summer Meeting collocated with 8th International Conference on Nanochannels, Microchannels, and Minichannels*. 2010. Montreal, Quebec, Canada.
78. Blok, K.D. *Multi-stage travelling wave thermoacoustic in practice*. in *Proceedings of 19th International Congress on Sound and Vibration (ICSV19)*. 2012. Vilnius, Lithuania.
79. N. Kino, T.U., *Evaluation of acoustical and non-acoustical properties of sound absorbing materials made of polyester fibres of various cross-sectional shapes*. Applied Acoustics, 2008. **69**(7): p. 575-582.
80. C. Wang, J.T., *Experimental study of the absorption characteristics of some porous fibrous materials*. Applied Acoustics, 2001. **62**(4): p. 447-459.
81. F. C. Sgard, X.O., N. Atalla, F. Castel, *On the use of perforations to improve the sound absorption of porous materials*. Applied Acoustics, 2005. **66**(6): p. 625-651.
82. W. C. Ward, G.W.S., J. P. Clark, *Interactive analysis, design, and teaching for thermoacoustic using DeltaEC*. Journal of Acoustical Society of America, 2008. **123**(5): p. 3546.
83. M. E. H. Tijani, S.S., *A hot air driven thermoacoustic-Stirling engine*. Applied Thermal Engineering, 2013. **61**(2): p. 866-870.

84. D. Sun, L.Q., B. Wang, Y. Xiao, *Transmission characteristics of acoustic amplifier in thermoacoustic engine*. Energy Conversion and Management, 2008. **49**(5): p. 913-918.
85. A. S. Abduljalil, Z.Y., A. J. Jaworski, L. Shi, *Construction and performance characterisation of the looped-tube travelling-Wave thermoacoustic engine with ceramic regenerator*. World Academy of Science, Engineering and Technology, 2009. **25**: p. 285-288.
86. Z. Yu, A.J.J., *Impact of acoustic impedance and flow resistance on the power output capacity of the regenerators in travelling-wave thermoacoustic engines*. Energy Conversion and Management, 2010. **51**(2): p. 350-359.
87. Fahy, F.J., *A simple method for measuring loudspeaker cabinet impedance* Journal of Audio Engineering Society, 1993. **41**(3): p. 154-156.
88. A. F. Seybert, D.F.R., *Experimental determination of acoustic properties using a two-microphone random-excitation technique*. Journal of Acoustical Society of America, 1977. **61**(5): p. 1362-1370.
89. J. Y. Chung, D.A.B., *Transfer function method for measuring in-duct acoustic properties. I. Theory*. Journal of Acoustical Society of America, 1980. **68**(3): p. 907-913.
90. J. Y. Chung, D.A.B., *Transfer function method of measuring in-duct acoustic properties. II. Experiment*. Journal of Acoustical Society of America, 1980. **68**(3): p. 914-921.
91. J. Y. Chung, D.A.B., *Transfer function method of measuring acoustic intensity in a duct system with flow*. Journal of Acoustical Society of America, 1980. **68**(6): p. 1570-1577.
92. Chu, W.T., *Extension of the two-microphone transfer function method for impedance tube measurements* Journal of Acoustical Society of America, 1986. **80**(1): p. 347-348.
93. Chu, W.T., *Transfer function technique for impedance and absorption measurements in an impedance tube using a single microphone*. Journal of Acoustical Society of America, 1986. **80**(2): p. 555-560.

94. H. Boden, M.A., *Influence of errors on the two-microphone method for measuring acoustic properties in ducts*. Journal of Acoustical Society of America, 1986. **79**(2): p. 541-549.
95. M. Abom, H.B., *Error analysis of two-microphone measurements in ducts with flow*. Journal of Acoustical Society of America, 1988. **83**(6): p. 2429-2438.
96. P. B. Lee, H.P., *Length error analysis for impedance tube measurements*. Journal of Acoustical Society of America, 1989. **85**(4): p. 1769-1772.
97. Katz, B.F.G., *Method to resolve microphone and sample location errors in the two-microphone duct measurement method*. Journal of Acoustical Society of America, 2000. **108**(5): p. 2231-2237.
98. Chu, W.T., *Further experimental studies on the transfer-function technique for impedance tube measurements*. Journal of Acoustical Society of America, 1988. **83**(6): p. 2255-2260.
99. Jones, M.G., *Comparison of methods for determining specific acoustic impedance*. Journal of Acoustical Society of America, 1997. **101**(5): p. 2694-2704.
100. Chu, W.T., *Impedance tube measurements - a comparative study of current practices*. Noise control engineering journal, 1991. **37**(1): p. 37-44.
101. Jones, M.G., *Evaluation of a multi-point method for determining acoustic impedance* Mechanical Systems and Signal Processing, 1989. **3**(1): p. 15-35.
102. S. H. Jang, J.G.I., *On the multiple microphone method for measuring in-duct acoustic properties in the presence of mean flow*. Journal of Acoustical Society of America, 1998. **103**(3): p. 1520-1526.
103. *Fluent 6.3 User's guide*. 2006, Fluent Inc.
104. Cengel, Y.A., *Heat and mass transfer: A practical approach*. 2006: The McGraw-Hill Companies.

105. Howell, J.R., *A catalog of radiation heat transfer configuration factors*, U.o.T.a. Austin, Editor. 2010.
106. B. M. Chen, P.H.R., Y. A. Abakr, *Design and testing of a wood burning electricity generator by using dual-core thermoacoustic engine*, in *2011 World Congress on Engineering and Technology (CET) 2011*: Shanghai, China.
107. M. S. Bharathm, B.S., P. A. Ashwathnarayana, *Performance studies of catalytic converter used in automobile exhaust system*, in *The 37th National and 4th International Conference on Fluid Mechanics and Fluid Power*. 2010: IIT Madras, Chennai, India.
108. A. Neale, D.D., B. Blocken, J. Carmeliet. *Coupled simulation of vapor flow between air and a porous material*. in *Proceedings of the ASHRAE/DOE/BTECC Conference*. 2007. Florida, USA.
109. I. Qashou, H.V.T., B. Pourdeyhimi, *An investigation of the radiative heat transfer through nonwoven fibrous materials*. *Journal of Engineering Fibers and Fabrics*, 2009. **4**(1): p. 9-15.
110. I. Qashou, H.V.T., B. Pourdeyhimi, *An investigation of radiative heat transfer in fibrous thin sheets*, in *Graduate Faculty*. 2009, North Carline State University.
111. Y. Yan, R.U., N. Sobh. *CFD simulation of a research reactor*. in *Proceedings of the Mathematics and Computation, Supercomputing, Reactor Physics and Nuclear and Biological Applications 2005*. Avignon, France: American Nuclear Society.
112. L. Peronski, R.B., D. B. Ingham, L. Ma, M. Pourkashanian, S. Taylor, *Fluid flow analysis and design of a flow distributor in a domestic gas boiler using a commercial CFD software*. *World Academy of Science, Engineering and Technology*, 2008. **2**(4): p. 226-234.
113. Y. P. Banjare, R.K.S., S. K. Sarangi, *CFD simulation of a gifford-mcmahon type pulse tube refrigerator*. *International Journal of Thermal Sciences*, 2009. **48**(12): p. 2280-2287.
114. D. Khoo, Y.A.A., N. M. Ghazali, *Numerical investigation on the heat transfer from the cooking stove to the thermoacoustic engine's*

- regenerator*, in *The International Conference, Low-cost, Electricity generating heat engines for rural areas*. 2012: Nottingham, UK.
115. D. W. Y. Khoo, Y.A.A., N. M. Ghazali, *Radiation heat transfer between the externally heated surface and the regenerator of the thermoacoustic engine*. *Energy Procedia*, 2015. **61**: p. 2576-2579.
116. D. K. W. Yang, Y.A.A., N. M. Ghazali, *CFD investigation of the heat transfer between an external heat source and the regenerator of a thermoacoustic engine*. *Procedia Engineering*, 2013. **56**: p. 835-841.
117. D. W. Y. Khoo, Y.A.A., *Effect of different heat exchangers on the waste-heat driven thermoacoustic engine*. *Journal of Engineering Science and Technology*, 2016. **11**(3).
118. D. W. Y. Khoo, Y.A.A., *Experimental and numerical investigation of the acoustic absorption coefficient at very low frequency*. *Journal of Magnetohydrodynamics*, 2015. **51**: p. 2-6.
119. W. P. Arnott, H.E.B., R. Raspet, *General formulation of thermoacoustics for stacks having arbitrarily shaped pore cross sections*. *Journal of Acoustical Society of America*, 1991. **90**(6): p. 3228-3237.
120. A. F. Seybert, B.S., *Error analysis of spectral estimates with application to measurement of acoustic parameters using random fields in ducts*. *Journal of Acoustical Society of America*, 1981. **69**(4): p. 1190-1199.
121. L. E. Kinsler, A.R.F., A. B. Coppens, J. V. Sanders, *Fundamentals of acoustics*. 4th ed. 1999: John Wiley and Sons Inc.
122. T. Biwa, Y.T., U. Mizutani, M. Kozuka, T. Yazaki, *Experimental demonstration of thermoacoustic energy conversion in a resonator*. *Physical Review E*, 2004. **69**(6): p. 066304.
123. S. Garrett, S.B., *DELTAEC is also an acoustics teaching tool*. *Journal of Acoustical Society of America*, 2008. **123**(5): p. 3654.